Optical Properties of Cirrus Clouds from Satellite Imagery and Radiative Transfer Calculations

by
Robert S. Stone and Graeme L. Stephens

Department of Atmospheric Science
Colorado State University
Fort Collins, Colorado

Colorado State University

Department of Atmospheric Science

Paper No. 425

OPTICAL PROPERTIES OF CIRRUS CLOUDS FROM SATELLITE IMAGERY AND RADIATIVE TRANSFER CALCULATIONS

by

Robert S. Stone and Graeme L. Stephens

Research supported by NSF Grant ATM-8519160

Principal Investigator: Graeme L. Stephens

Department of Atmospheric Science
Colorado State University
Ft. Collins, CO 80523

December 1987

Atmospheric Science Paper No. 425

ABSTRACT

In this study, differences between narrowband near infrared (NIR) and infrared (IR) brightness temperatures are related to cloud optical depth providing a theoretical basis for determining cirrus optical properties from combined satellite images. A simple monochromatic radiative transfer model is developed and utilized to simulate the upwelling radiation field as a function of cloud optical depth for five hypothetical clouds characterized by different particle size distributions, volume densities and temperatures. For simplicity, irregular shaped ice crystals are approximated by equivalent spheres. The radiative properties for each model cloud are calculated at the appropriate wavelengths employing a Mie algorithm and the results compiled into tables.

Two case studies are presented to demonstrate the potential of the spectral differencing method. The first involves correlation of bispectral satellite imagery (from the NOAA-9 AVHRR) and ground-based lidar and radiometric (LIRAD) measurements. Validation of the method is accomplished by collating lidar returns with aerological data in order to deduce the physical characteristics of the cirrus layer. In the second case, only bispectral data from the GOES-6 VAS radiometer and rawinsonde data are used. In each case, comparative analysis of satellite derived and simulated cloud brightness temperature differences (NIR-IR) as a function of cloud optical depth are used to select the model cloud which best represents the observed cloud. The radiative properties of the cloud are then assumed to be those listed in the tables for the selected model. Results from the latter study are used to produce a contour map of cirrus cloud optical depth to further illustrate the value of using the spectral differencing method for studying cirrus.

This study represents a first step in the development of an objective technique for determining cirrus cloud optical properties. In light of the encouraging results presented in this paper, recommendations are made to further validate and refine this technique through intercomparisons of *in situ* and remotely sensed measurements and the use of more radiative transfer models.

ACKNOWLEDGEMENTS

We wish to acknowledge various people who have contributed in different ways to this research. In the early stages, Alan Lipton and Duane Whitcomb helped one of us (R.S.S.) with the operation of the CSU ground station and assisted in the collection and processing of the GOES imagery used in this study. Nan McClurg assisted with the CSU interactive research imaging system (IRIS). Dr. Garrett Campbell provided software support as did Chi Fan Shih, Dr. Steven Ackerman, Kelly Dean and Bill Davis. Bill Davis also helped to produce photographs from the digital GOES images which are included in this paper.

We are particularly grateful to Dr. Martin Platt for supplying data and results from his Aspendale Cirrus Experiments conducted in Australia. Access to Dr. Warren Wiscombe's Mie algorithm on the NCAR CRAY X-MP was of great value in formulating the theoretical basis for this study. We also wish to thank Dr. Don Hillger and Dr. Stan Kidder for their fruitful suggestions which paved the way to meaningful comparisons between satellite and ground-based radiance measurements. We also appreciate the efforts of Susan Lini who helped prepare the manuscript.

This research was supported by NSF grant ATM-8519160. The support of Dr. Tom Vonder Haar is also gratefully acknowledged under grant NA-85RAH05045.

CONTENTS

LIST OF FIGURES

LIST OF TABLES

Chapter 1

INTRODUCTION

Cirrus clouds are known to be important modulators of the earth's radiation budget. Existing cloud climatologies indicate that, on the average, cirrus cover approximately 20% of the globe, making them the most extensive of all cloud types. Though optically thin, they significantly affect the amount of solar radiation transmitted to the surface and the infrared radiation emitted from the upper boundary of the atmosphere. Whether the presence of cirrus clouds causes the earth-atmosphere system to heat or cool is dependent on the microphysical and radiative properties of the clouds, their optical depth and their altitude. All of these characteristics have been observed to vary greatly, complicating our understanding of the quantitative effects of these heating/cooling processes (often referred to as the greenhouse and albedo effects respectively). In addition, the presence of high thin cirrus leads to ambiguous interpretation of satellite imagery used to infer the physical state of the atmosphere. Due to the sensitivity of radiative transfer to perturbations in cirrus characteristics, parameterizing these clouds in numerical weather and climate models is particularly difficult. Model simulations of such perturbations will remain rudimentary until better parameterization schemes are developed.

1.1 Radiative Effects of Cirrus Clouds

Examples are given in this section that illustrate the problem of cirrus/radiative feedbacks introduced above. A classic paper by Manabe and Wetherald (1967) describing the results of their one-dimensional radiative convective equilibrium model (with given distribution of relative humidity) called attention to the fact that thermal equilibrium in the atmosphere is very sensitive to changes in the concentration of its gaseous constituents and/or cloud type and amount. Figure 1.1 shows how various cloud types may affect the

surface equilibrium temperature. It is apparent that cirrus clouds have the distinction of increasing surface temperature with increasing cloudiness, while the opposite effect occurs for thick, low clouds.

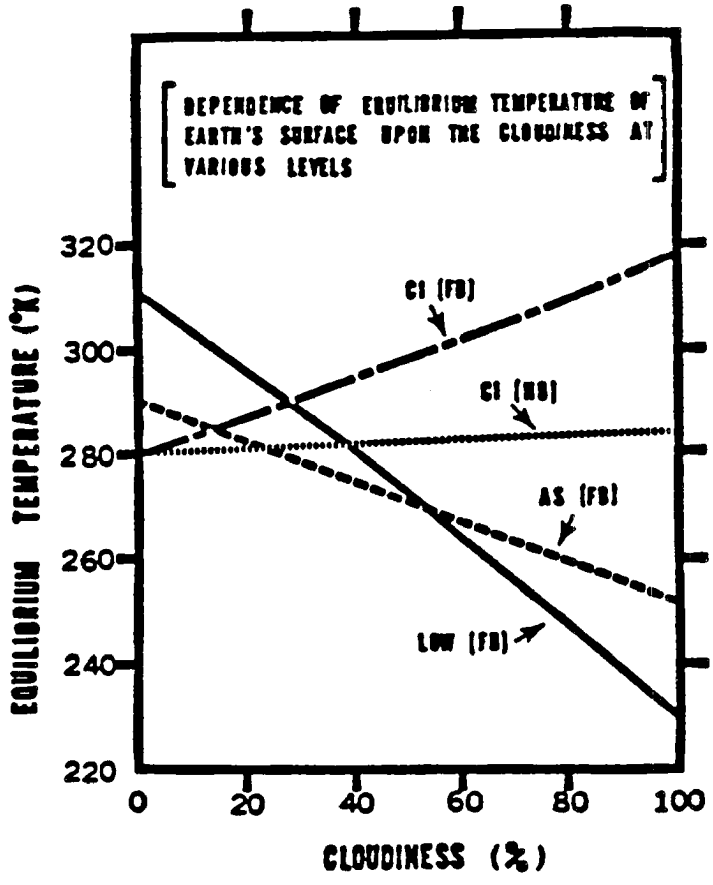

Figure 1.1: Radiative convective equilibrium temperature at the earth's surface as a function of cloudiness for cirrus, altostratus, and low clouds. FB and HB refer to full black and half black, respectively (from Manabe and Wetherald, 1967).

Stephens and Webster (1981), employing a one-dimensional radiative convective model studied the sensitivity of surface temperature to the presence of clouds varying in thickness and height. They also found that high thin clouds generally cause an increase in the equilibrium surface temperature while thicker, lower clouds cause surface cooling. The greenhouse vs. albedo effects of different cloud types were again demonstrated by Liou and Gebhart (1982). Figures 1.2 (a) and (b) show the effects of thin vs. thick, and high vs. low clouds on the equilibrium temperature profile of the atmosphere.

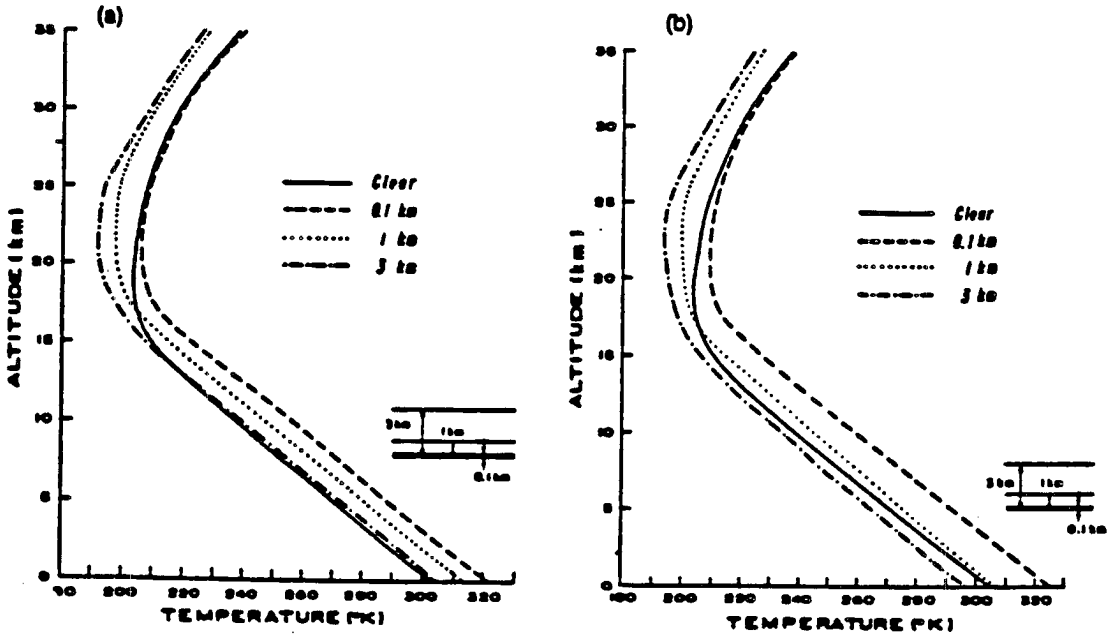

Figure 1.2: Effects of the cirrus cloud thickness and height on the thermal equilibrium temperature in a one-dimensional climate model (after Liou and Gebhart,1982).

Figure 1.2 (a) illustrates how optically thin cirrus produce warming below the cloud layer due to a combination of large solar flux transmission and a thermal infrared greenhouse effect, while Figure 1.2 (b) indicates that low, thick ice clouds, or water clouds produce IR-cooling throughout the troposphere due to a decrease in solar flux entering the atmosphere (the albedo effect).

The effects of high level clouds on the radiative energy balance in the atmosphere are highly dependent on the characteristics of those clouds. Stephens and Webster (1979) made radiative transfer calculations of infrared fluxes for the $11\mu m$ window region of the spectrum and found that "net radiative fluxes at the boundary of the atmosphere varied substantially for different assumed radiative properties of cirrus clouds..." In short, there is convincing theoretical evidence that the atmospheric temperature profile and heating/cooling rates are sensitive not only to the cloud's thickness and height, but also to the radiative properties of cirrus.

1.2 Distinguishing Characteristics of Cirrus Clouds

Several characteristics of cirrus clouds distinguish them from other cloud types. These are introduced below and will be discussed in greater detail in the context of topics presented in subsequent chapters. Figures illustrating the features most pertinent to this study follow. (See Liou, 1985 and references therein for a complete summary of cirrus characteristics).

- They occur only at high altitudes (above $\approx$ 4 km).
- They are "non-black". Typical absorption emissivities (ϵ_a) range from 0 to 0.7, rarely exceeding 0.95 (Figure 1.3).
- They are optically thin. Cirrus cloud optical depth (τ) seldom exceeds a value of 5; typically, $\tau < 3$.
- They are composed primarily of many small non-spherical ice crystals in the shape of columns, bullets and rosettes (Figure 1.4); however, a significant number of large crystals with mean crystal lengths ranging between 60 and 1000 μm have been observed. (see Figure 1.5 for size distribution). Many of these larger crystals are hexagonal plates and elongated columns which may assume preferential orientation in the horizontal plane under the influence of fluid dynamical forces.
- Their ice water content (IWC) varies over several orders of magnitude and is temperature dependent. Typical values are less than 0.02 g m^{-3} (Figure 1.6).
- Their cloud base temperature is generally below -20°C, and thier cloud top temperatures may range to below -55°C.
- They are often dynamically associated with upper level troughs, high pressure systems or jet streams and are most prevalent over the tropics and mid-latitudes (Figure 1.7).

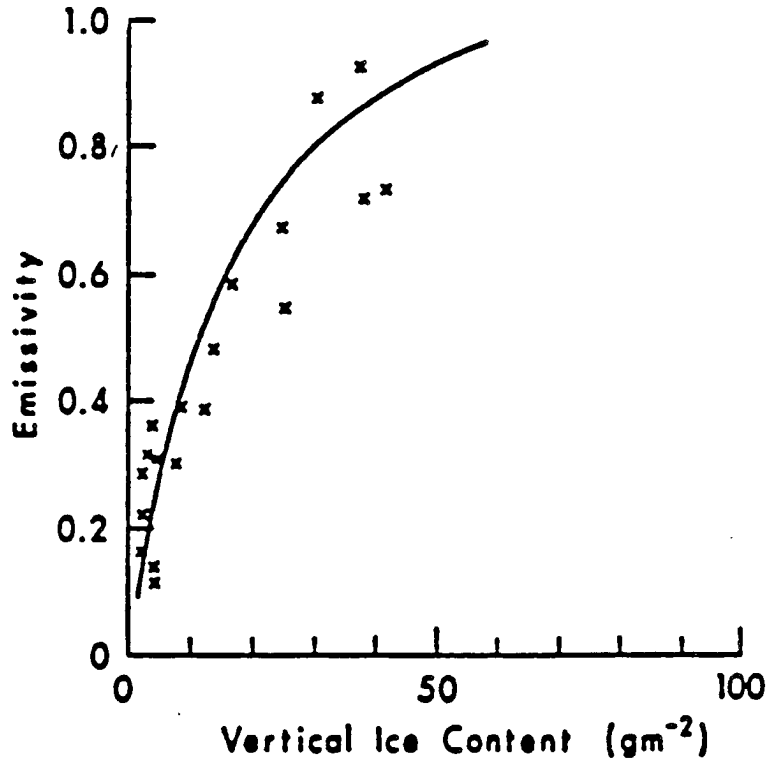

Figure 1.3: Cirrus IR emissivity as a function of vertical ice content from aircraft meaurements (adapted from Paltridge and Platt, 1981).

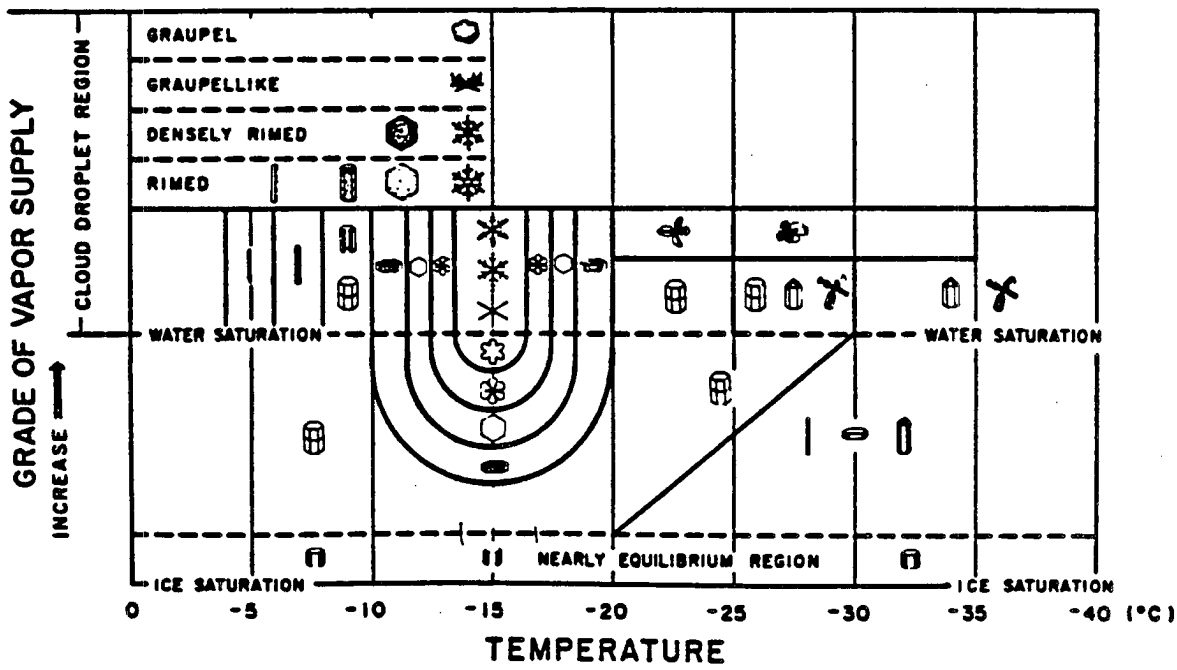

Figure 1.4: Temperature and humidity conditions for the growth of natural snow crystals of various types (from Magono and Lee, 1966; by courtesy of J. Fac. Sci., Hokkaido University).

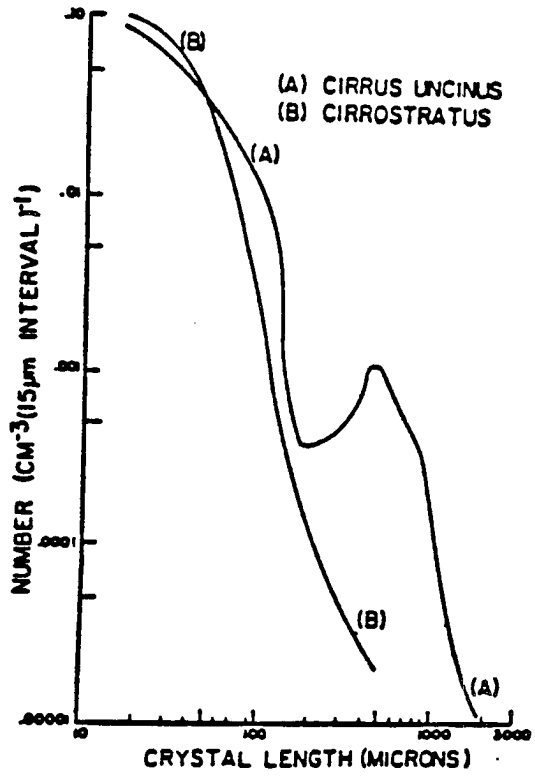

Figure 1.5: Ice crystal size distributions for cirrus clouds (after Heymsfield, 1975a).

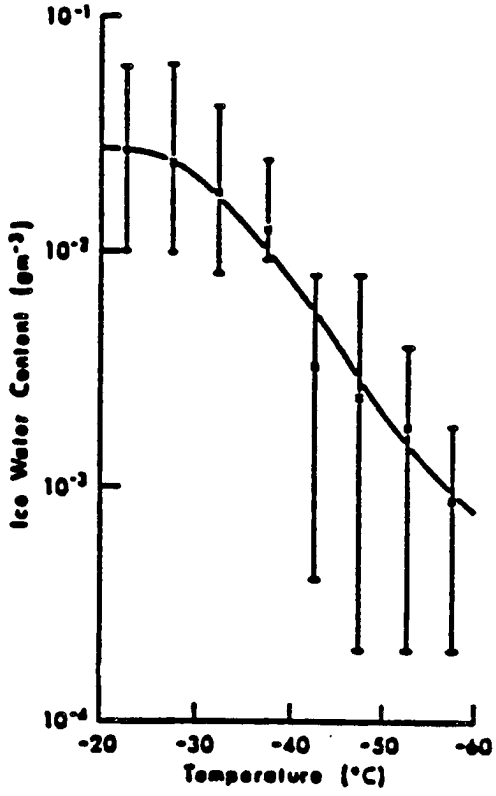

Figure 1.6: Ice water content as a function of temperature. Data from Heymsfield and Platt (1984).

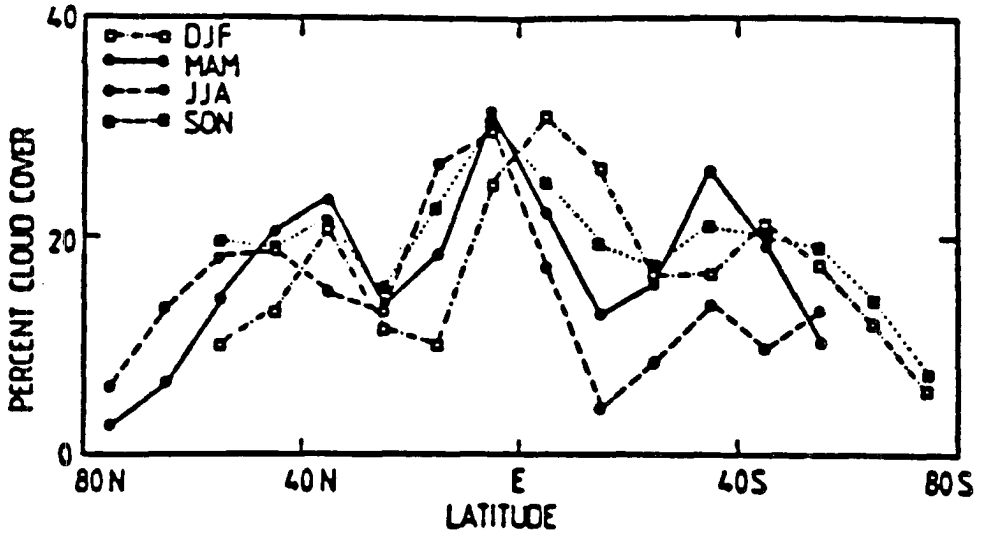

Figure 1.7: Seasonal zonal average distribution of the occurance of high clouds (after Barton, 1983).

1.3 Cloud Optical Properties

Central to this study is the determination of cloud optical properties. However, as is common in the literature, these "optical" properties will often be referred to as radiative properties or radiative parameters. These terms will be used interchangably throughout this work and thus, they should not be misconstrued as having different meanings. This study focuses on three parameters that characterize the radiative processes which control the transfer of radiation through an absorbing-emitting and scattering medium. These parameters are introduced by simple definition below and will be discussed at length in the main body of this paper. They are:

- the total extinction coefficient (k_{ext}), which gives a measure of the total attenuation a beam of radiation experiences due to absorption and scattering within the medium,
- the single scattering albedo ($\tilde{\omega}_o$), which is the fractional amount of total extinction due to pure scatter of a beam of radiation, and

- the asymmetry factor (g), which may be viewed as a measure of the degree of forward scatter of a beam of radiation.

1.4 International Research Plan

Because of the current inadequacies of numerical models to properly incorporate the effects of large scale cloud systems, a concerted international effort is underway to gain knowledge about the distribution and radiative characteristics of these systems. Due to their wide distribution and strong influence on the earth's radiation budget, cirrus and marine stratus/stratocumulus are the primary focus of intensive investigations (FIRE (First ISCCP Regional Experiment) Research Plan, 1983). The main sources of data for monitoring the earth's cloud climatology and for studying cloud/radiative-dynamical feedback mechanisms are visible and infrared images of the earth which are routinely collected and transmitted by a system of operational geostationary and polar orbiting satellites. The International Satellite Cloud Climatology Project (ISCCP, 1983 - present) is responsible for coordinating this effort. In addition, regional experiments such as FIRE are being conducted to compliment ISCCP. These regional experiments are designed to improve our knowledge of the radiative and microphysical characteristics of clouds on a smaller scale. Better use of satellite imagery for improving parameterization schemes used in various numerical models is one of the goals of these efforts. Any method developed to facilitate the determination of cirrus radiative properties will aid in the attainment of these goals. To this end, I have directed my research.

1.5 Research Objectives and Structure of this Thesis

The objectives of this study were three-fold:

- **First**, a general survey of the distinguishing microphysical and radiative properties of cirrus clouds was made in order to understand why these clouds perplex general climate modelers in their effort to incorporate cloud/radiative feedbacks involving cirrus into their models. These characteristics were already introduced above and are discussed in more detail in Chapter 3 in the context of the scattering and absorptive properties of ice particles.

- Second, a simple monochromatic radiative transfer model was developed to simulate the transfer of radiation through model cirrus clouds representing a range of observed microphysical properties. Through these simulations, a theoretical relationship between differences in radiance values for two "window" wavelengths and cloud optical depth was explored as a potential means to detect optically thin cirrus clouds utilizing bispectral satellite imagery. This is referred to as the spectral differencing method (after Stephens, 1981). The relevant theory and model development and initialization requirements are described in Chapter 2.

  A slight digression is made in Chapter 4 to introduce radiometry and discuss the steps necessary to collect, process and interpret satellite imagery. Special note is made regarding the geometric constraints placed on analyses involving correlation of ground-based and satellite measurements. Then, in Chapter 5, theoretical model results are discussed in relation to specific simulations required for comparison with multispectral satellite imagery (MSI).

- The third is perhaps the most novel feature of this study. A technique was developed (based on the spectral differencing method) to deduce the microphysical and radiative properties of observed cirrus clouds and to "map" the cloud's optical depth. Though the theoretical basis for this work had already been formulated by Stephens (1981), and Arking and Childs (1985), the methodology developed in Chapter 6 represents an alternative method for deriving cirrus optical properties. The theory is validated and applications of the use of this technique are presented. Two case studies are analyzed to demonstrate the method's potential. The first is unusual in that both ground-based and satellite radiance measurements are correlated with lidar and rawinsonde data. The second utilizes readily available data such as those being archived by ISCCP/FIRE. The latter application demonstrates a straightforward means to estimate the radiative parameters required to initialize monochromatic radiative transfer calculations. Results of these analyses are encouraging and future development of this method is recommended as a first step toward determining broadband radiative properties required for use in general climate models.

1.6 Final Remarks

There is an obvious need for better determination of cirrus radiative properties. Explicit intercomparisons of in situ aircraft measurements of cirrus microphysics, airborne, ground-based and satellite radiometric observations and vertical sounding data, etc. will be necessary to validate theoretical methods for determining these properties. The technique introduced in Chapter 6 of this paper suggests one approach to estimating the radiative properties of cirrus; however, further validation and refinement of this technique will be required. The in-situ observations made during the 1986 FIRE experiment will provide an excellent microphysical data base for the further study of cirrus. There is reason to believe that a valid objective technique will soon be developed to unambiguously map cloud optical depths and provide reliable estimates of radiative parameters utilizing MSI data. The result would be significantly improved parameterization schemes for use in climate models and a clearer understanding of the feedbacks between radiative and dynamical processes.

Chapter 2

THE RADIATIVE TRANSFER EQUATION AND MODEL

A thorough discussion of radiative transfer theory and cloud radiative properties is beyond the scope of this thesis. Only a summary of relevant topics is presented. This chapter describes the radiative transfer equation and the model used to solve this equation. The dependency of cloud optical properties on microphysics and wavelength is discussed in Chapter 3. It is assumed the reader has a fundamental knowledge of these subjects and is familiar with the notation used.

Multi-channel satellite radiometers measure radiances over narrow but finitely wide spectral regions or channels. These channels are selected to span the solar and terrestrial emission spectra. Subsequent sections provide an outline of a model that is capable of simulating these radiances for a hypothetical and necessarily simple atmosphere containing cirrus cloud.

The ice crystals that comprise a cirrus cloud absorb and scatter direct shortwave (sw) radiation from the sun. In addition to these processes, these crystals also absorb and emit radiation in the longwave (lw) region of the spectrum. The emittance according to Kirchoff's law equals the absorptance for a given wavelength and temperature; $a_\lambda = \epsilon_\lambda$. All these processes depend on details of the microphysical characteristics of the crystals.

Of particular interest in this study is a region where the solar and terrestrial spectra "overlap". Molecular absorption by atmospheric gases is very weak in this region; thus a quasi-transparent "window" exists which allows greater transmission through the atmosphere at these wavelengths. Cloud particles on the other hand may absorb, emit, and scatter a significant amount of radiation at these near infrared (NIR) window wavelengths. Clouds are exposed to both direct (solar) radiation from above and diffuse radiation from

below in this spectral interval giving rise to external sources in the radiation field as will be explained in the next section. It was proposed by Stephens (1981) that differences in radiance values between NIR-wavebands and those in the lw-window region at $8 - 13\mu m$ might be useful for estimating cloud optical depth. Selection of wavebands for this study were made on the basis of this proposition. Their spectral centers are highlighted in Figure 2.1.

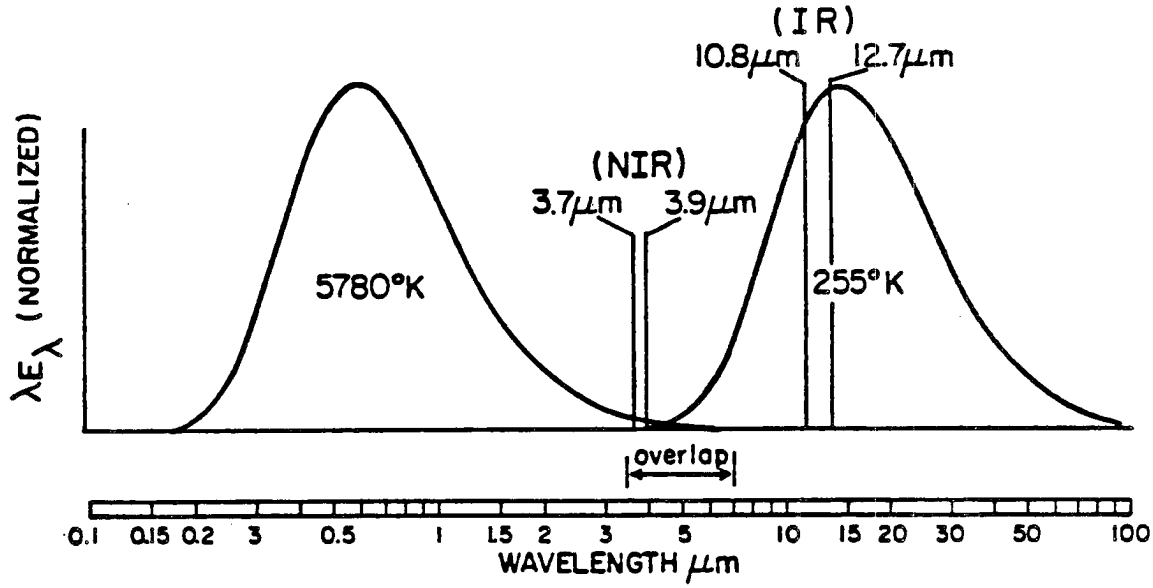

Figure 2.1: Schematic representation of the spectral centers used in this study to compare calculated and observed radiances [Adapted from R.M. Goody, "Atmospheric Radiation," *Oxford Univ. Press* (1964), p.41].

2.1 The Radiative Transfer Equation

The required monochromatic radiances are simulated by solving the general form of the radiative transfer equation for an absorbing-emitting and scattering atmosphere. Each hypothetical cirrus layer is assumed to be plane-parallel and horizontally homogeneous; that is, the microphysical characteristics and radiative properties do not vary horizontally within the cloud layer. Only "thin" clouds are considered and they are assumed to be isothermal with a temperature equal to the environmental temperature. The general form of the radiative transfer equation appropriate to this study is

$$\mu \frac{dI_\lambda(\tau;\mu,\phi)}{d\tau} = -I_\lambda(\tau;\mu,\phi) + \frac{\tilde{\omega}_o}{4\pi}\int_o^{2\pi}\int_{-1}^{+1} P(\mu,\phi;\mu',\phi')\, I_\lambda(\tau;\mu',\phi')\, d\mu' d\phi'$$

$$[A]$$

$$+ \ \tilde{\omega}_o \frac{F_{o\lambda}}{4\pi} P(\mu,\phi;\mu_o,\phi_o)\, e^{-\tau/\mu_o} \qquad + \ (1-\tilde{\omega}_o)\, B_\lambda(T)$$

$$[B] \qquad\qquad [C] \qquad\qquad (2.1)$$

where:

- $I_\lambda(\tau;\mu,\phi)$ is the diffuse monochromatic intensity for an angle defined by μ,ϕ at an optical depth, τ,
- $(\mu,\phi;\mu',\phi')$ represents the scattering angle between the incident angle (μ',ϕ') and response angle (μ,ϕ),
- $(\mu,\phi;\mu_o,\phi_o)$ represents the scattering angle between the solar angle (μ_o,ϕ_o) and response angle (μ,ϕ),
- $\mu' = \cos\theta'$, where θ' is the incident zenith angle,
- $\mu = \cos\theta$, where θ is the response zenith angle,
- $\mu_o = \cos\theta_o$, where θ_o is the solar zenith angle,
- ϕ', ϕ and ϕ_o are the respective azimuth angles,
- $P(\mu,\phi;\mu',\phi')$ and $P(\mu,\phi;\mu_o,\phi_o)$ define the phase functions for the diffuse and direct solar beams respectively,
- $k_{ext} = k_{sca} + k_{abs}$ is the total volume extinction coefficient,
- $\tilde{\omega}_o = k_{sca}/k_{ext}$ is the single scattering albedo,
- $F_{o\lambda}$ is the incident solar flux over the band-width with spectral center given by the wavelength λ,

- τ is the optical depth defined by $(k_{ext} * dz)$ where dz is the geometric thickness of the cloud; τ and z are measured from the top of the layer,
- $(1 - \tilde{\omega}_o)$ is a measure of emissivity (absorptivity), and
- $B_\lambda(T)$ is the Planckian black-body emission for the layer, where T is the layer temperature.

The integration is performed over all solid angles given by

$$\int_{4\pi} d\Omega = \int_0^{2\pi} \int_{-1}^{+1} d\mu' d\phi' = \int_0^{2\pi} \int_{-1}^{+1} \sin\theta' d\theta' d\phi' \tag{2.2}$$

Equation (2.1) states that the change in monochromatic intensity with optical depth as a function of angle results from a decrease in the incident intensity due to extinction along the path plus an increase due to sources as described below.

Source term:

- [A] represents the "virtual" source of diffusely scattered radiation from all angles (μ', ϕ') into the direction (μ, ϕ). The phase function gives the probability that energy incident from (μ', ϕ') will be re-directed into (μ, ϕ) as a consequence of a single scattering event. The single scattering albedo $(\tilde{\omega}_o)$ ranges from 1 for conservative scatter (no absorption) to 0 for pure absorption (no scatter).
- [B] is a "pseudo" source due to the diffuse-direct splitting of the collimated incident beam. This beam undergoes attenuation $\left(e^{-\tau/\mu_o}\right)$ as it is transmitted through an atmosphere of optical depth τ and is scattered at this level according to the phase function formed by the solar angle (μ_o, ϕ_o) and (μ, ϕ). The entire process depends on the fraction of scatter given by $\tilde{\omega}_o$.
- [C] represents the thermal emission from the cloud particles themselves; the Planckian black-body emission modified by the fractional absorptance (or emittance) $(1 - \tilde{\omega}_o)$.

It should be noted that source term [B] depends on $F_{o\lambda}$. For longwave calculations, or for nighttime NIR-calculations when $F_{o\lambda} = 0$, there is no contribution from this term. However, for NIR-calculations during the day, [B] may add significantly to the total upwelling radiance reflected by the cloud. The effect of this contribution will be discussed further in Chapter 5.

Equation (2.1) applies to an infinitesimally thin layer in which only single scattering occurs. A realistic transfer problem involves calculating the radiation field at the boundaries of a finite or semi-infinite multiply scattering medium. The model used in this study was adapted from that of Stephens (1980). It utilizes quadrature to reduce the integro-differential equation (2.1) to an equivalent matrix form which can be numerically solved to simulate the radiation field for a thin single scattering layer. Then, by employing the method of "doubling and adding" the radiation field for a multiply scattering vertically inhomogeneous atmosphere of arbitrary thickness can be determined. Only an outline of this procedure is given here. A more thorough development of this approach is described in the literature; Grant and Hunt (1969), Wiscombe (1975), Liou (1980), Stamnes (1986), Stephens (1980, 1985 and 1987-pending publication), etc.

2.2 Introduction to Quadrature

Exact solutions to the integro-differential transfer equation (2.1) are generally difficult and sometimes impossible to obtain. Therefore, numerical methods have been developed which yield reasonably accurate solutions for a variety of atmospheric radiative transfer problems. These methods discretize the radiation field and employ quadrature formulae to represent the integrals in (2.1). For instance, Guassian quadrature may be used to represent an integral of a polynomial of degree $N \leq 2n - 1$ exactly by the following quadrature formula:

$$\int_{-1}^{+1} f(\mu)\, d\mu = \sum_{j=1}^{n} f(+\mu_j)\, w_j + \sum_{j=1}^{n} f(-\mu_j)\, w_j \tag{2.3}$$

where $\pm\mu_j$ and w_j are the quadrature abscissae and weights respectively. Other quadrature formulae are given by Chandrasekhar (1960).

The transfer problem can be defined as follows. The radiance field at a point along a vertical lattice is divided into upward (+) and downward (−) hemispheres, each defined by n-discrete angles (quadrature abscissae) denoted by $+\mu_j$ and $-\mu_j$ respectively, $j = 1, ..., n$ where $-\mu_j = -(+\mu_j)$. Together they comprise a $2n$-stream model of the radiation field. It is convenient to view the flow of radiation in terms of incident (i) or response (r) directions depending on whether the radiation flows toward or away from a particular point. The upward response intensities $I_r^+(+\mu_j)$ and the downward response intensities $I_r^-(-\mu_j)$ represent the solution to the transfer equation. Figure 2.2 shows the configuration of the incident and response fields for the case of 4 quadrature angles (i.e., 8-streams). For this study 16 quadrature angles in each hemisphere were used (32-streams). These angles and their corresponding weights are listed in Table 2.1.

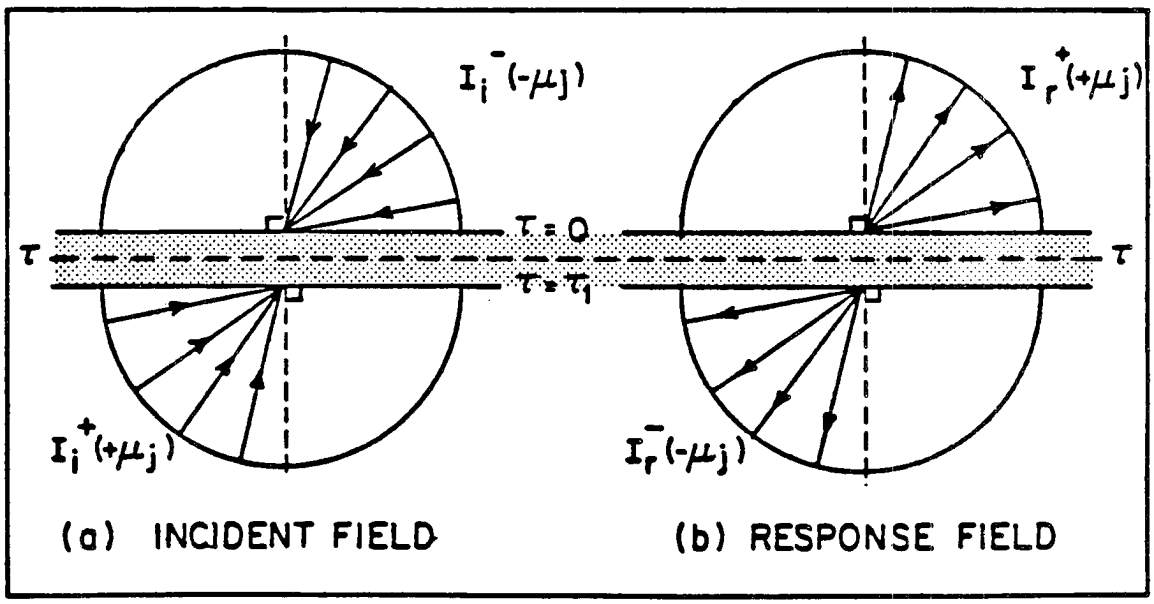

Figure 2.2: (a) represents the incident field and (b) the response field for a set of 4 discrete quadrature angles relative to the upward and downward hemispheres defined in the text (Adapted from AT-721 class notes, Stephens, 1986).

Table 2.1

Table 2.1: Quadrature Angles and Weights used in a 32-Stream Radiative Transfer Model.

QUADRATURE POINT	ANGLE (θ_j)	$\mu_j = cos\theta_j$	WEIGHT (w_j)
1	87.231	0.0483077	0.0965401
2	81.693	0.1444720	0.0956387
3	76.155	0.2392874	0.0938444
4	70.618	0.3318686	0.0911739
5	65.080	0.4213513	0.0876521
6	59.542	0.5068999	0.0833119
7	54.005	0.5877158	0.0781939
8	48.467	0.6630443	0.0723458
9	42.930	0.7321821	0.0658222
10	37.393	0.7944838	0.0586841
11	31.857	0.8493676	0.0509981
12	26.321	0.8963212	0.0428359
13	20.787	0.9349061	0.0342739
14	15.255	0.9647623	0.0253921
15	9.731	0.9856115	0.0162744
16	4.239	0.9972639	0.0070186

2.3 Phase Function Approximation

The scattering phase function for a distribution of particles is generally a complicated function of the scattering angle Θ. The scattering angle can be defined in terms of the angle pair $(\theta, \phi; \theta', \phi')$ by

$$\cos\Theta = \cos\theta' \cos\theta + \sin\theta' \sin\theta \cos(\phi' - \phi) \tag{2.4}$$

where (θ', ϕ') and (θ, ϕ) define the incident and response angles respectively. Figure 2.3 schematically illustrates the relationship between the incident and scattered direction and the scattering angle formed between these directions.

The phase function in (2.1) describing the angular distribution of scattered radiation can now be written in terms of the scattering angle defined above. It is necessary to introduce quadrature in such a way to insure the normalization of the phase function to conserve energy. This normalization has the following form,

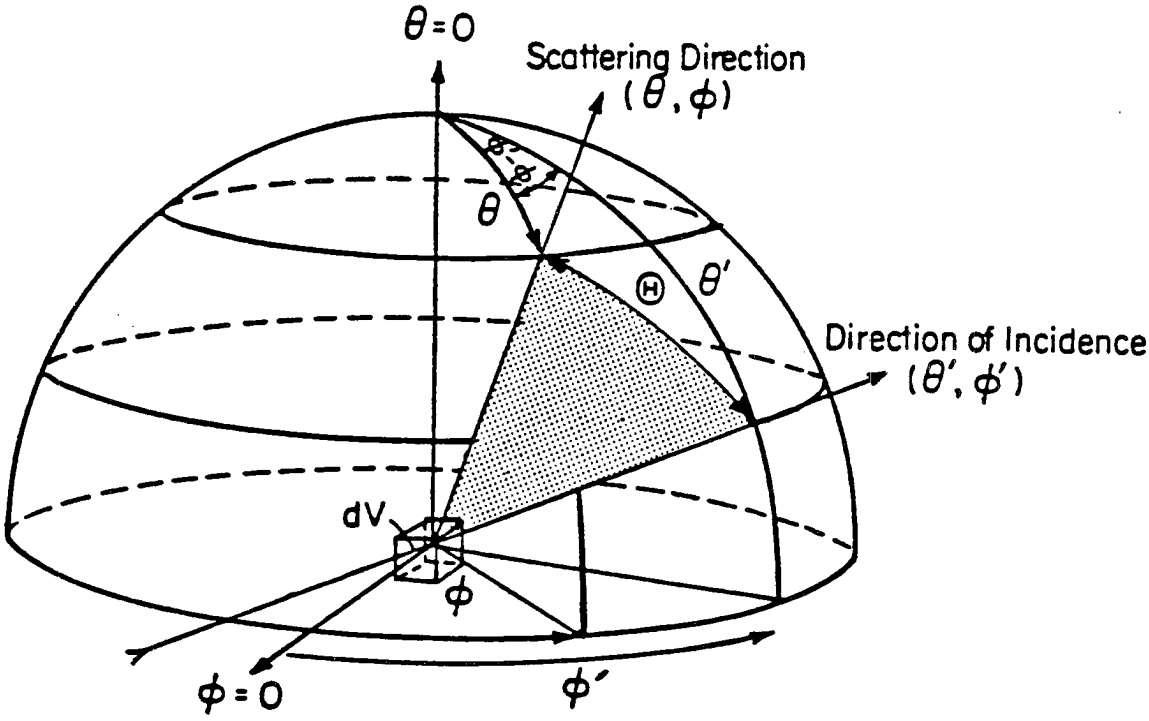

Figure 2.3: Scattering geometry defining the scattering angle Θ (Adapted from Paltridge and Platt, 1976).

$$\int_0^{2\pi}\int_0^{\pi} \frac{P(\cos\Theta)}{4\pi} \sin\Theta d\Theta d\phi = 1 \tag{2.5}$$

Numerically it is more convenient to represent the phase function by a finite sum of Legendre polynomials,

$$P(\cos\Theta) = \sum_{\ell=0}^{N} \chi_\ell P_\ell(\cos\Theta) \tag{2.6}$$

where P_ℓ is the ℓ^{th} order Legendre polynomial and χ_ℓ are $N+1$ associated expansion coefficients.

The order of the expansion (N) is somewhat dependent on particle size since larger particles tend to be more anisotropic than smaller ones, thus requiring more terms in the expansion. To observe the normalization condition (2.5) requires a choice of quadrature directions in such a way that they define the number of terms in the expansion. For example, Guassian quadrature of order n produces a zero error in the integrals of the type (2.5) when $P(\cos\Theta)$ is represented by a polynomial of order $2n$. Therefore, with the

selection of 16 Gaussian angles, $N = 31$. Then, with the substitution of (2.6) into (2.5) and the expansion of this expression using the addition theorem for spherical harmonics, the phase function is represented by

$$P(\mu, \phi; \mu', \phi') = \sum_{m=0}^{N} \sum_{\ell=0}^{N} \chi_\ell^m \, P_\ell^m(\mu) \, P_\ell^m(\mu') \cos m(\phi' - \phi) \tag{2.7}$$

where

$$\chi_\ell^m = (2 - \delta_{o,m}) \frac{(\ell - m)!}{(\ell + m)!} \; \chi_\ell; \qquad \begin{cases} \ell = m, \ ..., \ N \\ 0 \leq m \leq N \end{cases}$$

and

$$\delta_{o,m} = \begin{cases} 1 & \text{for } m = 0 \\ 0 & \text{for } m \neq 0 \end{cases}$$

The interested reader is referred to (Liou, 1980, Appendix G) for the details of this expansion.

2.4 Henyey-Greenstein Phase Function and the Asymmetry Factor

It is often convenient to employ analytic functions to approximate the actual phase function. One of these which is widely used in the atmospheric science literature is the Henyey-Greenstein phase function. This function is

$$P_{H-G}(\cos\Theta) = \frac{1 - g^2}{(1 + g^2 + g\cos\Theta)^{3/2}} \tag{2.8}$$

where g is the asymmetry factor. The asymmetry factor provides a measure of particle forward or backward scattering and is defined by

$$g = 1/2 \int_{-1}^{+1} P(\cos\Theta) \cos\Theta d\cos\Theta = < \cos\Theta > \tag{2.9}$$

This parameter can be interpreted as a cosine weighted phase function. Values of g range from -1 for complete backscatter to 1 for complete forward scatter. As an example, large ice particles may have asymmetry factors exceeding 0.9 as a result of highly anisotropic scattering in the forward direction. When $g = 0$ either isotropic scatter exists or scattering is symmetric about $\Theta = 90°$ (as in the case of Rayleigh scatter). Use of the H-G phase function allows the expansion coefficients χ_ℓ in (2.7) to be defined conveniently as

$$\chi_\ell = (2\ell + 1) g^\ell; \quad \ell = m, ..., N, \quad 0 \leq m \leq N \tag{2.10}$$

2.5 The Fourier Expansion of the Radiative Transfer Equation

The diffuse intensity in equation (2.1) may also be represented by a Fourier cosine series; the expansion is of the form

$$I(\tau;\mu,\phi) = \sum_{m=0}^{2n-1} I^m(\tau;\mu)\cos m(\phi-\phi_o) \tag{2.11}$$

where ϕ_o defines a reference azimuth angle and

$$I^m(\tau;\mu) = \frac{1}{(1+\delta_{o,m})\,\pi}\int_0^{2\pi} I(\tau;\mu,\phi)\cos m(\phi-\phi_o)\,d\phi \tag{2.12}$$

With the substitution of (2.7) and (2.11) into (2.1) the integro-differential form of the radiative transfer equation is reduced to a linear system of $N+1$ independent equations:

$$\begin{aligned}\mu\frac{dI^m(\tau;\mu)}{d\tau} = -I^m(\tau;\mu) + (1+\delta_{o,m})\frac{\tilde{\omega}_o}{4}\sum_{\ell=m}^{N}\chi_\ell^m P_\ell^m(\mu)\int_{-1}^{+1} P_\ell^m(\mu')\,I^m(\tau;\mu')\,d\mu' \\ +\frac{\tilde{\omega}_o}{4}\sum_{\ell=m}^{N}\chi_\ell^m P_\ell^m(\mu)\,P_\ell^m(\mu_o)\,F_{o\lambda}\,e^{-\tau/\mu_o} \\ +\delta_{o,m}(1-\tilde{\omega}_o B_\lambda(T));\ m=0,1,\ldots,N\end{aligned} \tag{2.13}$$

where the last term is the thermal source which is zero for all but the $m=0$ (azimuthally averaged) solution. The m Fourier coefficients incorporate the azimuthal dependence in each of the amplitudes, $I^m(\tau;\mu)$ effectively uncoupling the equations in m. Thus (2.13) may be solved for $N+1$ independent amplitudes and the intensity determined from (2.11). The special case for azimuthally independent solutions results for $m=0$ and is commonly used for solving problems that require flux calculations. Note that (2.13) requires calculation of a new phase function for each Fourier coefficient thus requiring computer time proportional to the order of the expansion. Comparisons are presented in Chapter 5 which indicate that the assumption of azimuthal independence in the intensity field is reasonable for a wide range of satellite viewing angles. For the sake of numerical efficiency the azimuthally independent form of the radiative transfer equation was used in this study. The ensuing discussion applies to the azimuthally independent solution with the $m=0$ superscript deleted from the notation for convenience.

2.6 The Matrix equation of transfer

The integral in equation (2.13) can now be replaced using Gaussian quadrature to obtain a system of $2n$ first-order, nonhomogeneous differential equations. For a set of $2n$ quadrature points $(\pm\mu_j)$ on the interval $-1 < \mu_j < 1$ and weights w_j this system becomes

$$\begin{pmatrix} \frac{d\mathbf{I}^+}{d\tau} \\ \frac{d\mathbf{I}^-}{d\tau} \end{pmatrix} = \begin{pmatrix} -\mathbf{t} & \mathbf{r} \\ -\mathbf{r} & \mathbf{t} \end{pmatrix} \begin{pmatrix} \mathbf{I}^+ \\ \mathbf{I}^- \end{pmatrix} + \begin{pmatrix} \sum^+ \\ \sum^- \end{pmatrix} = \mathbf{S}\mathbf{I}^{\pm} + \sum^{\pm} \tag{2.14}$$

where $\mathbf{t}$ and $\mathbf{r}$ are matrices characterizing the localized transmission and reflection of an infinitesimally thin layer in the atmosphere and $\left(\sum^{\pm}\right)$ is the source vector for the various sources described in section 2.1 for that layer. The $\mathbf{t}$ and $\mathbf{r}$ matrices are determined by

$$\mathbf{t} = \mathbf{M}^{-1} - \frac{\tilde{\omega}_o}{2}\mathbf{M}^{-1}\mathbf{P}^{++}\mathbf{C}$$

$$\mathbf{r} = \frac{\tilde{\omega}_o}{2}\mathbf{M}^{-1}\mathbf{P}^{+-}\mathbf{C}$$

where $\mathbf{M}$ is an n by n diagonal matrix of quadrature points (μ_j) and $\mathbf{C}$ is an n by n diagonal matrix of quadrature weights (w_j), $j = 1, ..., n$. The $\mathbf{P}^{+-}$ and $\mathbf{P}^{++}$ are phase matrices for bidirectional reflection and transmission respectively. Equation (2.14) is the matrix equation of transfer for the azimuthally independent case. One way to solve (2.14) is to use linear algebra to obtain the characteristic eigenvalues and eigenvectors of the $\mathbf{S}$ matrix with given boundary conditions as described by Tsay (1986). Another method is more phenomenological in its approach and will be described below. It utilizes a finite difference form of (2.14) to deduce global transmission and reflection functions in terms of the localized $\mathbf{t}$ and $\mathbf{r}$ matrices already defined. Ultimately, the complex integro-differential form of the radiative transfer equation (2.1) can be reduced to a simple linear system involving only the boundary conditions and the gross radiative properties for an arbitrarily thick layer. That is, it is possible to determine the external response field of radiation without resolving the entire field within the layer or medium as demonstrated by Ambartsumian (1943).

2.7 The Interaction Principle

Clouds are tenuous in nature. Therefore, the effects of phase change, interference and diffraction of waves between individual particles can be ignored. Radiative transfer can be viewed more simply by linear interactions between radiation and matter; i.e., photons interacting with gaseous constituents, aerosols or cloud particles in the atmosphere. The addition of reflected and transmitted intensities rather than wave fields describe the radiation field about a point. Thus, the transfer of radiation through a multiple scattering plane-parallel horizontally homogeneous atmosphere can be described in terms of (global) diffuse reflectance (**R**) and transmittance (**T**) functions. These are matrices whose elements describe the bidirectional transfer of radiant energy by the layer for specific angle pairs. Together these functions provide a useful description of energy flow at the boundaries of the medium.

The **R** and **T** matrices are derived from the finite difference form of the matrix equation of transfer (2.14). For example the upward intensity for an infinitesimally thin layer $\Delta\tau$ is approximated by

$$\{\mathbf{I}^{+}(\Delta\tau) - \mathbf{I}^{+}(0)\} \approx \{-\mathbf{t}\mathbf{I}^{+}(0) + \mathbf{r}I^{-}(\Delta\tau)\}\,\Delta\tau + \sum^{+} \tag{2.15}$$

The global functions are defined as

$$\mathbf{T} = \mathbf{E} - \mathbf{t}\Delta\tau \quad \text{and}$$

$$\mathbf{R} = \mathbf{r}\Delta\tau \tag{2.16}$$

where **E** is an identity matrix and $\Delta\tau$ is taken to be very thin to insure that only single scattering takes place in the layer. For reflectance (**R**) the response opposes the incident beam. Transmittance (**T**) occurs when the response has the same sense as the incident beam, passing through the hemispheric boundary. If these matrices can be determined for the total optical depth of the layer, the desired response intensities at the boundaries are given by the sum of the reflected and transmitted incident intensities. The relationship is symbolically represented by the following pair of matrix equations:

$$\begin{vmatrix} \mathbf{I}_r^+ \\ \mathbf{I}_r^- \end{vmatrix} = \begin{vmatrix} \mathbf{R} & \mathbf{T} \\ \mathbf{T} & \mathbf{R} \end{vmatrix} \begin{vmatrix} \mathbf{I}_i^- \\ \mathbf{I}_i^+ \end{vmatrix} + \begin{vmatrix} \Sigma^+ \\ \Sigma^- \end{vmatrix} = \begin{matrix} \mathbf{R}\mathbf{I}_i^- + \mathbf{T}\mathbf{I}_i^+ + \Sigma^+ \\ \mathbf{T}\mathbf{I}_i^- + \mathbf{R}\mathbf{I}_i^+ + \Sigma^- \end{matrix} \tag{2.17}$$

where the last term in each equation is a vector representing the sum of the source terms described for equation (2.1). Equation (2.17) is a statement of the "Interaction Principle" which is central to all multiple scattering problems. Application of this principle in conjunction with knowledge of the bidirectional reflection and transmission functions and source vectors for adjacent layers in an atmosphere yield the radiation field at an internal level within the combined layer (say level τ within the layer between $\tau = 0$ and $\tau = \tau_1$ in Figure 2.2). These relationships are known as the principles of invariance (Chandrasekhar, (1960).

2.8 The Doubling and Adding Method, and Initialization

The above discussion focused on simulating the radiation field for a single infinitesimally thin layer in which single scattering was assumed. To account for multiple scattering in vertically homogeneous media of arbitrary thickness the doubling method is employed. The principles of invariance are used in conjunction with the interaction principle to determine the reflection and transmission functions for adjacent layers. These relationships are called "invariant imbedding relationships" or "doubling rules," examples of which are given in the literature. The radiation field for an arbitrarily thick layer may be determined from (2.14) once the **R** and **T** matrices have been built up by cyclic application of the doubling rules. Beginning with an infinitesimally thin slab ($\Delta\tau$), p-cycles will generate a slab $2^p\Delta\tau$ thick as illustrated in Figure 2.4. This method is numerically efficient and yields accurate results.

2.8.1 The Adding Method

Radiative transfer calculations for a vertically inhomogeneous atmosphere can be made by appropriately dividing it into several thin homogeneous layers, performing the doubling method on each and then adding successive layers to determine global **R** and

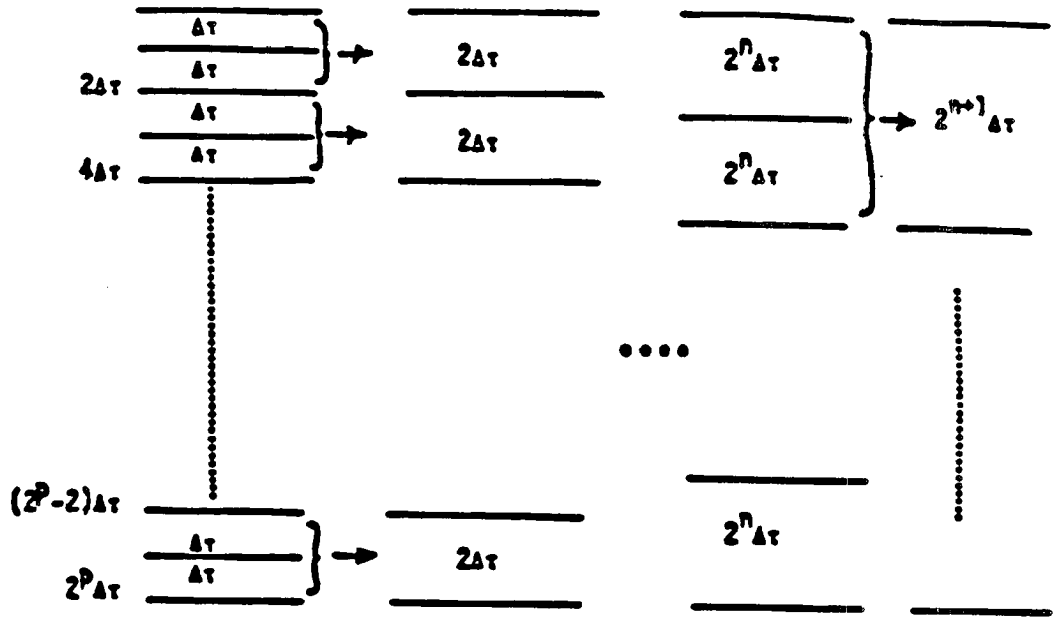

Figure 2.4: Schematic illustration of the doubling method.

T matrices for the entire atmosphere. This "adding method" is described by Stephens (1984).

The wavelengths used in this study are located in window regions of the spectrum; thus, absorption and emission within the intervening atmosphere between the surface and the cloud base are very weak and approximately equal in magnitude. These effects when differenced tend to cancel each other. Therefore, the assumption is made that a single vertically homogeneous cirrus layer resides in a vacuum eliminating the need for division of the atmosphere and the need to employ "adding".

2.8.2 Model Initialization

The accuracy of the doubling (and adding) method depends on the choice of incremental optical depth for which the procedure is initialized. Wiscombe (1976) discusses various initialization schemes and their associated errors. The simplest and most frequently used one was selected for use in this model. It is known as the Infinitesimal Generator Initialization (IGI). The basic criterion limiting the size of $\Delta\tau$ is that of non-negativity of all elements of the reflection and transmission functions which has obvious physical grounds.

Doubling preserves the property of non-negativity; therefore, once the process is properly initialized accurate results are assured. The "infinitesimal generator" ($\Delta\tau$) must meet the following criteria as discussed by Wiscombe (1976)

$$\Delta\tau \leq (\Delta\tau)_{max} = \min_{j} \left(\frac{\mu_j}{1 - \frac{1}{2}\tilde{\omega}_o P_{jj}^{++} C_j} \right); j = 1, \ldots, n$$

such that $2^p \Delta\tau$ gives the total optical depth of the layer after p-cycles.

In addition to knowing the infinitesimal generator, the radiative transfer model must be initialized for appropriate boundary conditions and the radiative parameters that characterize the cloud. Boundary conditions are wavelength dependent. For NIR-wavebands during the day the upper boundary condition is given by the solar flux over the bandwidth matching the sensitivity of the satellite radiometer. At night, the upper boundary condition becomes 0, ($F_{o\lambda} = 0$). For lw-calculations, the flux from above can be neglected as the atmosphere is too cold and thin to emit significant amounts of thermal energy. For both NIR and IR-calculations, the lower boundary condition is defined by the diffuse radiation field resulting from the Planckian emission at the surface ($B_\lambda(T_s)$) over the appropriate bandwidth; T_s being the surface temperature. Prescribed values for the radiative parameters are best understood in the context of the microphysical properties of the layer as discussed in the next chapter.

2.9 Chapter Summary

In general the integro-differential form of the radiative transfer equation (2.1) is difficult to solve. Simpler numerical methods employing quadrature formulae are commonly used to reduce (2.1) to a matrix form which accurately simulates the radiation field for a prescribed set of angles. The procedure requires appropriate discretization of the radiation field (to insure phase function normalization), and initialization of the doubling routine for an infinitesimal generator ($\Delta\tau$) which preserves the property of non-negativity for the reflection and transmission matrices.

Complete initialization of the radiative transfer model also requires knowledge of the cloud optical properties ($k_{ext}, \tilde{\omega}_o, g$ and the phase function) and boundary conditions.

Then, beginning with localized $\mathbf{r}$ and $\mathbf{t}$ matrices for $\Delta\tau$, global $\mathbf{R}$ and $\mathbf{T}$ functions are calculated and the principles of invariance are applied to set up invariant imbedding relationships. Implementation of the doubling routine for p-cycles yields the global $\mathbf{R}$ and $\mathbf{T}$ functions for the total optical depth of the layer. Finally, the Interaction Principle in the form of equation (2.17) gives the upward and downward monochromatic radiation field for the selected quadrature angles. The next chapter relates radiative parameters to cloud microphysics and wavelength. Graphic illustrations of their dependence on both are given for cirrus clouds.

Chapter 3

RADIATIVE PROPERTIES IN RELATION TO CLOUD MICROPHYSICS

The purpose of this chapter is to relate the main radiative properties introduced in Chapter 2 to microphysical characteristics of the cloud. For this purpose, the notion of microphysical models is introduced. These models will be used to aid in the understanding of how the scattering parameters and the extinction coefficient vary from microphysical model to model and also to demonstrate the dependence of these parameters on wavelength.

3.1 Ice Crystals; Observed and Simulated

The growth of ice crystals in the atmosphere is a complex process influenced by the temperature and moisture conditions of the environment. These conditions determine the distribution of particle shapes, sizes and phase. The shape of these particles further complicates the treatment of these clouds from the point of view of radiative transfer. Ice crystals are generally nonspherical and descend through the cloud with some preferential orientation in the horizontal plane (Platt, 1978). As a result of these microphysical inhomogeneities scattering parameters vary significantly within a cloud. Radiative transfer modelers are challenged by the need to develop accurate and efficient parameterization schemes for multiply scattering media varying in time and space.

3.1.1 Radiative Transfer in Anisotropic Media

Few investigators have undertaken the formidable task of making radiative transfer calculations for media composed of multiply scattering nonspherical ice particles. Two studies are noteworthy; both employ model clouds composed of long ice cylinders to approximate the columns and bullets that make-up a large percentage of cirrus clouds.

Liou (1974) investigated the transmission, emission and reflection characteristics of cirrus clouds in the lw-window region of the spectrum (8.3 - 12.5 μm) by simulating cloud composition using cylinders randomly oriented in space. Stephens (1980) compared shortwave reflection and absorption, and longwave emission and reflection for three different cloud compositions; cylinders randomly oriented in 3-dimensions, cylinders randomly oriented in 2-dimensions with preferential orientation in the horizontal plane and equivalent spheres. He approximated the radii of equivalent spheres by

$$R_e = \left(\frac{A}{4\pi}\right)^{1/2} \tag{3.1}$$

where A is the surface area of the cylindrical particle.

Stephens' investigation theoretically quantified differences in transmission, emission and reflection for a variety of hypothetical clouds. He concluded that it is important to incorporate the scattering effects of nonspherical ice particles in radiative transfer calculations. He also demonstrated a dependence of these properties on crystal orientation. In particular, significant differences resulted for cloud albedo and shortwave absorption between clouds with preferred crystal orientation and those composed of crystals randomly oriented in 3 dimensions.

Solving radiative transfer problems in anisotropic media is mathematically complicated and requires the use of powerful computers. To simplify the problem for this study, ice crystals are approximated by equivalent spheres. Numerical algorithms based on Mie theory can then be used to calculate radiative properties for polydispersed size distributions. Mie theory will not be treated in detail here, but an introduction to the subject is warranted.

3.2 Scattering by spheres (Mie theory)

Mie theory describes the scattering properties of spheres over a broad range of sizes and refractive indices. Van de Hulst's treatise on the subject (1957) is required reading for those interested in the detailed mathematical functions that describe the intensity and polarization of scattered light. A few characteristics of Mie scattering have particular relevance to this study. These are summarized below.

Mie scattering for a monodispersion of particles can be characterized by:

- A complicated dependence of scattered light intensity on the angle of observation, the complexity increasing with particle size relative-to-wavelength.
- An increasing ratio of forward scattering to backscattering as the particle size increases, with resulting growth of the forward scattering lobe as illustrated in Figure 3.1.
- Little dependence of scattering on wavelength when particle size relative-to-wavelength is large.

"Size relative-to-wavelength", expressed as the size parameter, $\chi = \frac{2\pi r}{\lambda}$, is an important factor controlling scattering phenomena; i.e., the scattering parameters ($\tilde{\omega}_o, g$ and k_{ext}) are a function of the interrelationship of microphysics (particularly size) and wavelength. Scattering properties of a polydispersion such as typically occurs in the real atmosphere are treated by integrating the scattering properties of the single particle weighted by an appropriate size distribution function.

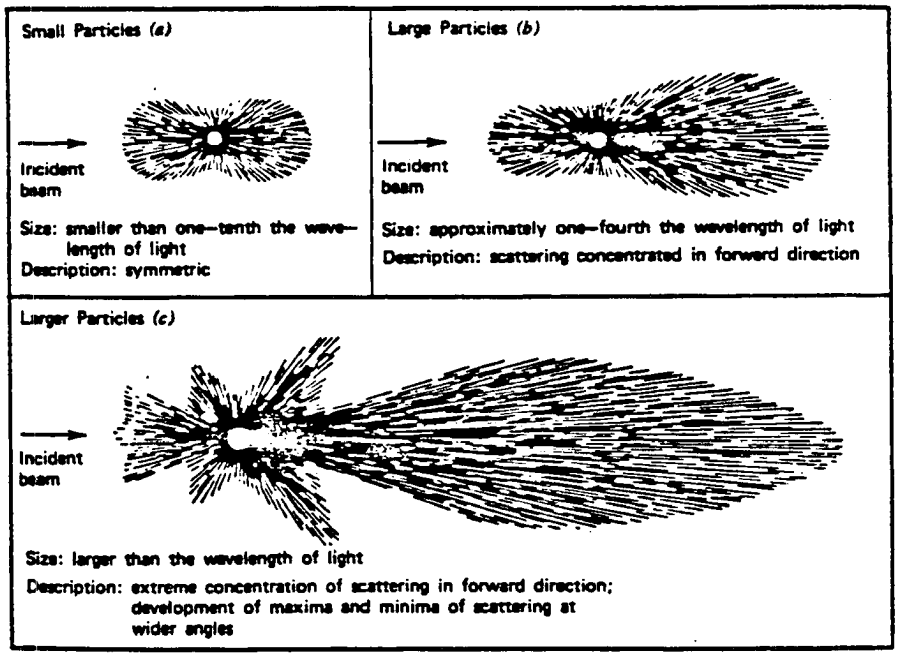

Figure 3.1: Angular patterns of scattered intensity from particles of three sizes. (a) Small particles, (b) large particles, (c) larger particles (Brumberger et al.,1968).

The scattering patterns pictured in Figure 3.1 (b) and (c) characterize the range of spherical ice particles used here to simulate cirrus composition. The growth of the forward lobe as a function of increasing size parameter is represented by an increase in the asymmetry factor ($g \rightarrow 1$). This is further demonstrated in the following section which includes plots of cloud optical properties versus particle radii.

3.3 Applications of Mie Theory and Microphysical Models

For the purpose of this research the total extinction coefficients (k_{ext}), single scattering albedos ($\tilde{\omega}_o$) and asymmetry factors (g) needed to initialize the radiative transfer model were calculated using a Mie algorithm written by Wiscombe (1980). His program is available for use on the NCAR Cray computer. It was used to develop a table of microphysical models characterizing cirrus clouds. Each entry in these tables give a microphysical description of a hypothetical ice cloud and includes a list of associated optical properties for that cloud. The effective radius, volume density, temperature, particle size distribution and wavelength must be prescribed before optical properties can be determined from the Mie code. This procedure follows closely that of Arking and Childs (1985) who developed a technique to retrieve cloud cover parameters from multispectral satellite images.

3.3.1 Selection of Microphysical Models

The microphysical models were designed to span a broad range of physical and microphysical conditions in the atmosphere. In nature, combinations of these properties are unlimited making any choice of model somewhat arbitrary. An effort was made to select combinations of properties consistent with the observations of Heymsfield (1975a) and Heymsfield and Platt (1984). For instance, ice water content (IWC) is observed to decrease by approximately two orders of magnitude over temperatures ranging from $-20°$ to $-60°C$ (See Figure 1.6). IWC is proportional to the volume of particles integrated over their size distribution.

$$IWC = \left(\frac{4\pi}{3}\right) \rho_i \int_o^\infty r^3 n(r)\, dr \tag{3.2}$$

where

- $n(r)dr$ is the number of particles per unit volume with radii in the interval $(r, r+dr)$, and
- $\rho_i \equiv$ ice density which is temperature dependent.

The integral of $n(r)$ over all particle radii defines the total concentration (N). Heymsfield and Platt (1984) observed a general tendency for N to decrease with decreasing temperature, especially for larger crystals with their maximum dimension exceeding 200 microns. They also observed that maximum crystal dimension decreases with temperature. Therefore, volume density, IWC, temperature and particle size are interrelated. Based on the observations of Heymsfield and Platt, five microphysical models were constructed.

The following modified gamma distribution of particle sizes was used in this study

$$n(r) = \frac{N(ab)^{(2b-1)/b}}{\Gamma[(1-2b)/b]} r^{(1-3b)/b} e^{-[r/(ab)]} \tag{3.3}$$

a and b were taken as the mean effective radius and effective variance defined by Hansen (1971). a is defined as

$$a = < r >_{eff} = \frac{\int_0^\infty r \pi r^2 n(r)\, dr}{\int_0^\infty \pi r^2 n(r)\, dr} \tag{3.4}$$

Here, cross-sectional area (πr^2) is used as a weighting factor to account for particle scattering (which is proportional to area). b is given by

$$b = v_{eff} = \frac{\int_0^\infty (r - < r >_{eff})^2 \pi r^2 n(r)\, dr}{< r >_{eff}^2 \int_0^\infty \pi r^2 n(r)\, dr}, \tag{3.5}$$

Each microphysical model was assigned a numeric index referred to as a microphysical index (MP-index). Table 3.1 lists the mean effective radii, temperatures and volume densities selected for each of these indices.

Tables 3.2 and 3.3 list the microphysical models and their radiative properties for the respective VAS and AVHRR channels used in this study. The Hansen size distribution (3.3) with an effective variance of 0.1 was used to initialize the Mie code for each of the MP-indices listed in Table 3.1. The real and imaginary parts of the refractive indices for spherical ice particles are listed below each table for their appropriate wavelengths.

Table 3.1

Table 3.1: Effective radii, Temperature and Volume Density for Microphysical Models.

MP-INDEX	1	2	3	4	5
$R_{eff}(\mu m)$	4	8	16	32	64
TEMP (K)	218	223	228	248	248
TEMP (C)	-55	-50	-45	-25	-25
Total Vol. Dens. (cm^{-3})	1.5	1.0	0.5	0.1	0.05

Table 3.2

Table 3.2: Microphysical Parameters for Spherical Ice Particles (for GOES-6 visible and VAS channels 12, 8 and 7 respectively).

MP-INDEX	R_{eff} (μm)	λ (μm)	(k_{ext}) (cm^{-1})	($\tilde{\omega}_o$)	(g)	IWC (g m^{-3})
1	4	0.65	1.1885E-6	0.999999	0.846124	2.655E-4
		3.94	1.7438E-6	0.928954	0.806763	
		10.82	5.4273E-7	0.208766	0.744374	
		12.66	1.0908E-6	0.363152	0.669144	
2	8	0.65	3.0656E-6	0.999998	0.865524	1.416E-3
		3.94	3.4824E-6	0.831526	0.789130	
		10.82	2.2141E-6	0.336256	0.898088	
		12.66	3.5607E-6	0.445900	0.836737	
3	16	0.65	6.0030E-6	0.999996	0.877276	5.664E-3
		3.94	6.5185E-6	0.734791	0.875587	
		10.82	5.5984E-6	0.430838	0.951485	
		12.66	6.9534E-6	0.481718	0.899611	
4	32	0.65	4.7388E-6	0.999992	0.884436	9.062E-3
		3.94	4.9903E-6	0.632908	0.925130	
		10.82	4.8216E-6	0.479032	0.970133	
		12.66	5.2702E-6	0.512960	0.922728	
5	64	0.65	9.3991E-6	0.999984	0.888586	3.625E-2
		3.94	9.7117E-6	0.561697	0.955140	
		10.82	9.6936E-6	0.502951	0.977084	
		12.66	1.0116E-5	0.535438	0.931124	

Spectral indices of refraction are listed below:

Spectral center (microns)	real (n)	imaginary (n')
00.650	1.3080	1.430E-8
03.945	1.3670	8.684E-3
10.818	1.0888	1.876E-1
12.660	1.4154	4.123E-1

Table 3.3

Table 3.3: Microphysical Parameters for Spherical Ice Particles (for the NOAA-9 AVHRR channels 1, 3 and 4)

MP-INDEX	R_{eff} (μm)	λ (μm)	(k_{ext}) (cm^{-1})	($\tilde{\omega}_o$)	(g)	IWC (g m^{-3})
1	4	0.69	1.1937E-6	0.999998	0.843755	2.655E-4
		3.73	1.6776E-6	0.934408	0.772376	
		10.82	5.4273E-7	0.208766	0.744374	
2	8	0.69	3.0724E-6	0.999997	0.864351	1.416E-3
		3.73	3.4494E-6	0.850004	0.783163	
		10.82	2.2141E-6	0.336256	0.898088	
3	16	0.69	6.0115E-6	0.999994	0.876846	5.664E-3
		3.73	6.4857E-6	0.762376	0.864643	
		10.82	5.5984E-6	0.430838	0.951485	
4	32	0.69	4.7432E-6	0.9999987	0.884314	9.062E-3
		3.73	4.9758E-6	0.659754	0.913918	
		10.82	4.8216E-6	0.479032	0.970133	
5	64	0.69	9.4046E-6	0.999975	0.888603	3.625E-2
		3.73	9.6946E-6	0.577796	0.947356	
		10.82	9.6936E-6	0.502951	0.977084	

Spectral indices of refraction are listed below:

Spectral center (microns)	real (n)	imaginary (n')
00.690	1.3071	2.400E-8
03.727	1.3951	6.899E-3
10.818	1.0888	1.876E-1

The information contained in the microphysical tables is easier to interpret in graphical form. Plots were produced only for the AVHRR window channels. Corresponding VAS channels would be very similar. The following three figures (Figure 3.2, Figure 3.3, and Figure 3.4) illustrate the general properties of Mie scattering as a function of effective radius for the two wavelengths, 10.8 and 3.7 μm (refer again to section 3.2). The plotted points correspond to actual values computed (from the Mie code) for each microphysical model. Curves have been fit merely for visual interpretation.

Inspection of these plots reveal interesting features of scattering by ice spheres. For example, Figure 3.2 shows an increase in asymmetry factor with increasing radius. This indicates a more pronounced forward scattering lobe as particles become large. Figure 3.3 shows how the single scattering albedo converges toward 0.5 as particle size increases. Large particles intercept an amount of energy proportional to their cross-sectional area removing that amount of energy from the incident beam by absorption. An equal amount of energy is removed by diffraction of the incident rays around the surface of the particle. Therefore, the total extinction (κ_{ext}) is proportional to twice the geometric cross-sectional area, whereas the scattering coefficient (κ_{sca}) is proportional only to the cross-sectional area. Therefore, definition, $\tilde{\omega}_o$ asymptotically approaches 0.5 as the geometric limit is approached. A similar argument holds for the asymptotic nature of the total extinction coefficient with increasing particle size as shown in Figure 3.4. The extinction efficiency approaches 2 regardless of wavelength for $\chi >> 1$.

One other characteristic of Mie scattering requires elaboration, this being the increasing complexity of the scattering phase function as the size parameter increases. Examples are given in the following section to illustrate this point.

3.3.2 Phase Function Revisited

The complex variation of the phase function with scattering angle depends to some extent on the magnitude of the particle absorption. This absorption is related to the imaginary part of the refractive index (n'). n' for ice is orders of magnitude greater for far infrared wavelengths than in the visible to near infrared wavelengths. For the wavelengths

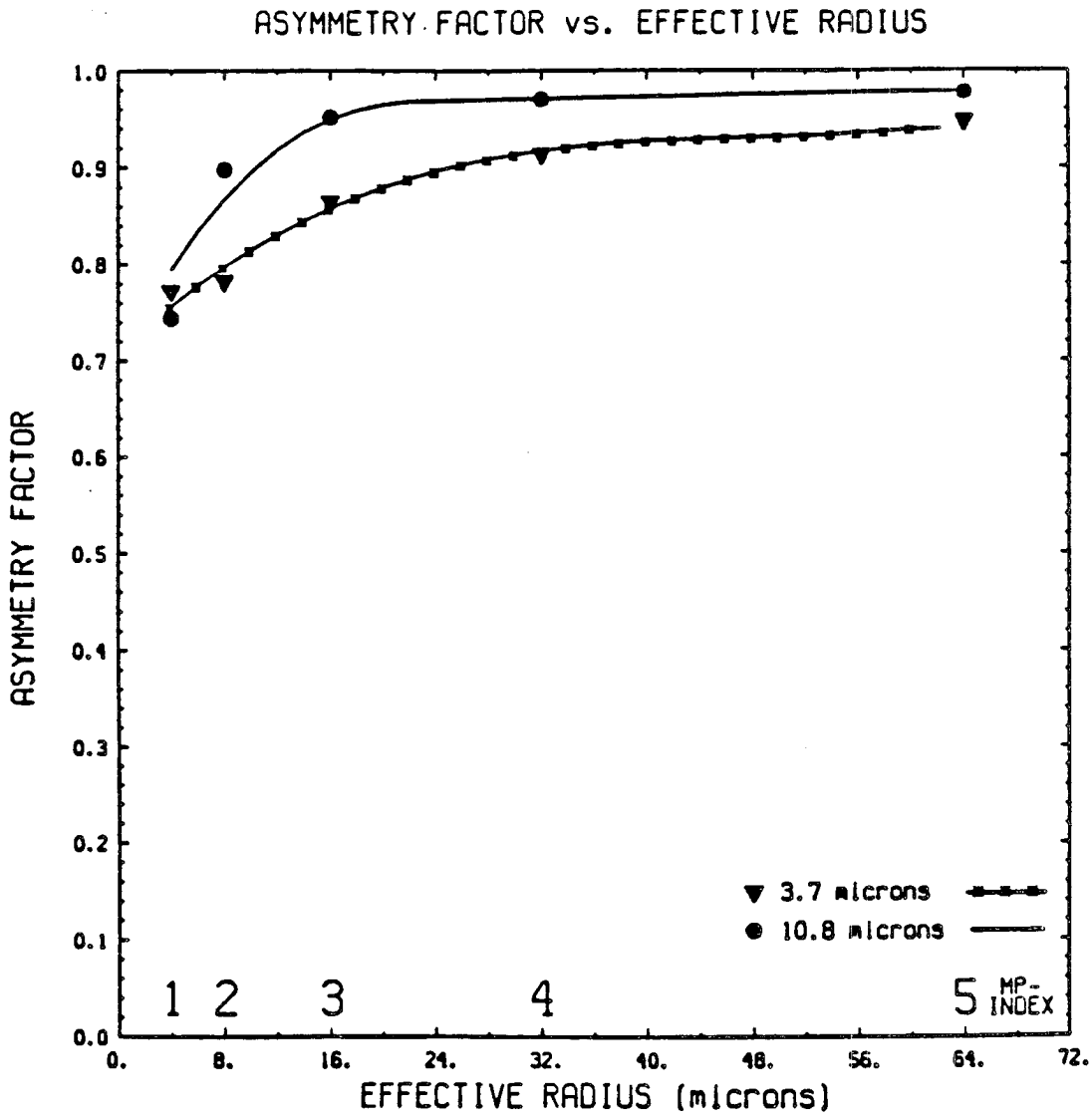

Figure 3.2: The behavior of the asymmetry factor as a function of effective radius for 3.7 and 10.8 micron wavelengths.

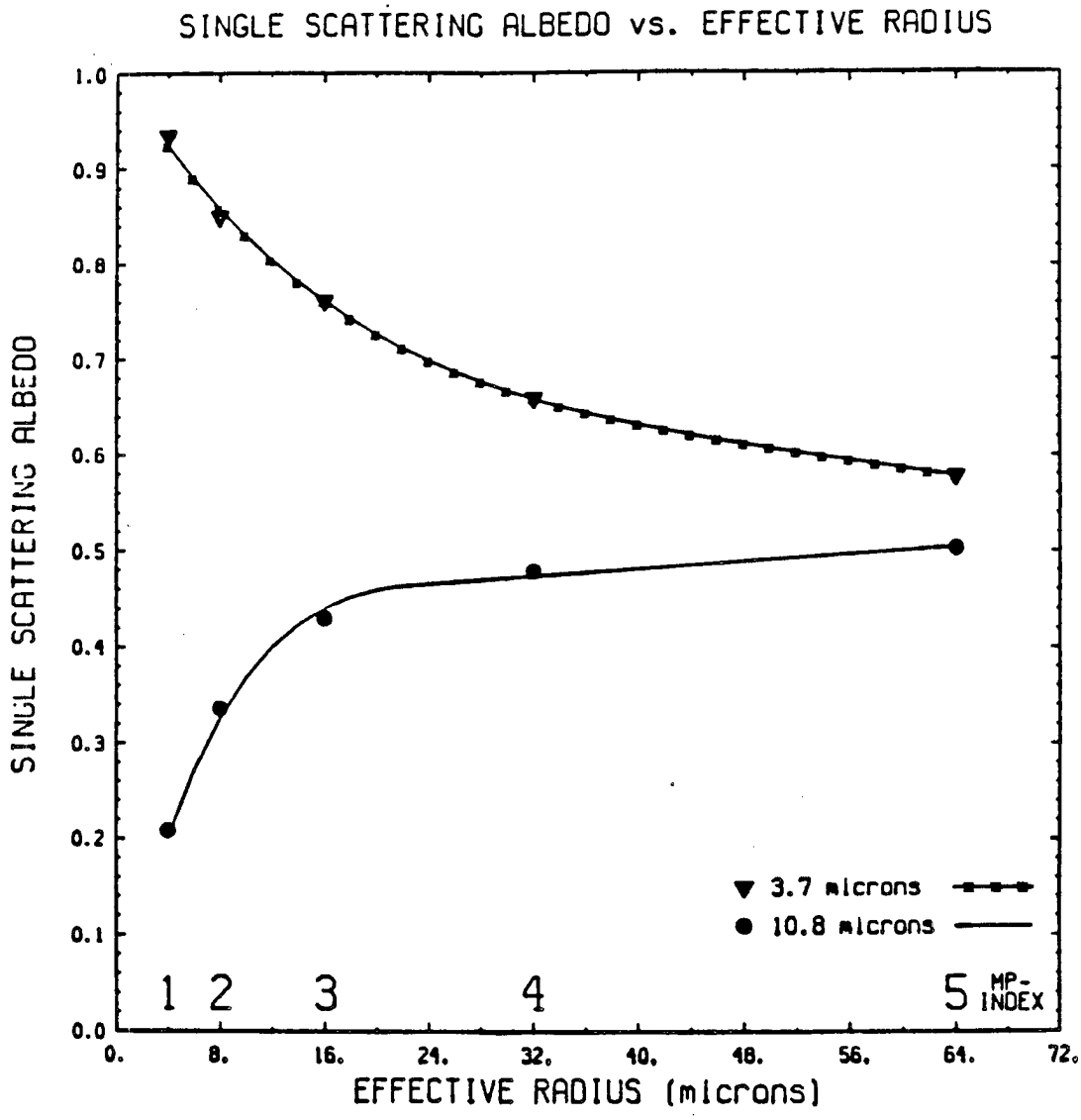

Figure 3.3: The behavior of the single scattering albedo as a function of effective radius for 3.7 and 10.8 micron wavelengths.

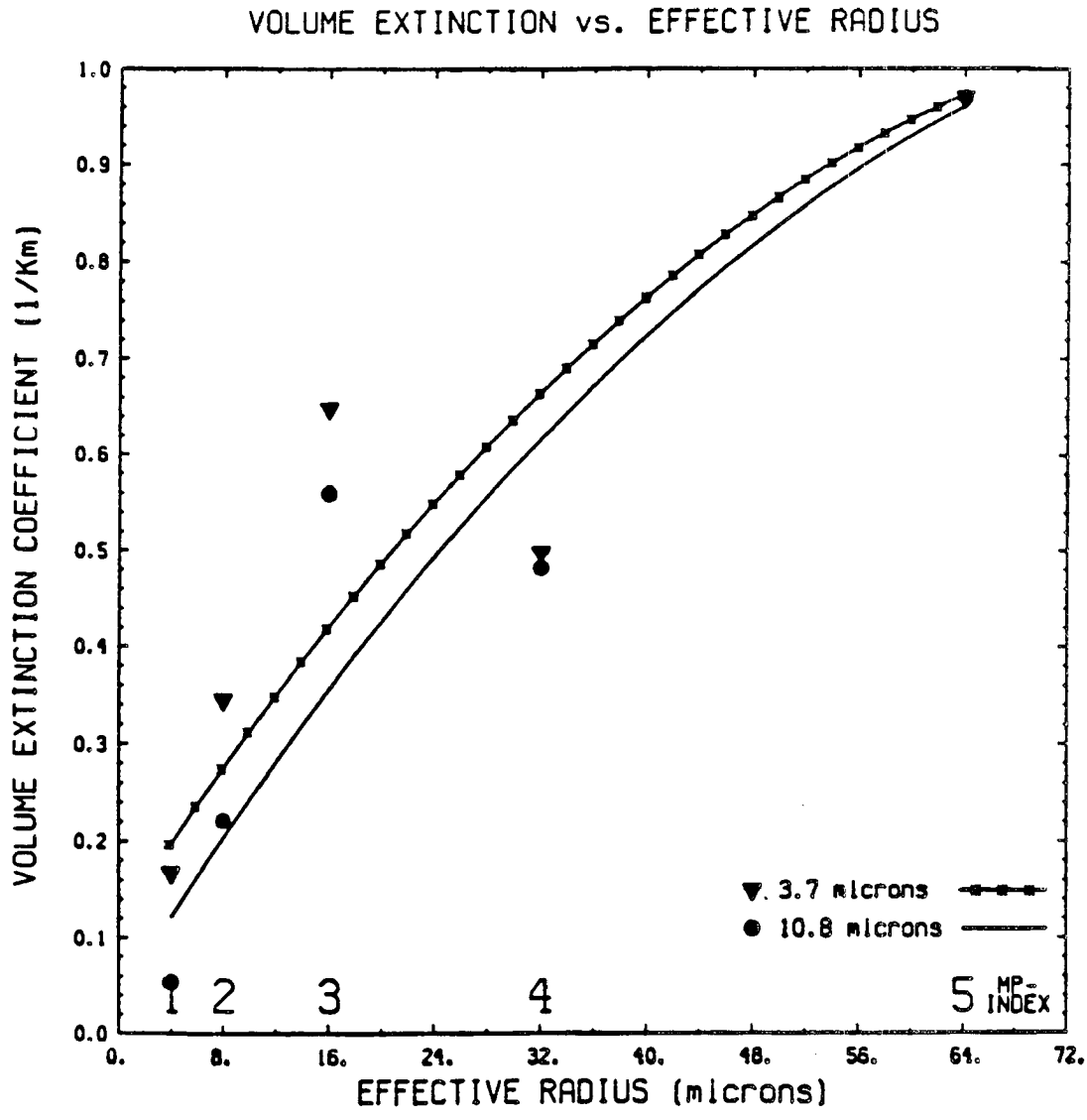

Figure 3.4: The behavior of the total extinction coefficient as a function of effective radius for 3.7 and 10.8 micron wavelengths.

of interest here, a given size particle will absorb more longwave energy (scatter less), and scatter more near infrared energy (absorb less). A small but significant portion of the additional scattering for the shorter wavelengths is backscattered. It is the combination of the strong forward peak and backscattered intensity that gives rise to complex phase functions as particle size relative to wavelength increases for any given wavelength. Figures 3.5 (a) and (b) show plots of the phase function vs. scattering angle for a particle distribution with an effective radius of 32 microns for two respective size parameters of approximately 16 and 51. Both the Mie phase function and the analytic Henyey- Greenstein approximation are shown for comparison. Since the two Henyey- Greenstein curves are monotonically decreasing functions of similar asymmetry factors little difference between them will be noted. However, the respective phase functions derived from Mie theory are dissimilar. Figure 3.5 (b) exemplifies the complexities of the large forward peak and backscatter intensity discussed above.

The Henyey-Greenstein approximation is sufficiently accurate for radiative transfer applications involving simple scattering patterns, but for large size parameters it underestimates the forward and backscattering peaks. Forward scattering peaks associated with halos at 22° are also poorly represented by the Henyey-Greenstein function. Use of combined Henyey-Greenstein functions and delta functions may be used to improve the accuracy of the approximation relative to the Mie phase function in these situations (AT-721 class notes, Stephens, 1986).

The Henyey-Greenstein phase function in the form of its Legendre Fourier expansion was used in the radiative transfer model for this study. The Fourier expansion results from substituting (2.10) into (2.6) to give

$$P_{H-G}(\cos\Theta) = \sum_{\ell=0}^{N} (2\ell+1)\, g^{\ell} P_{\ell}(\cos\Theta) \tag{3.6}$$

The disadvantage of underestimating the forward and backward peaks using (3.6) instead of the actual Mie phase function in radiative transfer calculations is somewhat offset by the advantages of increased numerical efficiency and reduced accumulation of numerical errors during computation as explained below.

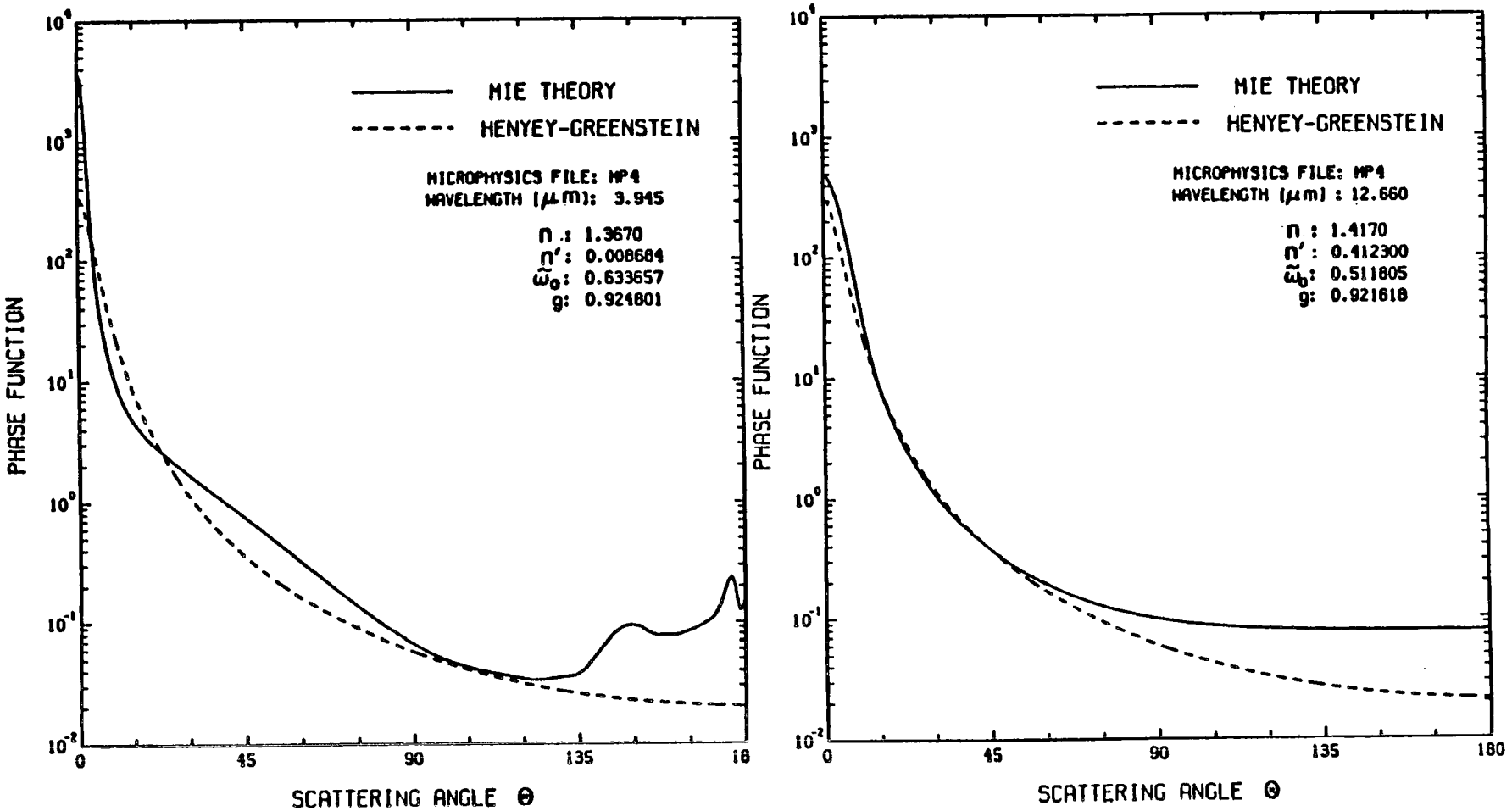

Figure 3.5: Plots of the Mie and Henyey-Greenstein phase functions for size parameter of (a) approximately 16 and (b) approximately 51.

Recall that for large effective radii a greater number of quadrature angles is required to simulate the radiation field requiring more terms in the Fourier series expansion of the phase function. Solutions are therefore more costly to obtain as these parameters increase in value. Also, when more quadrature points are used, the reflection and transmission matrices are proportionately larger increasing the potential for truncation and round-off errors during matrix operations which tend to degrade the accuracy of the radiative transfer calculations.

Another important point in regard to this particular study, is the fact that for typical satellite viewing angles relative to incident intensities, scattering is either closely approximated by the Henyey-Greenstein function or is underestimated by the same order of magnitude for the different wavelengths being compared. Therefore, analyses involving the differences of brightness temperatures (or radiances) determined from the Henyey-Greenstein approximation tend to cancel errors associated with the individual cases.

The asymmetric nature of the phase function associated with the prominent forward scattering lobe for large particles requires further attention. A procedure known as the Delta-M Method developed by Wiscombe (1977) was used in this model to compensate for the great magnitude of the forward peak. This involves rescaling the asymmetry factor, optical depth and single scattering albedo to effectively reduce this forward peak, thus allowing the use of fewer quadrature points and fewer terms in the Fourier representation of the phase function resulting in greater numerical efficiency. The interested reader is referred to Wiscombe's article for the details of his method.

This chapter has stressed the importance of understanding the physical and microphysical characteristics of cirrus clouds in order to determine realistic values of cloud optical properties required to initialize the radiative transfer model. It is clear that the task of developing a radiative transfer model to accurately simulate the radiation field for an absorbing-emitting and anisotropically scattering medium with internal thermal sources, which is also capable of parameterizing the inherent inhomogeneities of microphysical and radiative properties in space and time is a horrendous undertaking. Many simplifying assumptions have necessarily been made in this study to keep the problem

mathematically simple and numerically efficient. Results of applying the theory outlined in Chapter 2 and in this chapter will be presented in Chapter 5. But first an overview of satellite radiometry will be given to provide an observational perspective for interpreting these theoretical calculations.

Chapter 4

REMOTE SENSING AND MULTISPECTRAL IMAGERY

Remote sensing from space and ground-based platforms provides valuable information about the physical and radiative properties of the earth-atmosphere system. In particular, analysis of multispectral satellite imagery (MSI) is useful for a variety of cloud studies. Reynolds and Vonder Haar (1977) demonstrated how spectral differencing of image pairs could be used to discriminate among different cloud types utilizing objective threshold techniques. In this study the difference between image pairs for two window regions of the spectrum are related to cloud optical depth. This relationship is exploited as a technique for determining the presence of thin clouds and as a means to estimate values for the radiative properties of these clouds.

The use of remote sensing for meteorological research requires some knowledge of how radiometric measurements are made and processed. This chapter introduces various concepts of radiometry and image processing that are used in the analyses described in Chapter 6.

4.1 Satellite Radiometric Measurements and Image processing

Radiometry is a discipline concerned with spectral measurements of radiant energy. It has particular application to cloud imaging and atmospheric sounding from remote platforms such as those aboard geostationary or polar-orbiting satellites. A comprehensive overview of satellite meteorology is found in the lecture notes of Vonder Haar and Hillger (1984).

A satellite radiometer is a passive sensing device designed to measure radiant power (Pr). The amount of power received is a function of the instrument's field of view (FOV),

the satellite's position, and the radiance (N_s) emitted by the surface area (A_s) as illustrated in Figure 4.1. This relationship is given by

$$Pr = A_s \omega_s N_s(\gamma) \cos\gamma = A_c \omega_c N_s \quad \text{(in Watts)} \tag{4.1}$$

where

- ω_s is the solid angle for a point on the surface subtending the instrument's aperture (A_c)
- γ is the viewing angle relative to the local vertical, and
- ω_c is the solid angle subtending A_s

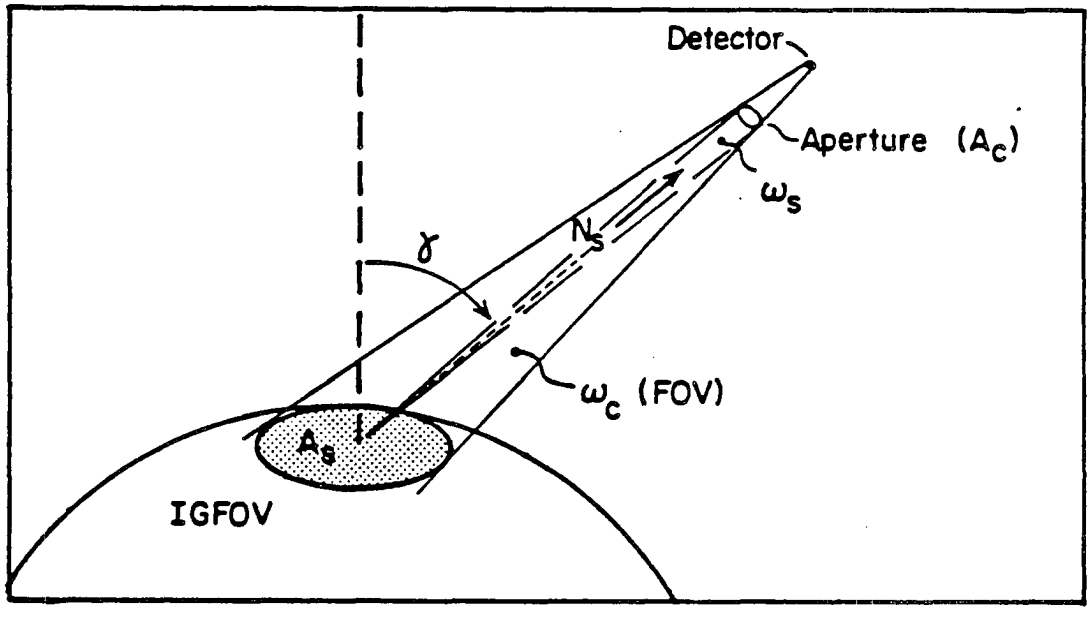

Figure 4.1: Geometric configuration for remote sensing of surface radiance (Adapted from Vonder Haar and Hillger, 1984).

Equation (4.1) relates measured power to two known instrument parameters (A_c and ω_c) and can be used to solve for the unknown surface radiance in W m^{-2} sr^{-1} over the spectral range of the instrument.

For visual interpretation of the entire field of coverage it is necessary to convert raw analog power (or intensity) measurements to digital signals which can be transmitted to ground receiving stations for processing.

4.1.1 Data Processing, Acquisition and Display System at CSU

The radiant power detected by a satellite sensor is converted to an output voltage and then digitized to an integer count value, normally an 8-bit number in the range 0 - 255. Each count value corresponds to a weighted integrated radiance for the aperture FOV or instantaneous geometric field of view (IGFOV) at the surface. The satellite transmits a stream of digital counts, navigation information, etc. to a receiving station where it is processed and either transmitted via a land-line or retransmitted to a geostationary communications satellite which then transmits to local receiving stations. The Colorado State University (CSU) satellite ground station is such a site. It is connected to the GOES-TAP which is an image distribution system operated by the National Environmental Satellite and Data Information Service (NESDIS) giving CSU the capability of receiving MSI data in near real time.

Researchers generally sectorize images from raw data files to extract smaller regions of particular interest. Final processing produces the desired digitized images for display. An Interactive Research Imaging System (IRIS) and various computer programs are available at the CSU ground station to assist in interpretation of the imagery. Images can be enhanced, smoothed (to reduce blockiness of large IR pixels), enlarged, combined, overlaid with navigated geopolitical plots, etc. to achieve specific research goals. As noted earlier, infrared satellite images are commonly interpreted in terms of equivalent blackbody temperatures (or brightness temperatures). Visible images, on the other hand, are interpreted in terms of albedo. Look-up tables are used to convert count values to either brightness temperature or albedo to obtain the radiative properties of the cloud field. Such data can be used in various ways to derive information about the types and distribution of the

clouds. For instance, bidimensional histograms of IR brightness temperature versus visible albedo are often used for classifying cloud types using objective statistical methods. These methods are based on the identification of the spectral signatures associated with clusters of points on the histogram, each defining a cloud type. In recent years many investigators have developed objective cloud classification schemes and/or algorithms to determine cloud cover parameters. Desbois et al. (1981) analyzed three dimensional histogram of images utilizing an additional IR channel to overcome the "indeterminancy" which arises in distinguishing semi-transparent clouds. Platt (1983) also addressed this problem, but employed a bispectral method similar to that of Reynolds and Vonder Haar (1977). Others have concentrated their efforts on detecting and allowing for partially filled fields of view; Coakley and Bretherton (1982) developed a "spacial coherence method" which employs only IR imagery providing results for night as well as daytime observations. As the clouds in this study are readily identifiable, further details of these statistical methods are left for the reader to explore.

Two types of satellites provide most of the data used for operational weather forcasting and meteorological research: geostationary and polar-orbiting. These are equipped with multi-channel scanning radiometers.

4.2 Scanning Radiometers and Multispectral Imaging

Multispectral scanning radiometers are designed to measure radiance in both the visible and several IR wavebands simultaneously. This is accomplished by utilizing various sensor arrays and rotating spectral filters. Two types of radiometers are in commom use: a line-scan instrument mounted on polar-orbiters and a spin-scan device incorporated in geostationary satellites. Such devices were used to collect the images analyzed later in this paper.

4.2.1 The Line Scan Radiometer; NOAA-9, AVHRR Instrument

NOAA-9, launched on Dec. 12, 1984, is one of the operational polar-orbiting environmental satellites of the TIROS-N series (1978-1984). It is in sun-synchronous orbit at an altitude of approximately 850 km with a period of 102 minutes (making 14.1 revolutions

per day). It is equipped with an Advanced Very High Resolution Radiometer (AVHRR) which is a line-scan device having five channels sensitive to visible, near infrared and infrared radiation. Table 4.1 lists the design features of this instrument.

Table 4.1

Table 4.1: Characteristics of the NOAA-9 AVHRR instrument (Adapted from "Satellite and Their Data", CIRA and AMS, 1982).

Channel	1	2	3	4	5
Spectral Range (μm)	0.58-0.68	0.725-1.1	3.55-3.93	10.3-11.3	11.5-12.5
Detector type	Silicon	Silicon	InSb	HgCdTe	HgCdTe
Resolution (km)	1.1	1.1	1.1	1.1	1.1
IFOV ($m\gamma$)	1.3	1.3	1.3	1.3	1.3
* NEdT at 300 K	-	-	0.12	0.12	0.12

* NEdT is the noise equivalent differential temperature.

The AVHRR obtains global coverage by continuously scanning from horizon to horizon perpendicular (crosstrack) to the satellite's direction of motion. Each scan line consists of image elements produced as a mirror rotates at a fixed angular rate. One element in a line is called a pixel. The mirror's angular position and rotation rate combined with the forward motion of the satellite determine the pixel size. The size of the pixel determines image resolution which varies with the nadir angle of the FOV. The resolution of an AVHRR image is 1.1 km at the satellite subpoint, but decreases (with increasing pixel size) as the nadir angle or distance from the subpoint increases. This causes foreshortening near the horizons which leads to image distortion requiring correction by some remapping procedure. Figure 4.2 illustrates this feature of polar-orbiting satellites. Additional information regarding the design and performance of the AVHRR can be found in the CIRA and AMS bulletin, Part I, "Satellite and their Data" (1982).

4.2.2 The Spin Scan Radiometer; GOES-6, VAS Instrument

GOES-6 (Geostationary Operational Environmental Satellite) is one of several Synchronous Meteorological Satellites (SMS, 1974-present) owned and operated by the National Oceanic and Atmospheric Administration (NOAA). The satellite is positioned above

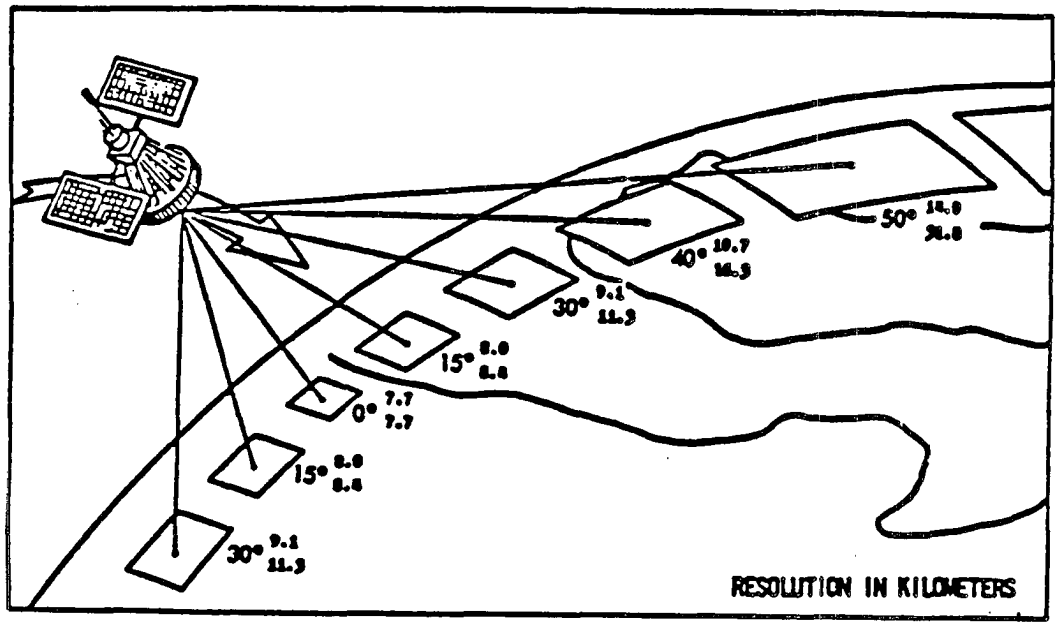

Figure 4.2: Ground resolution of Nimbus-5 Temperature-Humidity IR Radiometer (THIR), (from Vonder Haar and Hillger, 1984).

the equator at a synchronous altitude of 35,800 km and remains stationary relative to a fixed subpoint. GOES-6 is equipped with an improved Visible and Infrared Spin Scan Radiometer (VISSR) called VAS (VISSR Atmospheric Sounder). With its complex array of detectors and selectable narrow-band optical filters it is capable of sensing in the visible and twelve IR wavebands from the NIR-window region to about 15 μm. Channels were selected to distinguish the effects of tropospheric temperature, moisture and cloud cover on upwelling radiances (Chesters and Robinson, 1983). Table 4.2 lists the spectral characteristics of the VAS channels.

Spin scan imaging is accomplished by stepping a scan mirror in north-to-south (N-S) angular increments of 0.192 mr as the entire satellite rotates about its axis which is spin-stabilized perpendicular to the earth's equatorial plane. The satellite spins at 100 rpm producing a west-to-east (W-E) scan line for each step of the mirror. Line elements result from a W-E axis scan step corresponding to the IGFOV of the detectors. 1821 latitude steps are required to scan the total field covering approximately $\pm 70°$ in longitude and $\pm 72°$ in latitude relative to its equatorial subpoint. Two such images are produced

Table 4.2

Table 4.2: Spectral Characteristics of the GOES-6 VAS Channels (Adapted from Chesters and Robinson, 1983).

VAS Channel Number	Spectral Filters		
	center	center	width
	μm	cm^{-1}	cm^{-1}
1	14.730	0678.7	10.0
2	14.480	0690.6	16.0
3	14.250	0701.6	16.0
4	14.010	0713.6	20.0
5	13.330	0750.0	20.0
6	04.525	2210.0	45.0
7	12.660	0790.0	20.0
8	11.170	0895.0	140.0
9	07.261	1377.0	40.0
10	06.725	1487.0	150.0
11	04.444	2250.0	40.0
12	03.945	2535.0	140.0

each hour. Other modes of operation permit higher viewing frequency of smaller regions for monitoring severe weather phenomena (rapid-scan mode) or vertical sounding of the atmosphere (dwell-sounding mode), (refer to Clark, 1983 for additional information).

VAS resolution is determined by the size and array of visible and IR detectors. A linear array of eight visible detectors sweep any given line of an image to give an IGFOV at subpoint of 0.9 km. An arrangement of six infrared detectors of different sizes and materials enables imaging in three channels simultaneously. This is accomplished by selective use of filters and "interweaving scans of either large and small detectors" as described by Clark (1983). Subpoint resolution is 6.9 km for the small detectors (0.192 mr) and 13.8 km for the large detectors (0.384 mr). It is important to note that both the W-E and N-S pixel dimensions increase as the nadir angle increases from subpoint toward the horizons or higher latitudes respectively.

4.3 Problems of Image Interpretation

The previous discussion revealed an inherent problem of scanning radiometers; that of decreasing resolution as the distance from the satellite subpoint increases (Figure 4.2).

Another problem related to nadir angle is locating image pixels relative to ground-based navigation coordinates, especially for high clouds located large distances from the subpoint. Ambiguous location of image features may also result from slow detector response time relative to a rapid scan rate of the instrument. These problems are outlined briefly below.

4.3.1 Mislocation of Cloud Tops

Figure 4.3 illustrates the problem of locating cloud tops relative to fixed ground coordinates. This problem may not be obvious to someone analyzing a two dimensional navigated image unless the satellite elevation angle and cloud height are known. Errors in interpretation may be very significant. Weiss (1978) gives an example for a geostationary satellite: a cloud top at 10 km "appearing" over Anchorage, Alaska was actually located 30 km SSE of Anchorage! Polar-orbiting satellites viewing at large nadir angles "see" high clouds closer to their subpoint along the scan line direction. Any investigator working with satellite images of high clouds must be cognizant of this potential problem and correct for mislocation, especially if the image is to be correlated to ground-based radiometric measurements or other meteorological data. Another example relevant to this study will be given in Chapter 6.

4.3.2 Image Displacement due to Sensor Response Time

Sensor response time is slower for IR detectors than for the visible detectors due to lower signal power received at the longer wavelengths. For example, the GOES-6 VISSR IR channel has a response time of 55 microseconds. The sampling rate of the detector is only 7.6 microseconds, thus 7 samples are converted to count values during the response time (Vonder Haar and Hillger, 1984). The consequence of this time delay is an apparent shift of the pixels in the line scan direction. Therefore, abrupt changes in radiance will be displaced with respect to true ground coordinates. For example, cold cloud boundaries over warm water or coastlines with contrasting water/land temperatures would show distinct displacement relative to geopolitical mapping of the image. Comparing visible with IR images may show ambiguities with respect to known landmarks because of this characteristic.

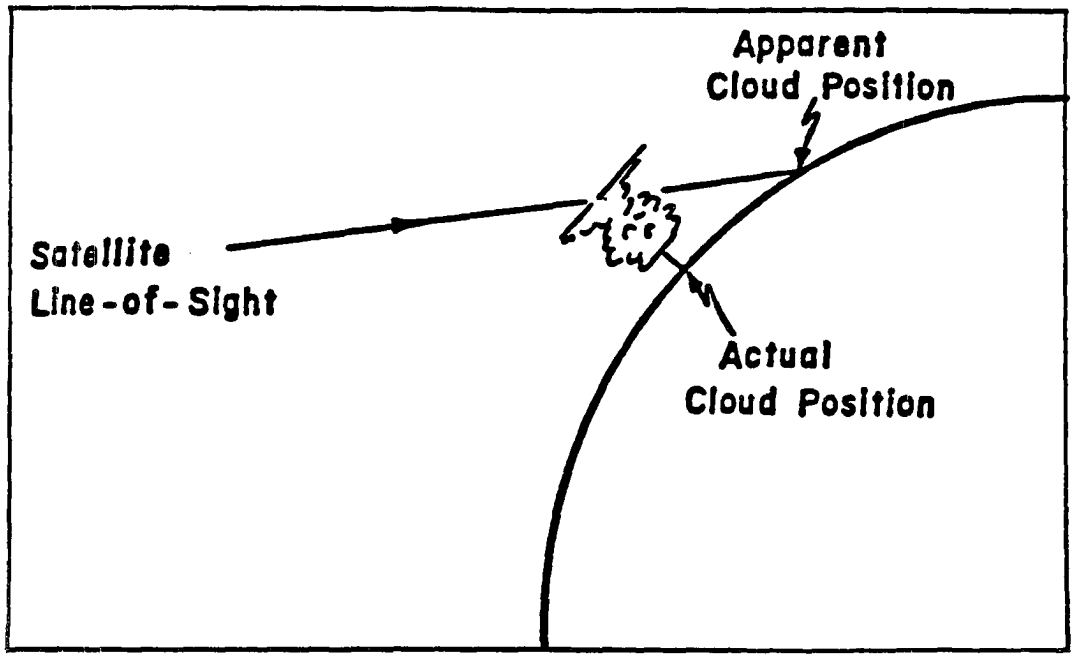

Figure 4.3: Actual vs. apparent cloud position (Adapted from Weiss, 1977).

4.4 Ground-based sensing of the atmosphere

Remote sensing of the atmosphere from ground-based platforms, though limited in areal coverage, greatly enhances our knowledge of the atmosphere's structure and dynamic nature. Radar, for instance, has become an indispensable operational weather forcasting and monitoring tool. For research specifically related to radiative studies of cirrus clouds, a combination of an active lidar (light detection and ranging) device and passive radiometer yields multispectral observations for a narrow field of view through time (e.g. Platt and Dilley, 1981). Because the spatial and temporal resolution of such a lidar-radiometer (LIRAD) system is much finer than that for satellite observations, problems of correlating these data arise. Further discussion of such problems is deferred until Chapter 6.

Typically, the LIRAD station is set up in a monostatic configuration to simultaneously measure backscattered visible light and cloud base radiances along a line as the cloud drifts overhead. The lidar is used to determine the cloud's vertical structure while the radiometer data can be used to determine absorption optical depth. The cloud's temperature profile can be estimated knowing the altitude and vertical extent of a cloud assuming it is the same as the environmental profile measured at a nearby rawinsonde

site or assuming standard climatological conditions exist. By correlating IR radiance measurements with lidar returns and knowing the surface and mean cloud temperatures, Platt (1979) developed a method for determining the visible and infrared properties of high thin clouds. As these ground-based observations will be compared to satellite images and radiative transfer calculations for a particular case analyzed in Chapter 6, further discussion of Platt's method is deferred until then.

Chapter 5

MODEL RESULTS AND SPECTRAL DIFFERENCING

A theoretical method for interpreting multispectral cloud images is developed in this chapter. It follows the work of Stephens (1981) who suggests that the difference between brightness temperatures for near infrared (NIR) and infrared (IR) window wavelengths may be used to determine the presence of thin clouds. In the radiative transfer model, the total upwelling monochromatic intensity $I^{+}_{\Delta\lambda}(TB_{\lambda})$ is related to the Planckian emission function ($B_{\lambda}(TB_{\lambda})$) defined at the brightness temperature TB_{λ}. This intensity is actually calculated for a spectral interval $\Delta\nu$ wide, where ν is the wavenumber defined by $\nu = 1/\lambda$ and λ is the central wavelength of the spectral interval. For simplicity, the brightness temperature is obtained by numerically inverting the following expression

$$I_{\Delta\lambda}(TB_{\lambda}) = \int_{\lambda 1}^{\lambda 1} B_{\lambda}(TB_{\lambda})\, d\lambda = \int_{\nu 2}^{\nu 1} \frac{2hc^2\nu^3 d\nu}{e^{\frac{hc\nu}{kTB_{\nu}}} - 1} \approx \frac{2hc^2\nu^3\Delta\nu}{e^{\frac{hc\nu}{kTB_{\nu}}} - 1} \tag{5.1}$$

where

- c is the speed of light (2.988 x 10^{8} m s^{-1}),
- h is Planck's constant (6.6262 x 10^{-34} J s),
- k is Boltzmann's constant (1.3806 x 10^{-23} J deg^{-1} $molecule^{-1}$), and
- $TB_{\nu} = TB_{\lambda}$

The difference between the NIR and IR window brightness temperatures will be referred to in the following analyses and is denoted by

$$\Delta TB = TB_{\mathrm{NIR}} - TB_{IR} \tag{5.2}$$

Variation of ΔTB as a function of cloud optical depth (τ) is the key factor in identifying thin clouds using the spectral differencing method.

5.1 The Transfer of NIR and IR Radiation Through Thin Clouds

Radiative transfer involving direct solar radiation is highly dependent on the solar zenith angle. TB_{NIR} varies according to the solar radiation incident on the cloud and so the desired ΔTB vs. τ relationship also varies throughout the day, with significant differences noted between day and night. It is therefore important to utilize the correct value of the incident solar flux in the theoretical simulations in order to obtain meaningful results for comparative analysis.

5.1.1 Daytime Case

NIR and IR brightness temperature differences are most significant during the day when the upwelling radiance is enhanced by incident NIR radiation reflected from the cloud top. This reflection is related to the incident solar flux which decreases as the solar zenith angle increases in accordance to the cosine law of irradiance; that is, $F_{o\lambda}(\theta_o) = F_{o\lambda}\cos\theta_o$. For a given solar zenith angle, ΔTB increases with optical depth as a result of the greater reflection as the diffuse limit of the cloud is approached. For large optical thicknesses, the radiometric character of the cloud is more isotropic and the reflection becomes less sensitive to changes in cloud optical thickness. Thus, the difference in brightness temperatures approaches a constant value which is determined by slight differences in thermal emission for the two wavelengths, and dominated by the additional NIR reflection.

5.1.2 Nighttime case

The nighttime case differs from that of day since no solar reflection exists to enhance ΔTB; however, the differences are still positive due to the relative magnitudes of the Planckian emission by the surface and cloud at the respective wavelengths. Relative differences in transmission also augment ΔTB. For thin clouds in the NIR region, emission by the cloud to space is negligible compared to the radiation from the surface; whereas, IR emission from the cloud may comprise the main component of the upwelling radiance for that wavelength. Due to greater attenuation of surface infrared radiation by the cloud, IR transmission is always less than the transmission of near infrared radiation from the

surface. This results from greater absorption $(1 - \tilde{\omega}_o)$ due to the fact that the infrared single scattering albedo is less than that for the near infrared as illustrated in Figure 3.3. As the optical depth increases, ΔTB increases since the transmission of NIR energy from a relatively warm surface plus that emitted by the cloud is greater than the sum of energy emitted by a colder cloud layer plus the transmitted surface IR radiation. When the diffuse limit is reached, the transmitted radiance from the surface becomes negligible and the upward intensity is solely due to thermal emission from the cloud. For these thick clouds, emission is nearly equivalent over the respective spectral intervals selected for use in this study and thus ΔTB approaches zero.

5.1.3 Clear Sky Case

If no clouds exist and the surface albdeo is assumed to be negligible, ΔTB approaches zero for both day and night situations. This is the case since the upwelling radiance is primarily due to Planckian blackbody emission from the surface and this emission is nearly equivalent over the respective spectral intervals. However, due to differential absorption/emission by atmospheric water vapor at these wavelengths, there exists a positive difference of up to about $1°C$ for humid atmospheres (Stephens, 1981).

5.1.4 Diffuse Surface Reflection

The variability of spectral albedo as a function of wavelength for some natural surfaces is indicated in Figure 5.1. These data show typical dependences of surface reflection with respect to wavelength, but departures from these curves can be expected for different objects and incident angles (McClatchey et al., 1971). It is notable in Figure 5.1 that the albedo for water is less than about 1.5% for both of the window wavelengths required to estimate optical depth using the spectral differencing method. Since the satellite images analyzed in this study (Chapter 6) were collected mainly over ocean surfaces, the reflected contribution to the total upwelling radiation at these wavelengths is assumed to be negligible compared to the other components already described. Therefore, a further simplification of the radiative transfer model was made by assuming zero surface

reflectance, thus eliminating the need to include surface reflection when initializing the doubling routine.

As a further note, the effect of surface reflection from surfaces other than water may also be ignored based on the fact that the respective albedos at these wavelengths are nearly equivalent (see Figure 5.1). Therefore, small contributions due to reflection tend to cancel when differenced. At any rate, for the cases analyzed below, errors introduced due to the neglect of surface reflection are certainly insignificant compared to errors caused by other simplifying assumptions already discussed in Chapters 2 and 3.

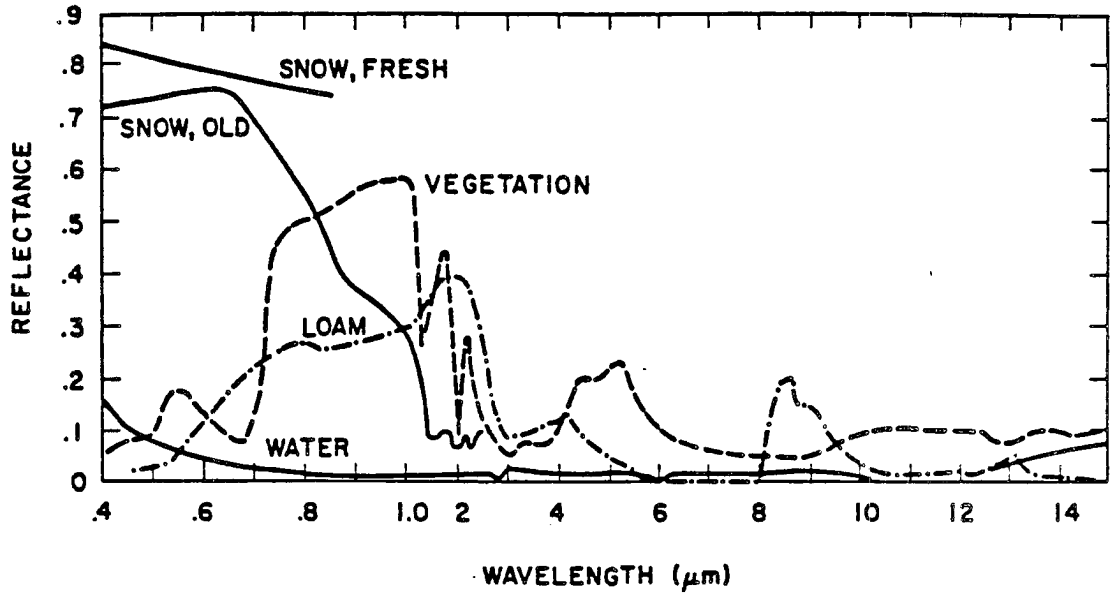

Figure 5.1: Typical reflection (spectral albedo) for natural surfaces (from McClatchey et al., 1971).

Figures 5.2 (a) and (b) graphically illustrate the transfer of radiation through a thin cloud layer for each of the window wavelengths and for day and night conditions described above. Sample plots of ΔTB versus optical depth for both day and night are presented in Figure 5.3. These curves were produced by using the optical properties derived for a model cloud (MP-3, Table 3.2) in the radiative transfer model initialized for surface and cloud temperatures as noted in the figure.

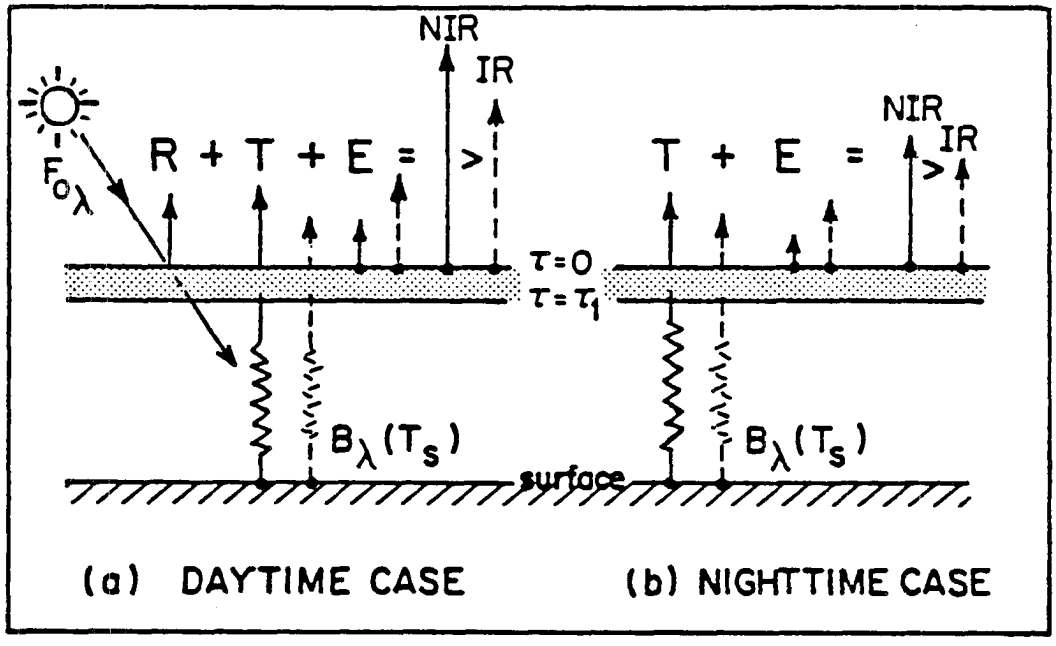

Figure 5.2: (a) daytime and (b) nighttime schematics representing the transfer of NIR (solid vectors) and IR (dashed vectors) radiation by thin cirrus clouds. The length of the vectors are proportional to the reflected (R), transmitted (T) and emitted (E) radiances (exaggerated for illustrative purposes).

The results presented in Figure 5.3 suggest that optically thin clouds may be detected using spectral differencing for either day or night images. The example shown in this figure is perhaps typical of what might be expected for thin cirrus of varying opacity over the ocean for which surface reflection can be ignored.

Practical use of this technique requires that theoretical plots of ΔTB vs. τ be produced for specific viewing geometries to enable comparison with actual satellite image pairs. In addition, sensitivity to microphysical changes in the cloud must be taken into account. For this purpose, a family of ΔTB-curves representing the various microphysical models was generated by initializing the radiative transfer model for the boundary conditions and viewing geometries defined by the relative sun-satellite-IGFOV positions for the times satellite observations were made. Before presenting an example, the importance of solving the transfer problem for a specific satellite viewing angle is discussed. Azimuthal and zenith (or quadrature) dependencies are treated separately.

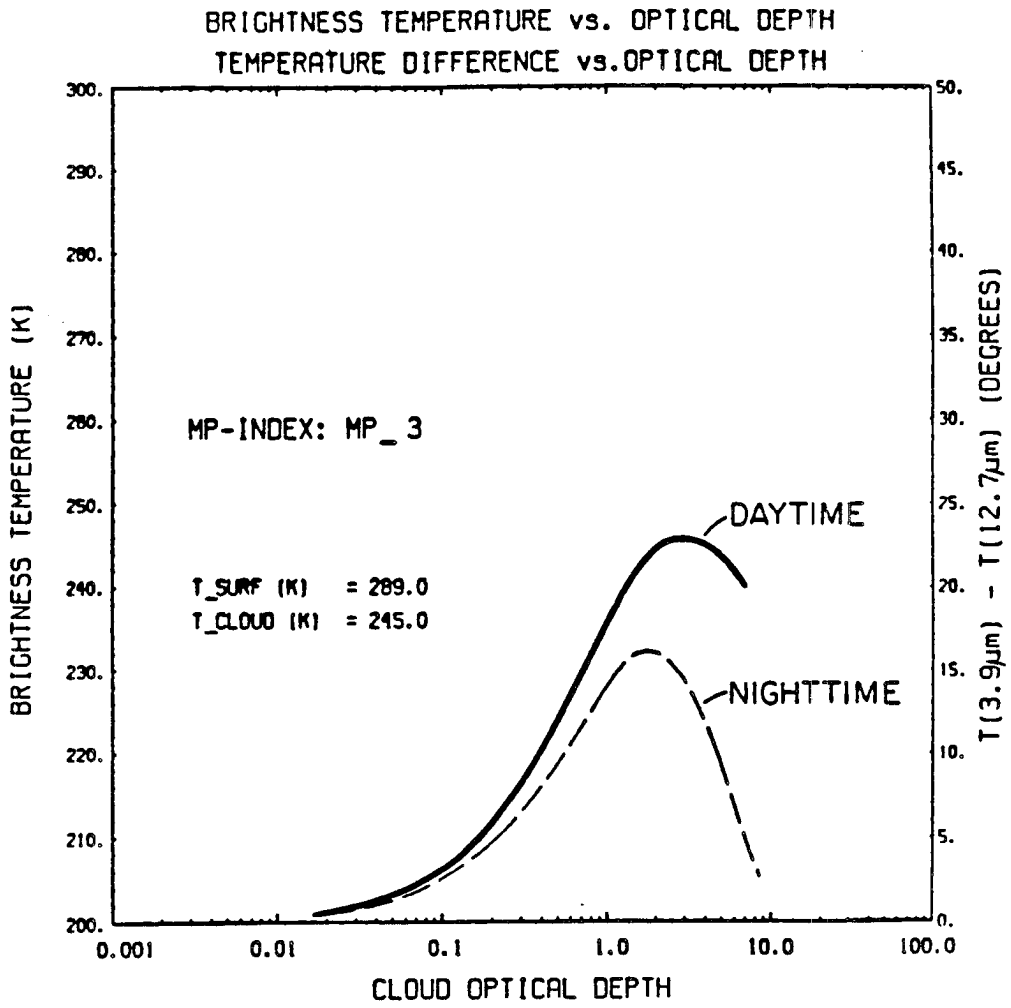

Figure 5.3: An example of the brightness temperature differences as a function of optical depth for daytime and nighttime using GOES-VAS window channels.

5.2 The Upwelling Radiation Field

5.2.1 Azimuthal Dependence

In Chapter 2 it was stated that the assumption of azimuthal independence of the radiation field was reasonable for a wide range of satellite viewing angles. To illustrate this point, the radiative transfer model was run for several test cases employing equation (2.13). Recall that this form of the radiative transfer equation incorporates the azimuthal dependence as N+1 Fourier coefficients; the intensity field being determined by the sum of the m-amplitudes ($I^m(\tau;\mu)$ for $m = 0,\ldots,N$). By using Gaussian quadrature and implementing the principles of invariance and the Interaction Principle for local and global

reflection and transmission matrices, (2.13) was reduced to a linear system of equations (2.17). The doubling method was then used to simulate the radiation field for discrete quadrature angles.

The question that arises is: how many terms are required in the Fourier series expansion to determine the radiation field accurately? van de Hulst (1980) presented empirical results which suggest that if the incident solar zenith angle (θ_o) or reflection angle (θ) is well removed from the grazing direction, the number of required terms is small. King (1983) confirmed these results by comparing individual terms of the Fourier expansion to find the number of terms required to achieve an accuracy of 0.1% using both the Mie phase function and the Henyey-Greenstein approximation. He found that for both functions, more terms were required for near grazing angles of the incident or reflected beam than for all other directions. Based on these studies, the radiative transfer model was run for N = 8 and N = 12 respectively and the sums were inspected for convergence at each selected azimuth angle. The sums differed in the worst cases by about 0.8% for very low sun angles in the extreme backward and forward scattering directions relative to the sun. Generally, differences were less than 0.1% indicating that even for N = 8, most of the field can be accurately represented. For the following analysis, N = 12 was used to represent the radiation field "exactly." Comparisons were then made between the exact and azimuthally independent case ($m = 0$) to determine relative errors over a full range of quadrature and azimuth angles, assuming azimuthal independence.

Intensities were computed for each quadrature/azimuthal angle pair ((μ_j, ϕ_k), $j = 1,\ldots,16$ and $k = 1,\ldots,19$) for the 16 quadrature angles listed in Table 2.1 and 10° azimuth increments from 0° to 180°. The sun's azimuth (ϕ_o) was set to 0 as a convenient reference point. Note that the radiation field is symmetric about $\phi = 0°$, $\phi = 180°$ since the Fourier expansion is in terms of $\cos\phi$ which is an even function. Figure 5.4 gives an example of comparative results for the exact and azimuthally averaged solutions at a specific quadrature angle ($\theta = 48.47°$). The calculations were derived with the following parameter values: $\theta_o = 26°$, incident NIR irradiance of $F_{o\lambda} = 3.95$ W m^{-2} coinciding with the bandwidth of the 3.9μm VAS channel (interpolated from the Table C.1, Iqbal, 1983),

surface and cloud temperatures of 288 K and 243 K respectively, $r \approx 0.3$ and radiative properties for MP-4 from Table 3.2. Intensities were converted to brightness temperatures to be consistent with subsequent analysis.

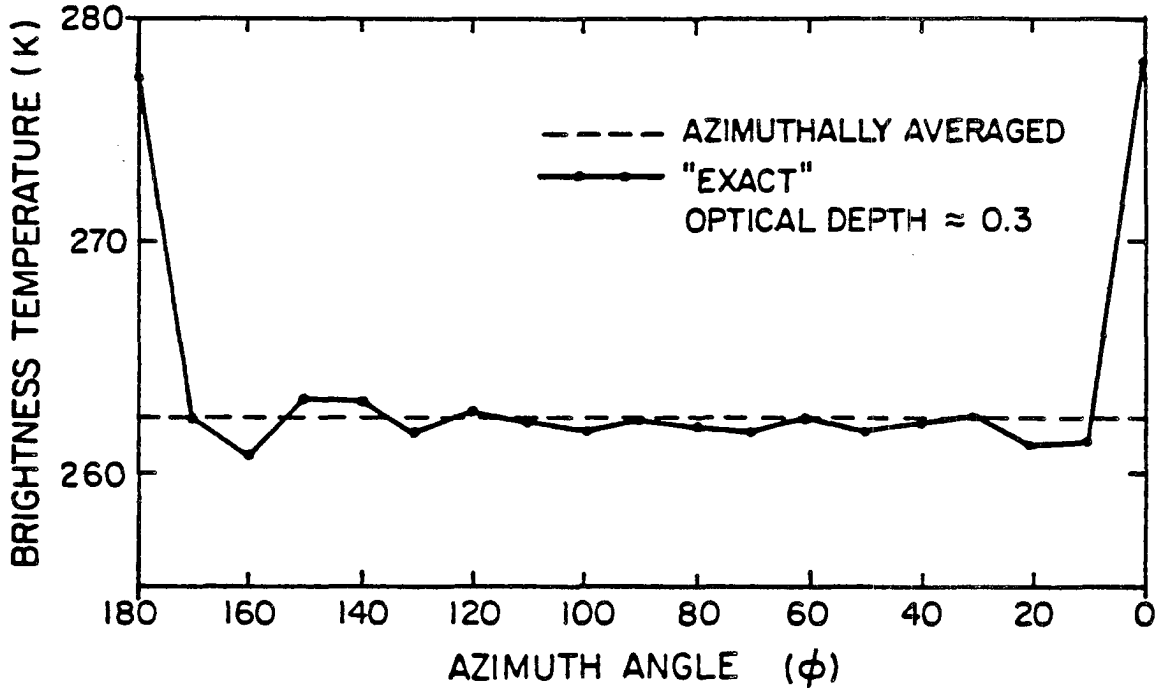

Figure 5.4: Comparison of the exact (solid curve) and azimuthal independent solutions (dashed curve) to the radiative transfer equation at one quadrature angle.

The relative errors determined for this particular example for the azimuthally averaged solution are less than ±0.4% for all angles except near the forward and backward directions where differences are quite significant. The example shown in Figure 5.4 applies only to one angle θ. A broader representation of these errors is presented in Figure 5.5 in the form of a sky map. Azimuth varies around the circumference of the diagram and θ varies along the radial direction. The contours represent the %-difference in brightness temperature between the exact solution and the azimuthal independent case and is defined as

$$\text{Error}\,(\%) = \frac{|\,\text{TB}_{N=12} - \text{TB}_{m=0}\,|}{\text{TB}_{N=12}} \times 100 \tag{5.3}$$

Shown in Figure 5.5 are the sun's position which is set on the zero azimuth line at a zenith angle of about 80° (an elevation angle of 10°). The position of the satellite (which

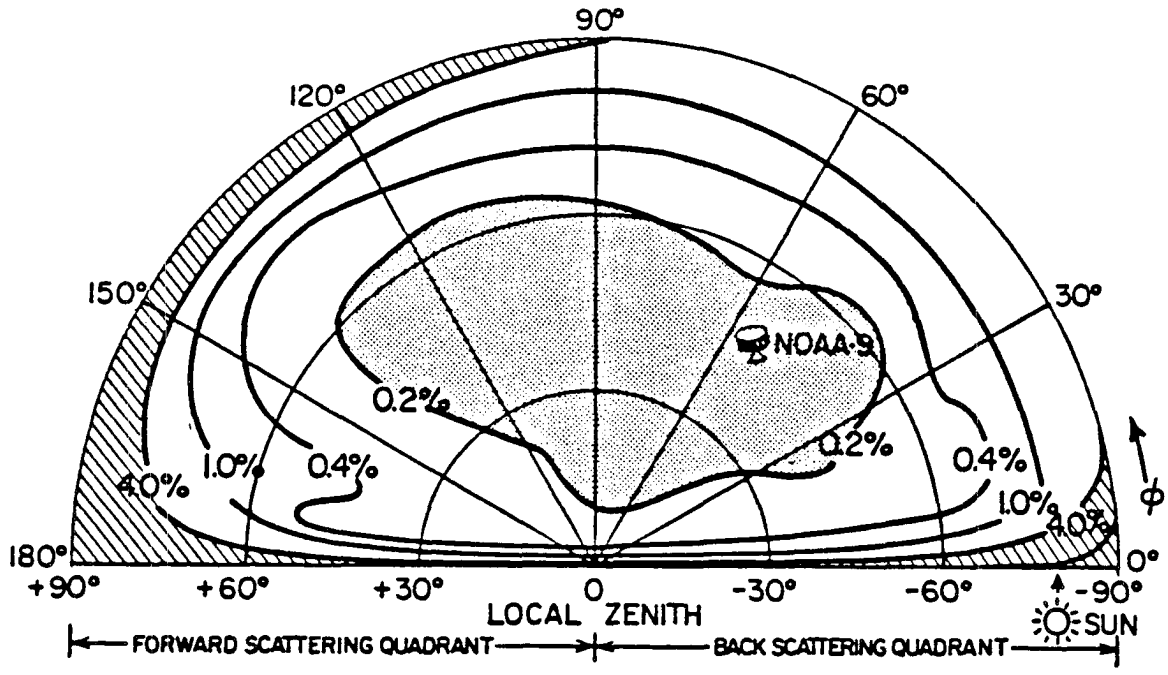

Figure 5.5: Sky plot of relative (%) errors in brightness temperatures between the exact solution and the azimuthally averaged solution for a discretized radiation field explained in the text.

is relevant to a case study described below) is also indicated and is at an azimuth of about 53° relative to the sun and a zenith angle of 48°. Distinct regions exist for which the azimuthal independent assumption is very acceptable (stippled) and poor (hatched). Within the stippled area, relative errors in brightness temperature are less than 0.2% which are less than approximately $\pm 0.5°C$ for temperatures around 240 K. Therefore, radiative transfer calculations using the azimuthal independent form of the equation simulate well the radiances measured by a satellite which has coordinates that fall anywhere within this region. Conversely, large errors would be expected for satellite observations with coordinates that fall within the hatched area of this diagram. Large errors are generally found along the axis of the sun in both the forward and backward scattering directions at most zenith angles and near the opposite horizon over a broad range of azimuth angles.

Several other cases (not included here) were analyzed similarly to determine whether or not the assumption of azimuthal independence is justified. Test cases were inspected for different sun angles, optical depths and MP-indices. Though the pattern of error changed as these factors were varied, broad regions with small errors were found to exist in most

cases; especially for those angles commonly associated with satellite observations. Thus, the azimuthally averaged form of the radiative transfer equation was adopted for this work.

5.2.2 Variation of Brightness Temperature with Quadrature angle

Analyses of sky plots (above) gave convincing evidence to support the assumption of azimuthal independence for a broad region of space. In contrast, the radiation field is generally more sensitive to changes in zenith angle (quadrature direction). To make reasonable comparisons between theoretical calculations and satellite imagery, the radiative transfer model must yield results for the quadrature angle most closely matching the satellite's zenith angle. The importance of this is illustrated in Figures 5.6 (a) and (b). These figures show plots of brightness temperature as a function of quadrature angle for a thin and a moderately thick cirrus cloud. These angles are denoted by the upward pointing arrows along the bottom of each plot. In this example, the sun elevation angle is low (10°) and the MP-index is representative of a size distribution with an effective radius of 16 microns (MP-3, Table 3.3).

A thin cloud (Figure 5.6 (a)) produces nearly constant brightness temperatures for both channels over a range of quadrature angles from 0° to about 48°, however, as the angle increases toward the horizon, the temperatures diverge radically in opposite directions. The increase of the $3.7\mu m$ temperature is a result of reflection as the response angle approaches the grazing direction (limb brightening). The $10.8\mu m$ brightness temperature decreases markedly due to limb darkening. Limb darkening occurs when the slant path through the cloud is sufficiently long to attenuate most of the surface energy incident at the cloud base; brightness temperature then approaches the Planckian blackbody temperature of the cloud.

For moderately thick clouds (Figure 5.6 (b)), limb brightening and darkening are enhanced due to greater NIR reflection and IR attenuation respectively. Brightness temperature varies more smoothly with θ for these thicker clouds than for the thin cloud case shown in Figure 5.6 (a). The infrared brightness temperature tends to be more isotropic

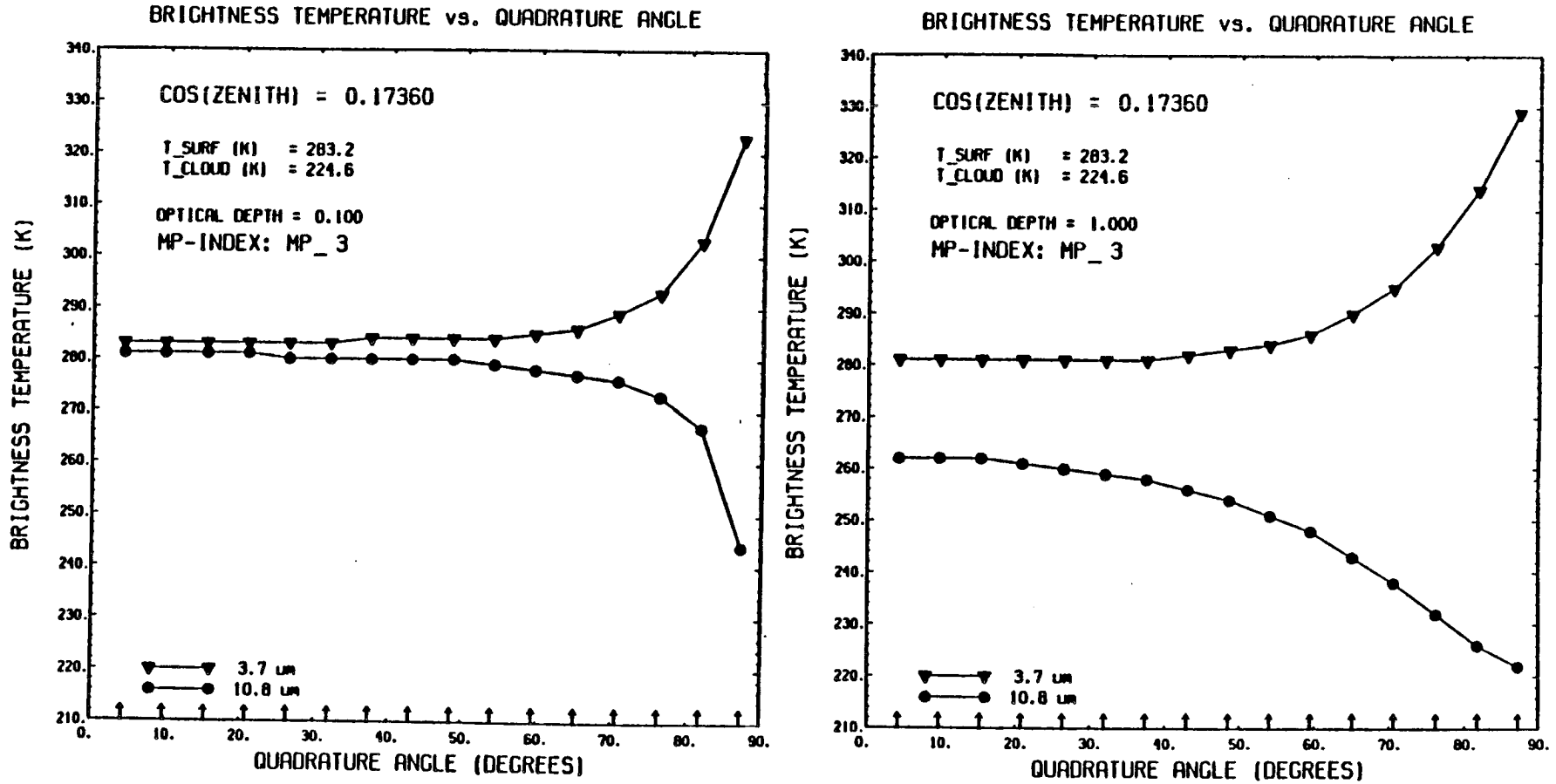

Figure 5.6: Theoretical calculations of ΔTB vs. quadrature angle for typically (a) thin and (b) thick cirrus clouds. Up-arrows represent the quadrature angles listed in Table 2.1.

as the optical thickness of the cloud increases. In either case, ΔTB is not constant over a very wide range of emergent angles. Though these trends change depending on the solar zenith angle, cases involving thin clouds generally show significant variation of TB_λ with emergent angle θ. This behavior must be accounted for if meaningful comparisons between theoretical calculations and observations are to be made.

5.3 Brightness Temperature Differences for Varying Microphysics

The complex nature of the microphysical properties of cirrus clouds greatly complicates the study of radiative transfer through these clouds. How these differences affect the identification of optically thin cirrus utilizing the method of spectral differencing is the subject of this section. The cloud models constructed in Chapter 3 are used to determine the effect that varying microphysical properties have on the behavior of brightness temperature differences as a function of optical depths. To accomplish this, radiative transfer calculations were carried out with appropriate boundary conditions and run successively for each of the MP-indices. Calculations of spectral brightness temperatures and differences in brightness temperature were obtained over a wide range of optical depths and composite plots of ΔTB vs. τ were produced in each case. Eight solutions for $TB_\lambda(\tau)$ were fit using a cubic spline from which 40 new points were interpolated and fit with a curve utilizing an NCAR plot routine. Sample results are presented in Figure 5.7. This family of curves relates to a specific case which will be analyzed in the following chapter. The near infrared and infrared channels of the NOAA-9 AVHRR were used in this particular study and the quadrature angle was selected to match closely the satellite viewing angle at the time it passed over a station where simultaneous ground-based measurements were made.

The general features of the curves in Figure 5.7 persist over the entire range of microphysics selected for this study. An obvious trend of each of these curves is the monotonic increase of ΔTB as optical depth increases and their asymptotic approach to constant values as the diffuse limit of the cloud is reached. Another feature is that of decreasing ΔTB as the MP-index increases. This occurs because the single scattering albedo at $3.7\mu m$

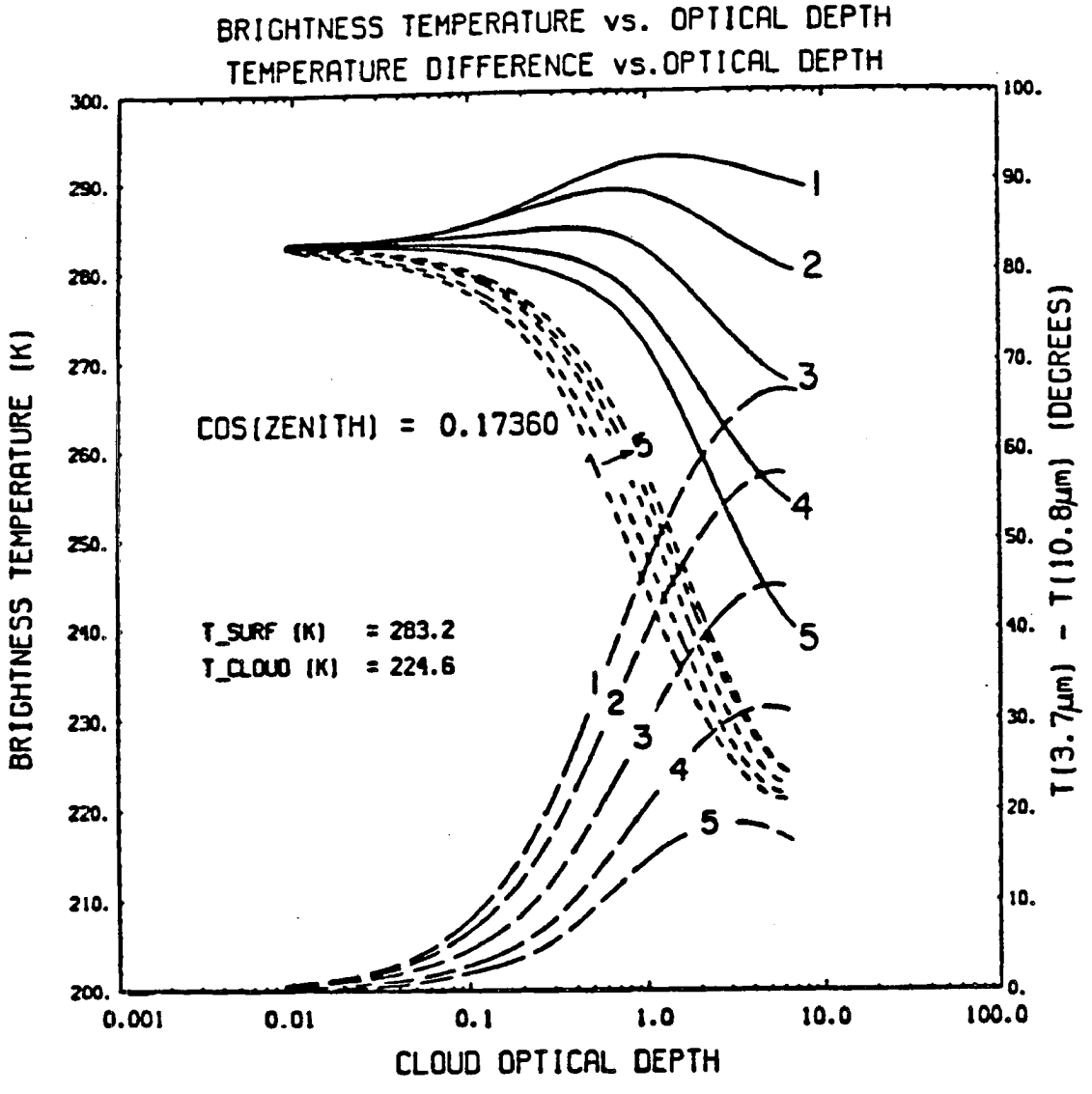

Figure 5.7: Composite of plots relating ΔTB to τ for model cirrus clouds. MP-indices are from Table 3.3. Solid curves are those for the $3.7\mu m$ NIR channel and dashed for the $10.8\mu m$ IR channel and relate to the lefthand scale. Long dashed lines are for ΔTB (right scale).

decreases with increasing MP-index (Figure 3.3) resulting in an increase in absorption at this wavelength; thus, the transfer of $3.7\mu m$ radiation becomes similar to the transfer of $10.8\mu m$ radiation which is dominated by emission/absorption. Therefore, ΔTB diminishes as the MP-index (or particle size) increases due to the convergence of the spectral properties of the cloud layer.

Other features of these curves are also explained by the radiative processes distinctive to each of these wavelengths. All curves asymtotically approach the surface temperature as $\tau \rightarrow 0$ since any effects of atmospheric absorption below the cloud layer are neglected. As the cloud approaches its diffuse limit, TB_{IR} converges toward the cloud blackbody temperature. For medium thick clouds, IR brightness temperatures are warmer for larger MP-indices. This is due to a combination of increasing asymmetry factor and single scattering albedo with increasing MP-index (see Figures 3.2 and 3.3). Absorption is reduced while forward scattering is increased resulting in greater relative transmission of surface radiation, producing warmer temperatures.

The near infrared curves show more complicated dependences on MP-index. Depending on the cloud model, temperature either increases and then decreases with increasing optical depth for small particles, or monotonically decreases with optical depth for the larger particles. Reasons for these trends are again understood by the differences in the radiative properties for the various cloud models. Moderately thick cirrus clouds composed of many small particles (solid curves 1 and 2 in Figure 5.7) reflect greater amounts of incoming NIR radiation by virtue of their large single scattering albedos and their larger backscattering intensities (smaller asymmetry factor). This added contribution to the upwelling intensity results in greater values of ΔTB. As the cloud becomes thicker, transmitted surface radiation diminishes due to attenuation within the cloud, thus slightly decreasing TB_{NIR}.

Clouds composed of fewer but larger ice particles (solid curves 4 and 5 in Figure 5.7) have their own peculiarities. For a given optical depth, these clouds appear colder than the clouds described above because less incident radiation is reflected. Anisotropic scattering in the forward direction (larger asymmetry factor) combined with a decreased

single scattering albedo, results in greater absorption which reduces reflection. In addition, transmission of upwelling radiation from the surface is reduced as the cloud becomes thicker, contributing to the monotonic decline in temperature as optical depth increases.

It must be noted that the preceeding discussion pertains to a unique family of curves determined by specific boundary conditions, sun geometry, cloud geometry and cloud model type. Details will vary from case to case, but the trends and arguments presented will be valid for a broad range of situations and represent a sound theoretical basis for analyzing image pairs. The usefulness of such a composite is further demonstrated in the next chapter.

Chapter 6

OBSERVATIONS AND ANALYSIS - CASE STUDIES

Previous discussions in this study have focused on the theoretical aspects of radiative transfer through cirrus clouds characterized by varying microphysical properties. The results presented in Figure 5.7 suggest that it may be possible to identify thin clouds by exploiting the relationship between brightness temperature differences and optical depth. These results were generated from the radiative transfer model initialized for a prescribed set of boundary conditions and a viewing geometry that relate to an actual observational experiment. The experimental set-up, data and comparative results are examined in the next section.

6.1 7/21/86 Aspendale Cirrus Experiment - Aspendale, Australia

The case analyzed below is one of several cirrus cloud experiments conducted at Aspendale, Australia during the winter of 1986. These experiments were conducted by the Commonwealth Scientific and Industrial Research Organization (CSIRO) and provide data which are particularly suitable for investigating the radiative properties of cirrus clouds.

6.1.1 Set-up of the Aspendale LIRAD Experiment, 7/21/86

The data for this study consists primarily of multispectral satellite imagery and ground-based lidar and infrared radiometric (LIRAD) data (e.g., Platt, Part I, 1979) which were collected as a cirrus cloud deck drifted over Aspendale on July 21, 1986. In addition, radiosonde data from a nearby site provided profiles of temperature, moisture, wind speed and direction at times before and after the radiometric observations were made. The aerological data was used in conjunction with the lidar data to estimate the ambient

cloud temperature and cloud motion. The location of the LIRAD site, the radiosonde station, the ascending track and scanline orientation of NOAA-9 and the extapolated motion of the cloud are indicated in Figure 6.1.

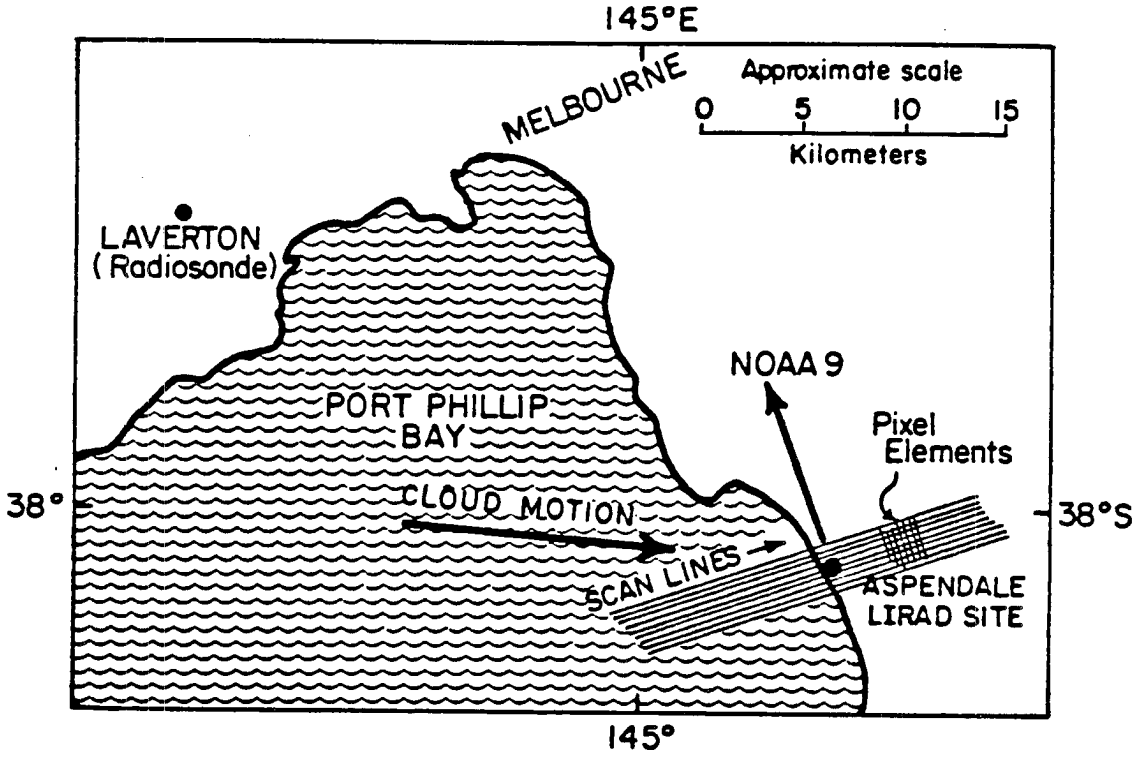

Figure 6.1: Map of the set-up for Aspendale Cirrus Experiment showing the relative scanline orientation of NOAA-9's AVHRR instrument in its ascending orbit on 7/21/86. The radiosonde station and extrapolated cloud motion are also indicated.

An enhanced visible image of a portion of southeastern Australia is pictured in Figure 6.2. This image was produced from full resolution (1 x 1 km) AVHRR data. No correction for pixel elongation along the scanline was made resulting in foreshortening of the image in the west-east (left-right) direction. Port Phillip Bay is centered in this picture, a portion of which is shown in Figure 6.1 in proper scale. Aspendale is located approximately a third of the way down the east shore of the bay.

6.1.2 Observational Data Collected

NOAA-9's AVHRR collected MSI data as it passed over Aspendale at an elevation angle of about 42° and an azimuth angle of 253° (relative to north). It was in an ascending

Figure 6.2: Visible image of a portion of southeastern Australia from NOAA-9 showing the cirrus cloud deck described in the text, 7/21/86, 6:10 GMT.(Original photo by CSIRO).

orbit which produced scanlines oriented 73° from north. The sun's elevation was about 10° above the western horizon at an azimuth of 306.2°. Table 4.1 lists the AVHRR channels including the $3.7\mu m$ NIR and $10.8\mu m$ IR window channels which were used to compute the brightness temperature differences from equation (5.2).

The vertically pointing LIRAD system measured the attenuated backscattered intensity using a "ruby" lidar operated at a visible wavelength of $0.694\mu m$, while downwelling infrared radiation was simultaneously sensed by the radiometer tuned to match channel 4 of the AVHRR, (spectral center $\approx 10.8\mu m$). From lidar ranging measurements, fairly accurate cloud base and cloud top heights were determined. Then, by correlating the mean cloud height with the available aerological data, a mean cloud temperature ($\bar{T}_c$) and the motion of the cloud were deduced.

A sample of the lidar returns which were produced at 15 second intervals during the experiment is presented in Figure 6.3. The radiosonde profiles are shown in Figure 6.4 with the estimated mean height and vertical extent of the cloud indicated. The direction of motion was taken as that at the cloud top level denoted on the figure by the bold-faced wind vector. Cloud velocity was estimated at 17 m s^{-1} from the WNW (276°) at an altitude of 9.9 km.

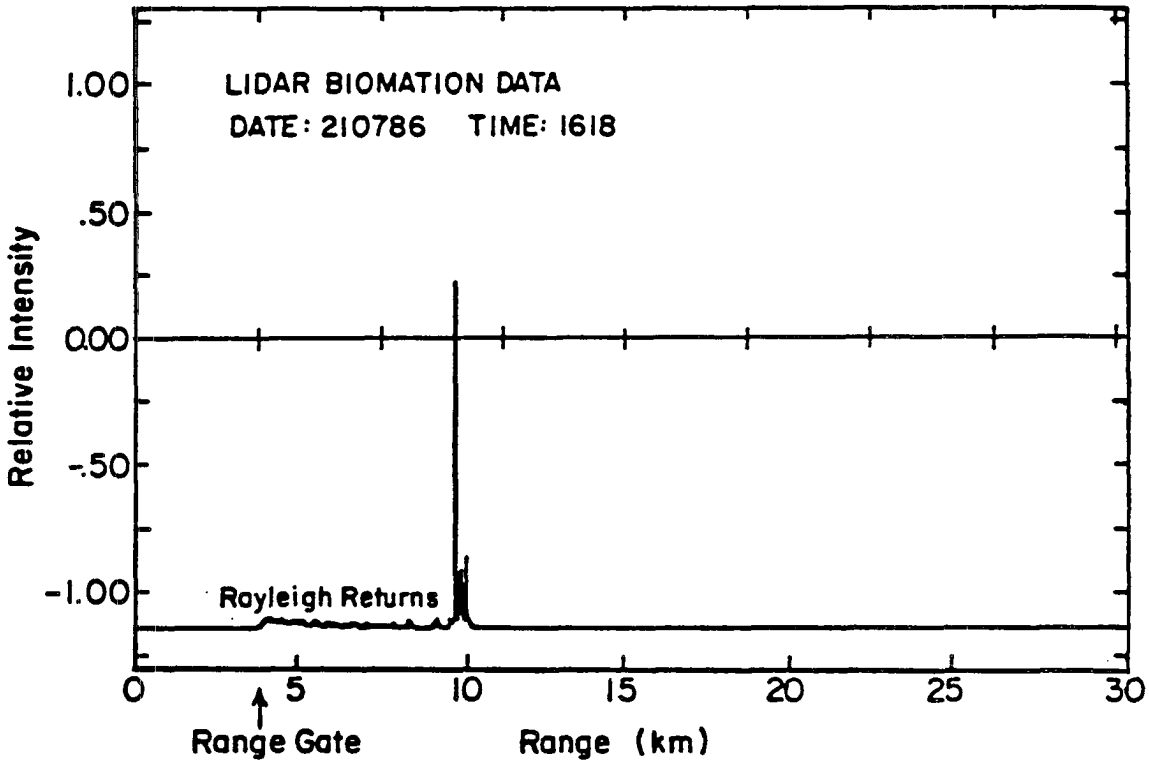

Figure 6.3: Sample lidar return from the 7/21/86 Aspendale Cirrus Experiment (adapted from lidar biomation data provided by Platt, 1987). Such data was correlated with the aerological data shown in the following figure.

The radiometer recorded cloud base radiances also at 15 second intervals as the cloud drifted overhead. From these data a time series of infrared emissivities (ϵ_a) was derived. Utilizing an appropriate conversion scale, these emissivities were then related to equivalent brightness temperatures enabling direct comparison between ground-based measurements and AVHRR pixel brightness temperatures along a coincident transit line. Details of this procedure are given below.

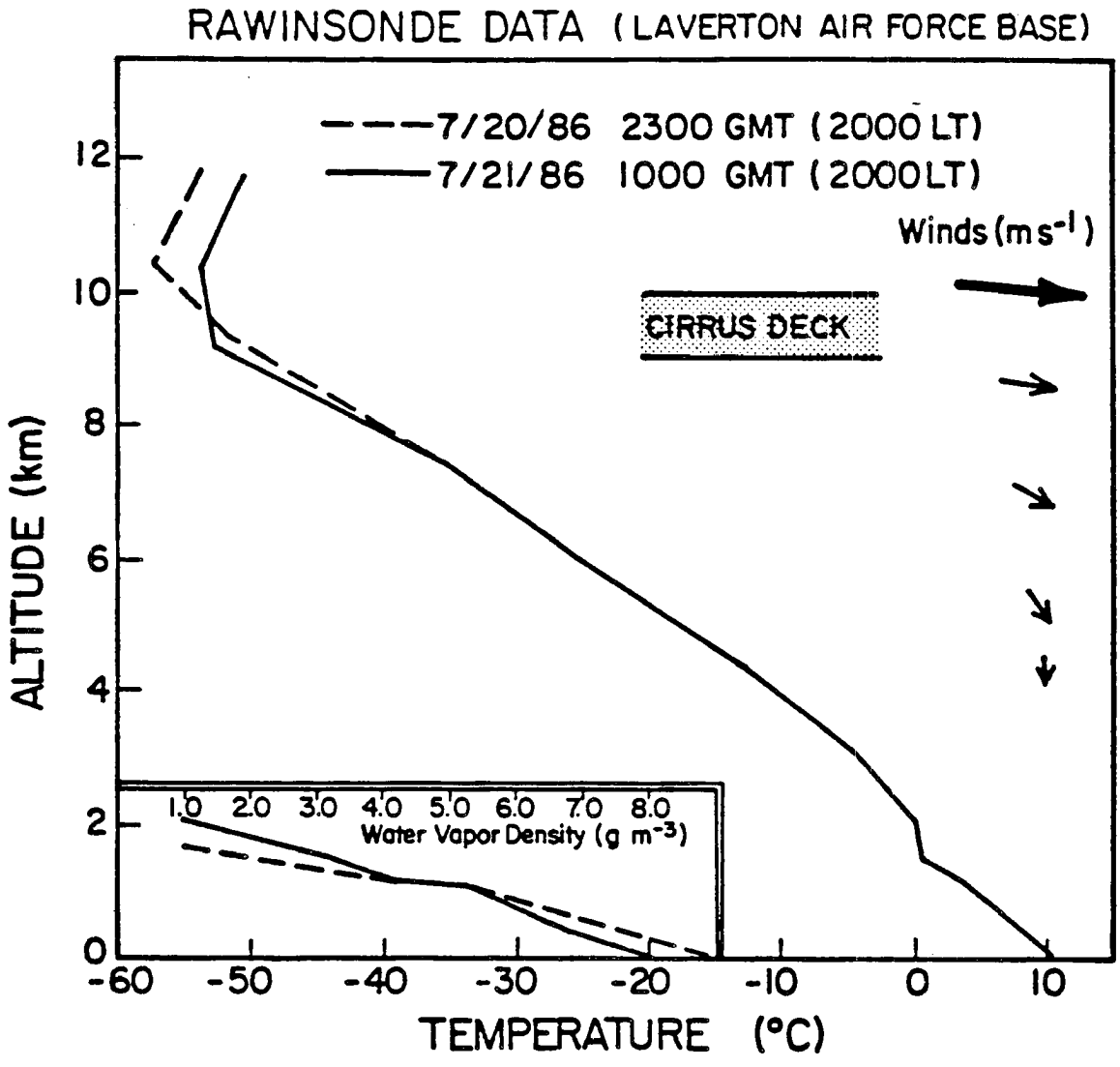

Figure 6.4: Laverton radiosonde profiles used to deduce cloud temperature and motion for the cirrus deck that drifted over Aspendale on 7/21/86. Wind speed and direction are indicated by scaled vectors. Water vapor density profiles were used to derive the clear sky radiance described in Section 6.1.3.

Figure 6.5 shows a perspective of the geometric configuration for the 7/21/86 Aspendale experiment veiwed in the plane of the 38° south latitude circle. The angular position of the sun and satellite are schematically illustrated relative to the LIRAD site and cirrus cloud position. Note that the field of view of NOAA-9's AVHRR is not the same as that of the vertically pointing LIRAD FOV. (Also, see Section 4.3.1 for a discussion of mislocation of cloud tops).

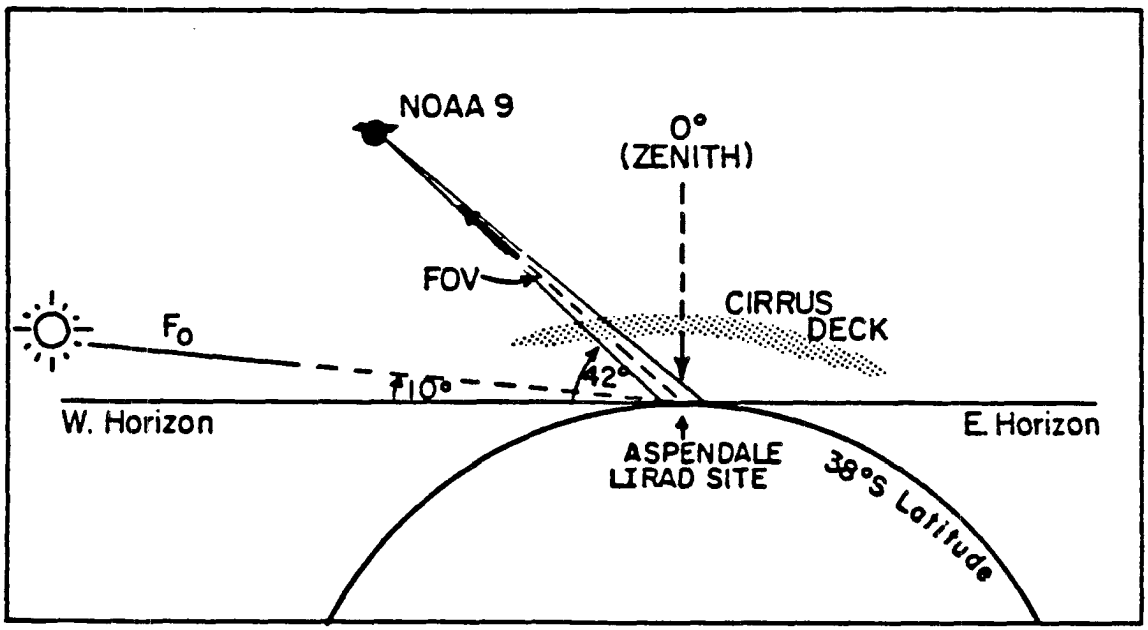

Figure 6.5: Cross- sectional view in the plane of the 38°S latitude circle for the 7/21/86 Aspendale experiment highlighting the geometric configuration of the sun-satellite-LIRAD-cloud system analyzed in the text (NOT TO SCALE).

The task of selecting coincident satellite data for comparison with ground- based data was complicated by the geometry illustrated in Figure 6.5 and the non-synchronous timing of the respective observations. The basic problem resulted from the fact that the satellite scanned a sector of the cloud deck in a matter of a few seconds, while the LIRAD required more than 40 minutes to make measurements along a line across the equivalent sector as the cloud drifted within it's FOV.

The actual cloud position was upwind from its apparent position relative to ground coordinates at the time of the overpass, as is evident in Figure 6.5. Therefore, a significant period of time may have lapsed from when the AVHRR sensed a given pixel and the

time it took that pixel to drift over the LIRAD site. Realistically, the cloud would not remain static in time. Dynamical effects may have changed the physical or microphysical characteristics of the cloud layer or perhaps its motion, but there is no feasible way to account for such effects. Therefore, to simplify the problem, it was assumed that the cloud remained plane-parallel and horizontally homogeneous throughout the duration of the experiment and that the layer drifted with a constant speed and direction over Aspendale as indicated in Figures 6.1 and 6.4. Time was referenced "before" or "after" the overpass time of NOAA-9 given as 06:14:47 GMT (or about 16:15 local time).

Even measurements of the satellite and LIRAD which may have been made simultaneously are not coincident in space due to the monostatic configuration of the LIRAD system relative to the nadir viewing angle of the satellite and the great height of the cirrus cloud. Therefore, a transformation in time and space was required to align the respective data points before any correlation was attempted. A further complication in selecting coincident lines of data resulted from the foreshortening of pixels at the large nadir angles (greater than 45°) at which NOAA-9 viewed the region around Aspendale. (See also Figure 4.2). The Aspendale sector was remapped to correct for this foreshortening. An average-sized pixel was calculated for a nadir angle pointing toward Aspendale resulting in a resolution of about 1.0 km in the N-S direction by 1.9 km along the scanline direction.

Another factor related to geometry required correction of the satellite brightness temperatures before final comparison with LIRAD results could be made. The ground-based radiometer measured downwelling radiances from the cloud of optical depth τ. The satellite AVHRR, on the other hand, measured upwelling radiance from the cloud top through an optical path which was greater than the true cloud optical depth by a factor of $1/\cos\theta$, where θ was the zenith angle of the satellite. For a clear sky, the derived brightness temperatures for both the AVHRR and LIRAD radiometers are expected to be approximately equal to the surface temperature (T_s) effectively fixing a "warm" limit for TB_{IR} (i.e., when the cloud emissivity is zero). However, the slant optical path length is always greater than the optical depth for any finite cloud depth; thus, the satellite observed brightness temperatures tend toward the colder blackbody temperature of the

cloud. Consequently, as the optical depth varies over distance (or time), excursions of satellite measured brightness temperatures vary more than those of the LIRAD equivalent brightness temperatures. Therefore, it was necessary to convert the slant path length to actual optical depth in order to achieve the best correlation possible between the respective calculated cloud emissivities.

Despite the physical complexity of the experiment described above, and the simplifying assumptions required to make the analysis feasible, this data set afforded a rather unique opportunity to explore the radiative properties of cirrus clouds. Encouraging results were obtained.

6.1.3 Analysis and Results.

The goal of this study was to estimate the total cloud optical depth of the cirrus cloud which drifted over Aspendale utilizing the spectral differencing method in conjunction with theoretical radiative transfer calculations. By exploiting the relationship between brightness temperature differences and optical depth, and knowing the dependence of ΔTB vs. τ on cloud microphysics (illustrated in Figure 5.7), the radiative properties of this cloud were also inferred.

Emittance/Brightness Temperature Scale

A common scale relating infrared brightness temperatures (TB_{IR}) to absorption emissivities (ϵ_a) was first determined in order to make meaningful comparisons of the satellite and ground-based data. This scale was approximated as follows.

The surface and cloud blackbody infrared radiances were computed by numerically integrating the Planck function over the IR channel bandwidth (ΔIR). These values are denoted by $B_{\Delta IR}(T_s)$ and $B_{\Delta IR}(\bar{T}_c)$ respectively. The total upwelling IR radiance measured by the satellite was then approximated by

$$I^{\uparrow}_{\Delta IR}(TB_{IR}) = T r_{cld} B_{\Delta IR}(T_s) + \epsilon_a B_{\Delta IR}\left(\bar{T}_c\right) \tag{6.1}$$

where

- T_s and $\bar{T}_c$ are the surface and mean cloud temperatures respectively, and

- Tr_{cld} is the transmissivity of the cloud, $(1 - \epsilon_a)$

By knowing the surface and cloud temperatures, values of upwelling intensity as a function of ϵ_a were obtained from (6.1). Finally, by inverting the Planck function for $I^{\uparrow}_{\Delta IR}(TB_{IR})$, infrared brightness temperatures were calculated as a function ϵ_a. The results are presented in Figure 6.6. The curve in this figure was produced by fitting a quadratic polynomial to the five calculated points (ϵ_a, TB_{IR}) indicated. This quadratic relationship was used as an approximate conversion scale for infrared brightness temperatures and absorption emissivities in the subsequent analysis.

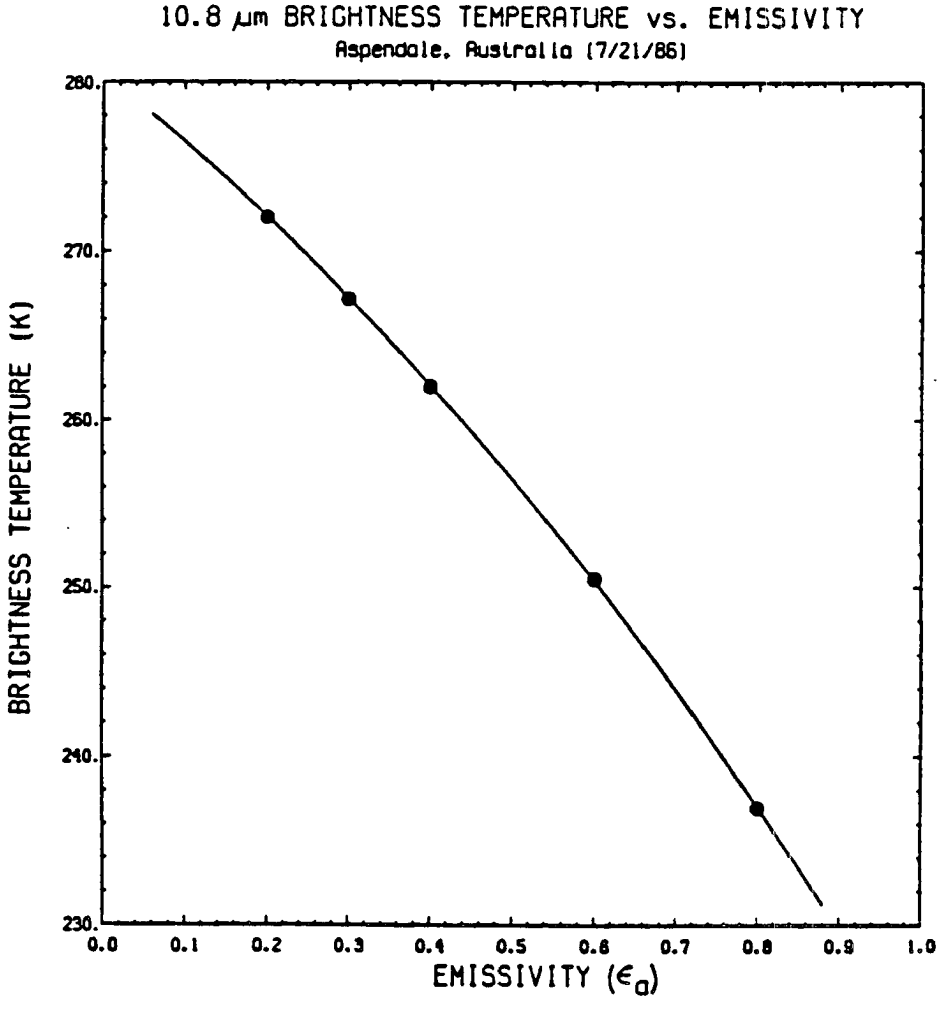

Figure 6.6: Plot of infrared brightness temperature (TB_{IR}) versus cloud absorption emissivity (ϵ_a) used to determine a common scale for comparing satellite and LIRAD derived radiance parameters.

Calculation of Cloud Emittance from LIRAD Radiance Data.

The LIRAD radiometer measures the sum of the infrared radiation emitted from the cloud base transmitted through the intervening atmosphere plus the contribution from the atmosphere itself. Thus, the LIRAD radiance, denoted by I_{rad}, is approximated as

$$I_{rad} = \epsilon_a B_{\Delta IR}(\bar{T}_c) Tr_{sky} + I_{sky} \tag{6.2}$$

where

- Tr_{sky} is the transmissivity of the sky, and
- I_{sky} is the "sky" radiance.

Therefore, cloud emissivity can be approximated by

$$\epsilon_a = \frac{I_{rad} - I_{sky}}{Tr_{sky} B_{\Delta IR}(\bar{T}_c)} \tag{6.3}$$

and an equivalent brightness temperature can be interpolated from the relationship depicted in Figure 6.6.

ϵ_a can be obtained from (6.3) if the sky radiance and sky transmissivity are known. Since water vapor is the principal absorbing- emitting constituent in the infrared window region, the humidity profiles measured by the Laverton radiosondes (see Figure 6.5) were useful for estimating these quantities. The "water vapor continuum" and its effect on the atmospheric transmittance is discussed in some detail by Paltridge and Platt (1976). Only a general outline of the procedure used to approximate Tr_{sky} and I_{sky} is included here.

Based on the humidity profiles shown in Figure 6.5, it was convenient to divide the lowest 2 km of the atmosphere into two layers (0 - 1 km, and 1 - 2 km) for which mean values of water vapor density ρ_1 and ρ_2 were easily interpolated. A mean density weighted path length for each of these layers was approximated by

$$\bar{U}_i = \int_{z1}^{z2} \bar{\rho}_i dz \approx \bar{\rho}_i \Delta z, \quad i = 1,2 \tag{6.4}$$

Then, the optical depths were calculated by $\delta_i = k_i \bar{U}_i$, $i = 1,2$, where the $k_i's$ are the mass absorption coefficients for the respective layers. The dominant ($\geq 85\%$) contribution to these spectral absorption coefficients is due to continuum absorption which is comprised of a foreign broadening component and a water vapor broadening component ("e-type" absorption) as described by Paltridge and Platt. The component of the total mass absorption coefficient for layer i due to continuum absorption ($k_{\nu ci}$) is given by

$$k_{\nu ci} = k_{\nu 1}(T_i)p + k_{\nu 2}(T_i)e \tag{6.5}$$

where

- $k_{\nu 1}$ is the absorption coefficient for foreign broadening,
- $k_{\nu 2}$ is the absorption coefficient for water vapor broadening,
- T_i is the mean layer temperature, and
- p and e are the air pressure and water vapor pressures respectively.

(Paltridge and Platt (1976) give typical values of $k_{\nu 1}$ and $k_{\nu 2}$)

Next, the sky radiance was obtained by

$$I_{sky} = \epsilon_{sky1} B_{\Delta IR}(T_1) + \epsilon_{sky2} B_{\Delta IR}(T_2) Tr_{sky1} \tag{6.6}$$

where ϵ_{sky1} and ϵ_{sky2} are the emittances of layers 1 and 2 given respectively by

$$(1 - Tr_{sky1}) \text{ and } (1 - Tr_{sky2})$$

where

- Tr_{skyi}, $i = 1,2$ are layer transmittances given by
- $Tr_{skyi} = e^{-\delta i}$, $i = 1,2$, and
- $B_{\Delta IR}(T_i)$, $i = 1,2$ are the Planckian emissions for layers 1 and 2 having mean temperatures of T_1 and T_2 respectively.

Total sky transmittance was then determined as the product of the transmission functions for the layers, $Tr_{sky} = Tr_{sky1} * Tr_{sky2}$

Having determined the clear sky radiance and sky transmittance, the emissivity of the cloud was calculated as a function of LIRAD measured radiance from (6.3). Finally, by utilizing the equivalent TB_{IR} *vs.* ϵ_a scale (Figure 6.6), comparisons between the satellite and ground-based measurements were possible.

Time Series of Satellite and Ground-based Observations

Figure 6.7 summarizes the results of the analysis described above. A time series of the absorption emissivities derived from the LIRAD radiances measured at 15 second intervals is represented by the lower solid curve (right scale). One minute average emissivities are also plotted (dashed curve). The later curve is perhaps more appropriate for comparison with the satellite brightness temperature curve (upper solid curve, left scale) which was produced by analyzing the coincident line of data through the $10.8\mu m$ image at time increments of 1.9 minutes.

The correlation between the satellite and ground-based measurements plotted in Figure 6.7 is only fair. It is obvious from the previous discussion that certain errors will exist because of the inherent spatial and temporal complexity of the problem. Most of these errors were reduced by judicious selection of coincident data for analysis, but other problems were not resolved.

One factor directly affecting the results derived from the LIRAD radiance measurements was the correction made for clear sky radiance, I_{sky} in (6.3). Recall that this quantity was estimated using the Laverton soundings. The data obtained was removed from Aspendale both in time and space (see Figure 6.1). Moreover, the soundings were made from an inland station upwind from Port Phillip Bay, while the Aspendale LIRAD site is situated quite close to the coast and downwind from the bay. It is reasonable to conjecture that the atmosphere over Aspendale may have been significantly more moist than at Laverton due to moist air being advected over land from the bay. On the other hand, Laverton may have been drier under the influence of continental air being advected from the north-northwest. If this were the case, the layer optical depths might have been

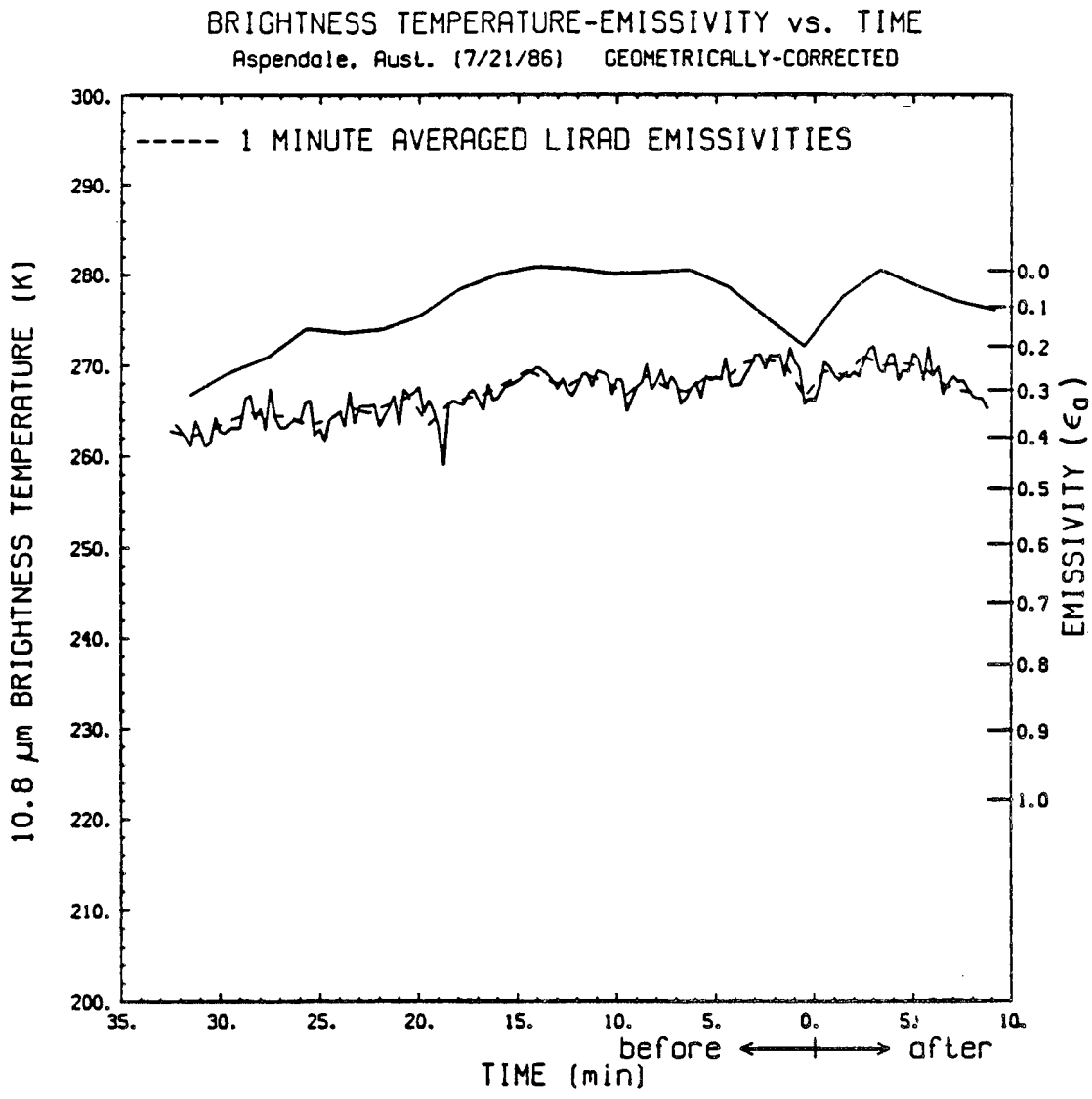

Figure 6.7: Time series of satellite (upper solid curve) and LIRAD (lower solid and dashed curves) brightness temperature-emissivity values for the Aspendale Cirrus Experiment, 7/21/86 referenced to the overpass time of NOAA- 9. Left and right scales are equivalent.

significantly greater than previously estimated leading to larger layer emissivities; thus, the sky radiance would have been greater. Consequently, the resulting cloud emissivities would have been lower than those plotted in Figure 6.7 which were computed for I_{sky} = 0.029 W m^{-1} sr^{-1}. To assess the effect of increasing the sky component of LIRAD radiances, I_{sky} was arbitrarily increased to 0.045 and the time-series reanalyzed. The results of this analysis are shown in Figure 6.8.

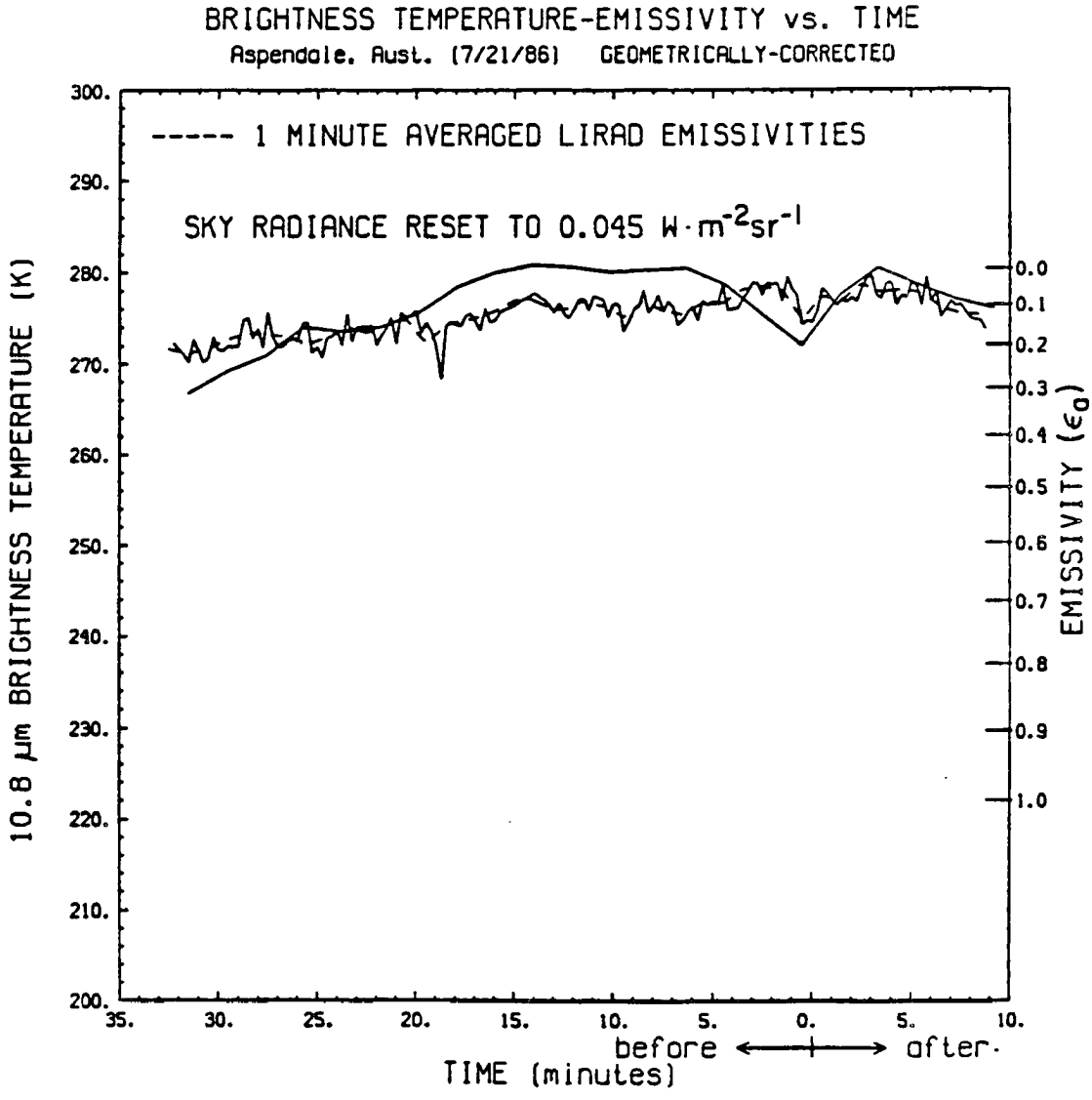

Figure 6.8: Time series of satellite and LIRAD brightness temperature- emissivity values as in Figure 6.7, but corrected for increased sky radiance as described in the text.

The correlation between the satellite and LIRAD emissivities in Figure 6.8 is now much better. In this figure, the satellite brightness temperatures still show greater ex-

cursions than those derived from ground-based radiance measurements, but the general trend of both curves is similar. Though the results shown in the later figure are purely speculative, they illustrate the importance of making reasonably accurate corrections for the contribution made by the sky radiance to the total measured LIRAD radiance for the purpose of deriving cloud emissivities.

The most plausible explanation for the poor correlation shown in Figure 6.7 is the likelihood that the radiometer was miscalibrated. In a personal communication from Platt (4/28/87) he suggests that the calibration blackbody may have been contaminated with frozen vapor leading to significant errors in emittance values. Therefore, the results presented above must be viewed with caution.

Comparison of Observations and Radiative Transfer Calculations

The analysis of the 7/21/86 Aspendale Cirrus Experiment is concluded in this section. An example is given of how the radiative properties of a cirrus cloud may be deduced utilizing the spectral differencing method in conjunction with the pertinent theoretical simulations. By comparing the observed brightness temperature differences interpolated along the line of cloud motion to the theoretical plots of ΔTB *vs.* τ for different microphysical indices (refer to Figure 5.7), a MP-index characterizing the cirrus deck was determined. Then, the cloud optical properties were assumed to be those listed in Table 3.3 for that index. And finally, theoretical and observational time series of optical depth were produced assuming the deduced radiative properties in an attempt to validate the method. Time series of the interpolated brightness temperatures for the NIR and IR window channels of NOAA-9's AVHRR and their differences are plotted in Figure 6.9. The error associated with the temperature curves in Figure 6.9 is largely due to random interpolation errors and are not likely to be greater than ± 0.5 K leading to potential errors in ΔTB of about $\pm 1^{\circ}$ C.

To compare the interpolated results plotted in Figure 6.9 with theoretical calculations, each pair of points defined by $(TB_{IR}(t), \Delta TB(t))$ corresponding to a time step (t) were plotted on the family of curves presented in Figure 5.7 assuming different TB_{IR} curves as a function of MP-index. For example, at a time corresponding to 14 minutes before the

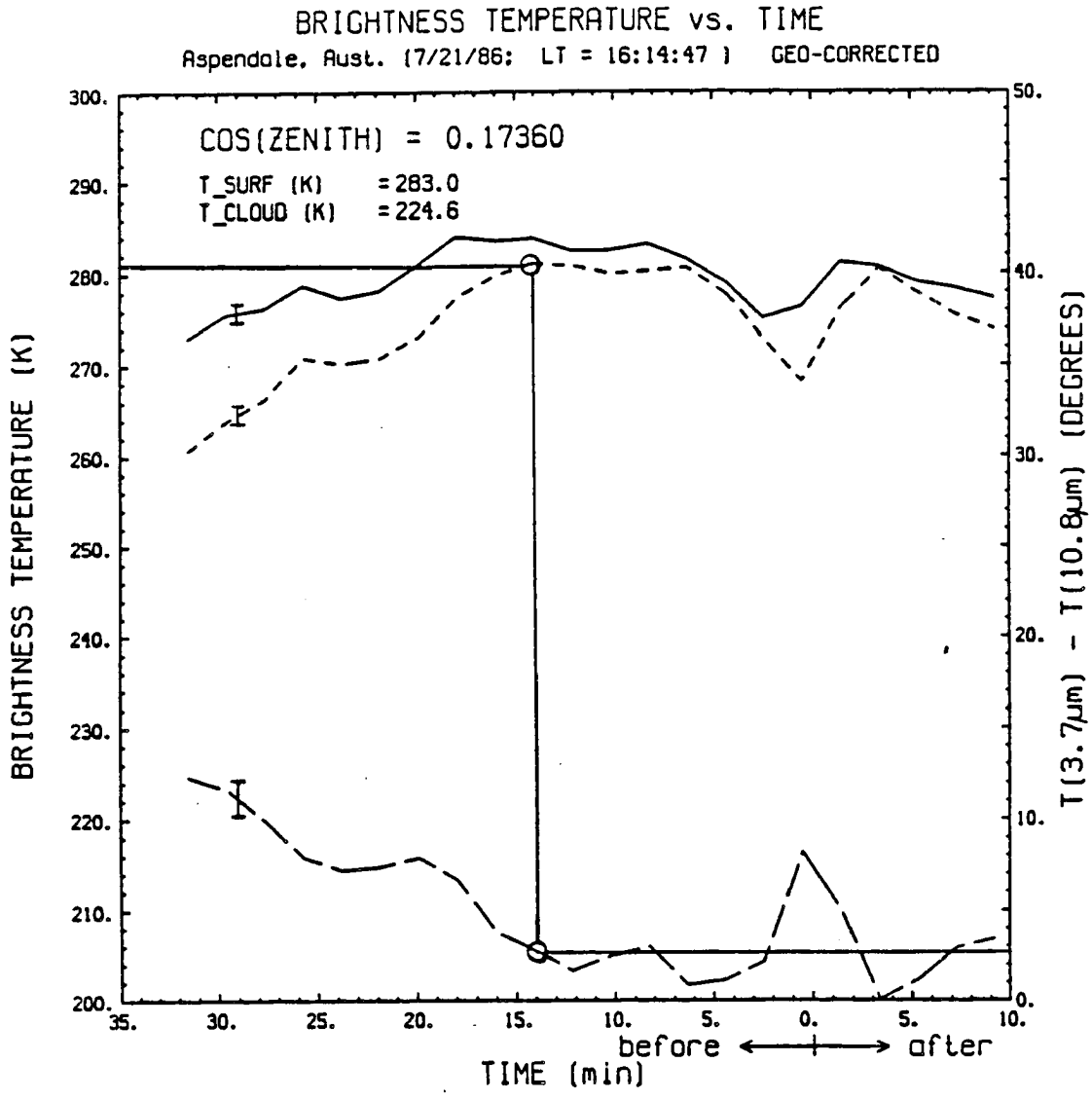

Figure 6.9: Time series of the NIR (solid curve) and IR (dashed curve) satellite brightness temperatures (left scale) and their differences (bottom curve, right scale) for a line of pixels coincident with LIRAD observations for the Aspendale Cirrus Experiment, 7/21/86. Circled points are described in the text.

overpass time, $TB_{IR} \approx 281K$ and $\Delta TB \approx 2.8$ indicated by the circled points in Figure 6.9. Assuming an index of MP-5, a dot was placed at the intersection of a vertical line drawn from $TB_{IR} = 281K$ along the $10.8\mu m$ temperature curve corresponding to MP-5 and a horizontal line representing $\Delta TB = 2.8$ (right scale) as is illustrated in Figure 6.10. A cluster of points resulted for each MP-index representing all the time steps in the time series. By inspecting these clusters relative to their respective theoretical ΔTB curves a "best fit" was visually selected and the index for that curve was taken to represent the microphysical properties of the cloud. The best fit determined in this case was for MP-5 which is presented in Figure 6.10. The points chosen as an example in Figure 6.9 are again circled to further elucidate the procedure used in forming the cluster.

The agreement between simulated and observed brightness temperature differences as a function of TB_{IR} is surprisingly good for MP-5. This is especially true for optical depths greater than about 0.4. The scatter of points is greater for thin clouds with depths in the range of 0.15 to about 0.4, but is rather symmetric and well fit by the theoretical curve. This region of broader scatter relates to clouds with emissivities of less than about 0.1 for which only single scatter and second order scatter prevail. Perhaps the anisotropic nature of scattering by the large particles represented by MP-5 may cause the increased noise evident in this regime. For still thinner clouds the fit appears to improve, but curves of other MP- indices are equally well-fit in this region since all the ΔTB curves converge in the clear sky limit. Due to this fact and the the small brightness temperature differences that exist for very thin clouds (within the noise level of measurement/interpretation), it is recommended that the selection of a microphysical model be made based on observations of thicker clouds if possible to avoid ambiguity. For the case presented here, the agreement is sufficiently good to deduce the microphysical state of the cloud with some degree of confidence. Thus, the radiative properties of the Aspendale cirrus are assumed to be those listed in Table 3.3 for index MP-5.

Though the cirrus cloud investigated for this study is quite cold and one might expect the the microphysics to be characterized by many small ice crystals (e.g., bullets and rosettes) with low ice water content as suggested by the observations discussed in Section

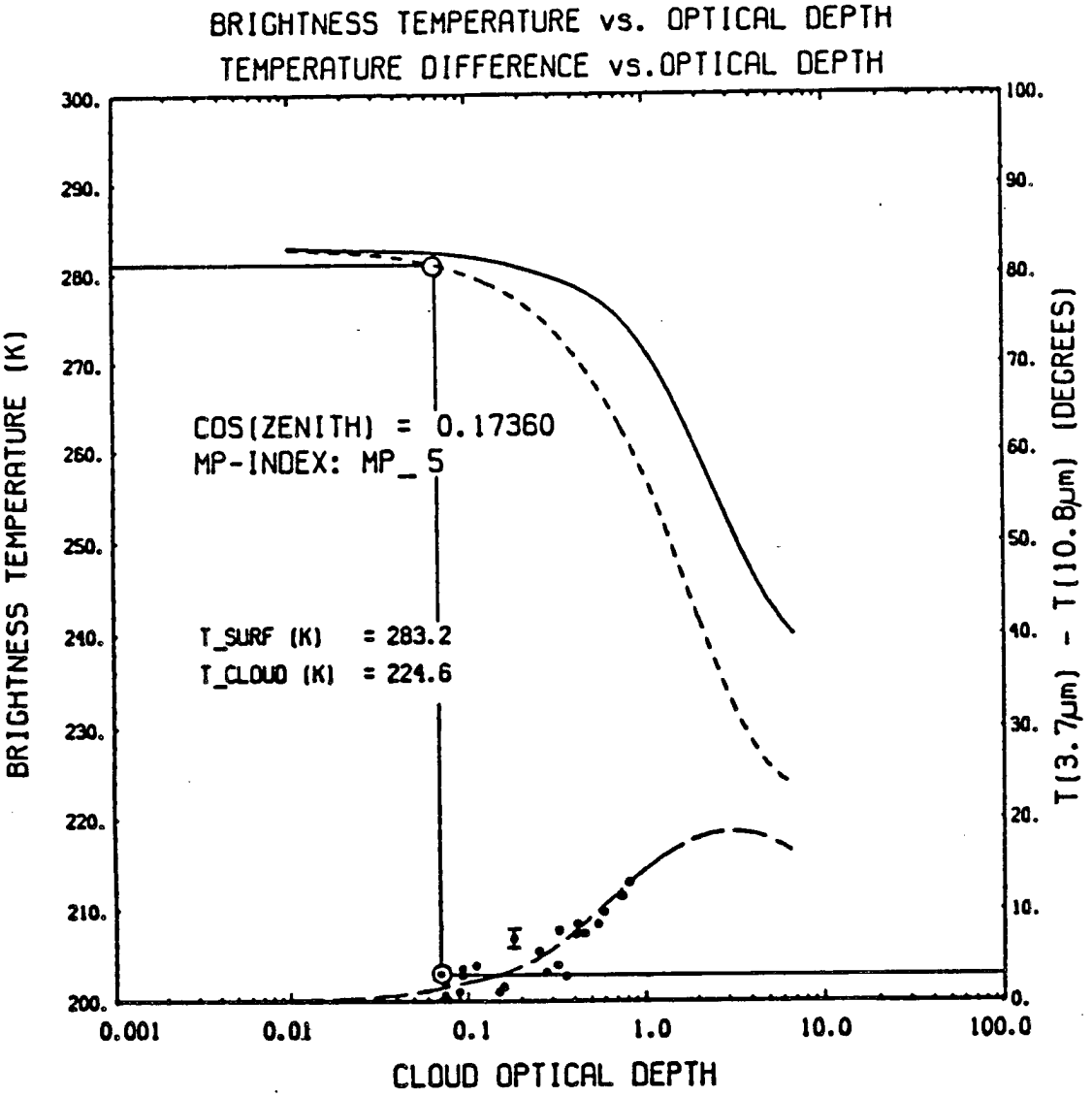

Figure 6.10: Theoretically determined NIR (solid curve) and IR (dashed curve) brightness temperatures and differences (long dashed curve) as a function of cloud optical depth for MP-5 (Table 3.3). Each point in the cluster corresponds to a step in the time series plotted in Figure 6.9. Circled points relate to those discussed in the text.

3.3.1, a MP-index characterizing large particles, low volume density and relatively large IWC was selected to characterize the cloud (e.g., Tables 3.1 and 3.3). This anomaly was borne-out during the analysis of the integrated backscatter returns measured by the Aspendale lidar. Very large values indicated a high probability of larger plate crystals oriented in the horizontal which is rarely observed at $-50°C$ (Platt, communication, 1987).

Simulated and Derived Time Series of Optical Depth

Using the inferred value for the single scattering albedo ($\tilde{\omega}_o$) for MP-5, estimates of the total cloud optical depth as a function of time (distance) for the satellite and LIRAD observations were finally made and compared to the simulated results for the model cloud as follows.

Noting that the absorption emissivity of the cloud is given by $\epsilon_a = 1 - e^{-\tau_{abs}}, \tau_{abs}$ (the absorption optical depth) can be calculated knowing ϵ_a derived from the radiance measurements. Then, by assuming $\tau_{abs} = (1 - \tilde{\omega}_o)\tau$, the total cloud optical depth τ can be approximated by

$$\tau \approx \frac{\tau_{abs}}{(1 - \tilde{\omega}_o)} \tag{6.7}$$

noting that $\tau = \tau_{abs} + \tau_{sca} = \tau_{abs} + \tilde{\omega}_o\tau$; τ_{sca} being the optical depth due to scattering alone.

Therefore, by knowing the value of the single scattering albedo $\tilde{\omega}_o$ extapolated from the spectral differencing approach described above, time series of τ for the Aspendale cirrus deck were produced. These are presented in Figure 6.11. The solid, dashed and dot-line in the figure represent the satellite, LIRAD and theoretical results respectively. The former two were derived from equation (6.7) after τ_{abs} as a function of time was computed from $\epsilon_a(t)$ (see Figure 6.7). The theoretical curve was produced from interpolated values of τ for the cluster of points in Figure 6.10, each point chronologically ordered by time step.

As expected from the results shown in Figure 6.10, fair agreement was found for the satellite derived curve and the simulated curve for MP-5. The poor correlation of either of these curves with the LIRAD curve is explained by the poor correlation between the respective emissivities given in Figure 6.7.

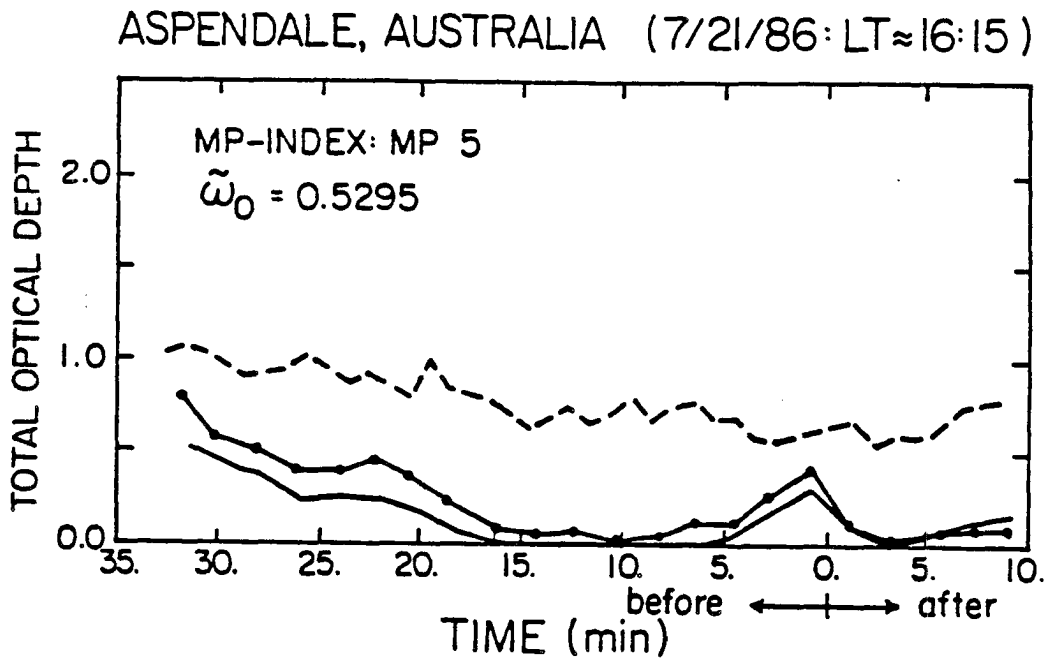

Figure 6.11: Time series of total cloud optical depth, τ for satellite (solid curve), LIRAD (dashed curve) and simulated (dot- line) results described in the text.

6.2 Satellite Applications, GOES MSI Case Study

The case study presented in Sections 6.1 provided a means to validate the spectral differencing method used for estimating cirrus cloud optical properties, but certain disadvantages due to differences in the temporal and spatial resolution of the LIRAD and satellite measurements were inherent in that approach. A significant amount of effort was required to deal with the geometric complexity of the problem. In addition, field experiments such as those conducted at Aspendale are costly, resulting in a scarcity of these types of data available for analysis. Therefore, simpler methods for deducing the radiative state of cirrus clouds are needed for general use.

6.2.1 Cirrus Cloud Study, 4/15/86 21GMT

In this section, an efficient technique to infer the microphysical and radiative properties of cirrus clouds is developed. In addition, the results from this procedure are used to demonstrate how a "map" of cirrus cloud optical depth can be produced. Again, the spectral differencing method is employed. Only bispectral data from the GOES-6 VAS

radiometer and nearby radiosonde data are necessary in this technique. Though radiative transfer simulations must be made for the proper solar zenith and satellite viewing angles, there are no other complicating geometric constraints to contend with.

The VAS images used in this study were collected at the CSU ground station through the GOES-TAP and all subsequent processing and analysis was performed using the interactive research imaging system (IRIS) and various computer programs run on CSU's VAX-VMS operating system.

Location and Data for the 4/15/86 Cirrus Study

A visible image of the sector analyzed below is presented in Figure 6.12. It lies mainly over the Pacific Ocean off the southern coast of California; Los Angeles is located near the upper right hand corner. This sector spans approximately 5.6° in latitude and 7.3° in longitude (or an area of approximately 627 km N-S by 685 km W-E). The cloud band streaming diagonally across the image is the focus of this study. It was part of an extensive cirrus cloud system associated with a moist flow of tropical air driven by the subtropical jet stream. The rectangular subsector highlights the thickest (coldest) portion of the cirrus deck and the circled area contains mainly low water clouds. These features and the line within the rectangular sector will be pertinent to the following analysis. A map view of a portion of this sector is shown in Figure 6.13 with the upper level winds, cirrus cloud axis and radiosonde stations indicated.

Data from two radiosondes were used to estimate the height and deduce the mean cloud temperature of the high clouds in this image. The similarities in the soundings from Edwards Air Force Base made 9 hours prior to, and from San Diego made 3 hours after the images were collected, suggest that fairly constant synoptic conditions prevailed over this region at 2100GMT. Therefore, the extrapolations of the cloud height and temperature from these data are reasonable. The rawinsonde data used in this analysis are shown in Figure 6.14.

A distinct high moist layer persisted near the lower level of the jet stream which clearly locates the cloud top. The mean cloud temperature was approximated as $-38°C$ at an altitude of about 9.1 km. It was not possible to determine the precise vertical extent

Figure 6.12: Visible (VISSR) image of the cirrus deck associated with the subtropical jet stream, 4/15/86 21GMT. See text for description of highlighted subsectors.

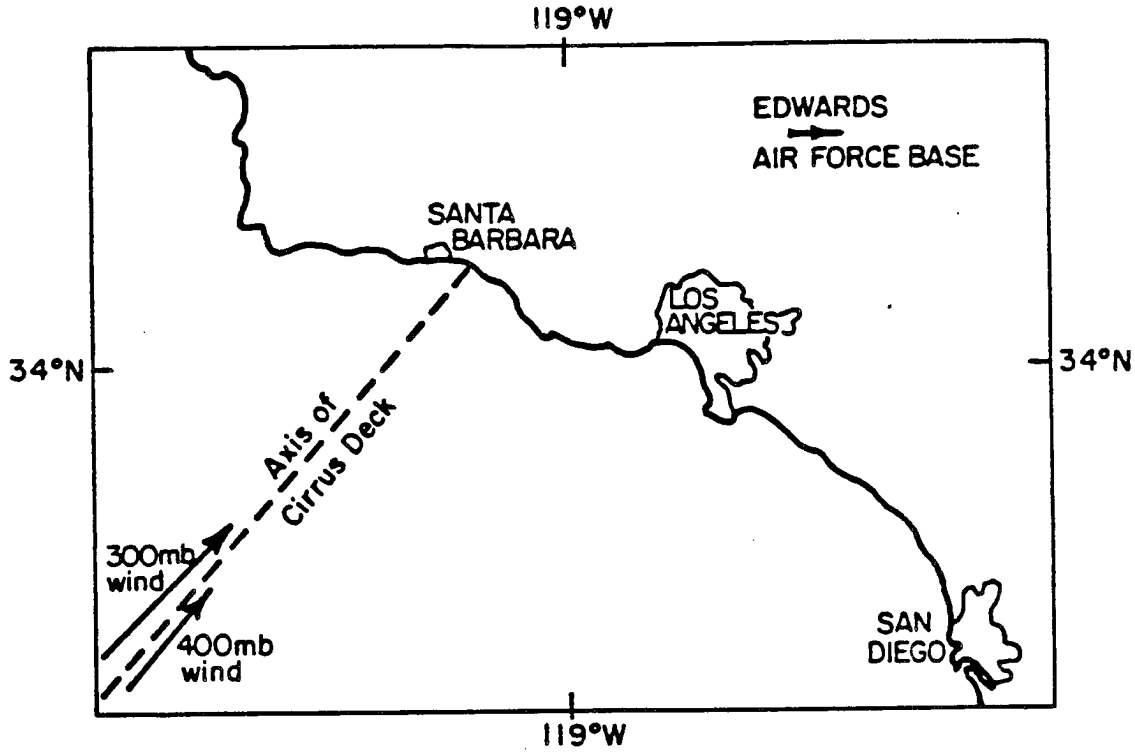

Figure 6.13: Map of a portion of the 4/15/86 21GMT sector showing the jet stream relative to the axis of the cirrus deck. Wind vectors were extrapolated from the 4/16/86 00GMT San Diego sounding shown in Figure 6.14.

of the cirrus deck as the dew point depression used to infer the presence of cloud did differ between the soundings, indicating spatial and/or temporal variation in cloud thickness. Despite obvious spatial variations in cloud thickness, it was assumed that the cloud was isothermal and that the microphysical and radiative properties were constant throughout the layer.

Figures 6.15 (a) and (b) are the NIR (3.9μm) and IR (10.8μm) images that correlate to the visible image pictured above. Due to the sensor configuration of the VAS radiometer, the NIR resolution is about 4x16 km and the IR resolution about 4x8 km. Since these images are only compared to one another, no remapping to correct for pixel elongation was necessary in this case. However, the 10.8μm image was "reduced" to match the resolution of the 3.9μm image to enable computation of brightness temperature differences (pixel by pixel). These images were enhanced using the function shown in Figure 6.16. This step function was constructed to fully utilize the dynamic range (0-255) of the gray scale available on the CSU Comtal display system, and the function's count value range was

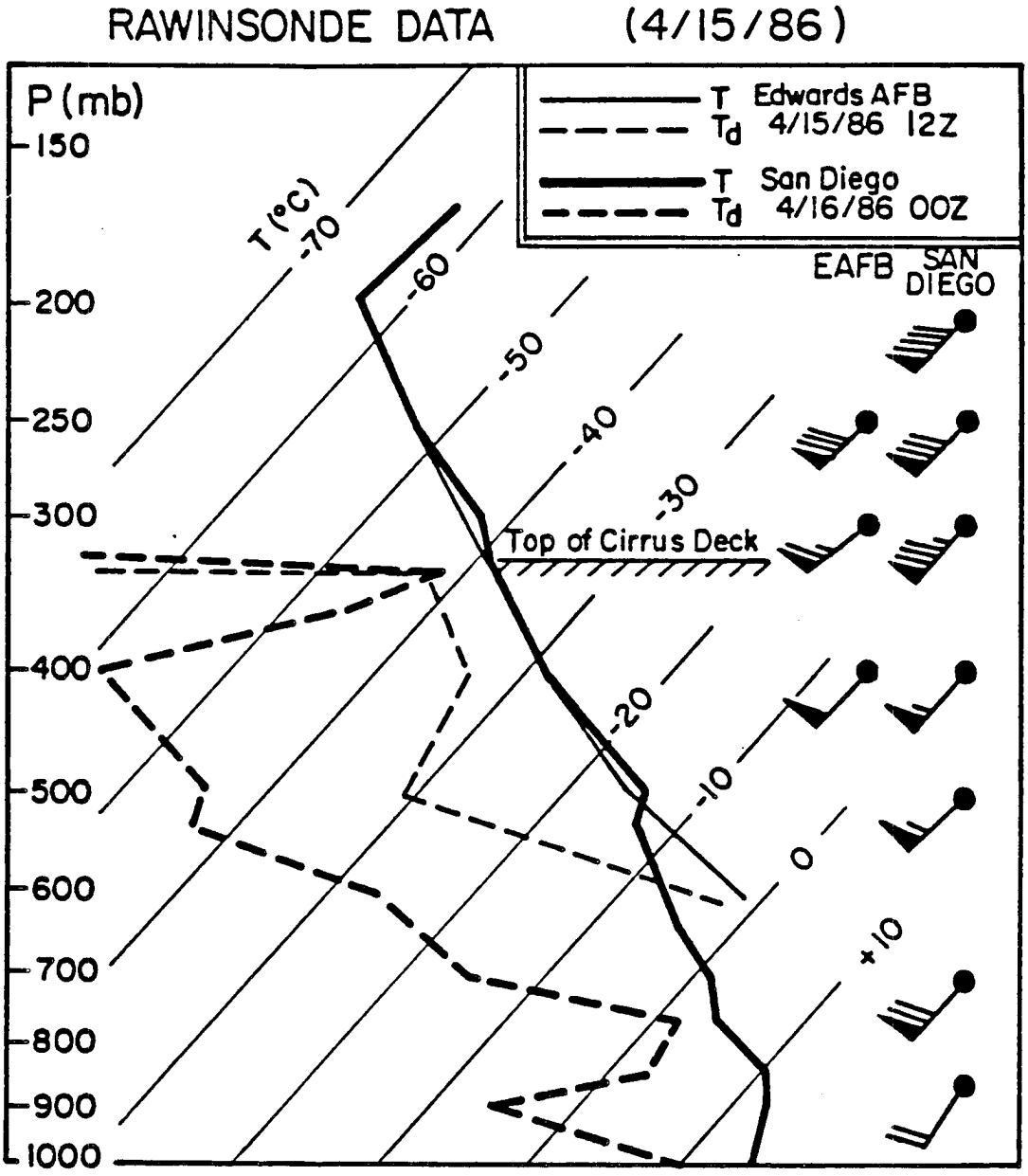

Figure 6.14: Vertical soundings of the atmosphere taken 9 hours before (at Edwards AFB) and 3 hours after (at San Diego) the 4/15/86 21GMT images were collected. An estimate of the cirrus cloud top is indicated.

based on the 1-D histograms of the images (Figures to follow). In addition, the images were "smoothed" to reduce the blockiness ordinarily associated with large pixel elements. For the convenience of interpretation, the different areas of gray shading have been labelled with the average brightness temperature characteristic of that area.

The differences in brightness temperatures described theoretically in Section 5.1 (see Figures 5.3 and 5.7 for simulations) are evident by comparing Figures 6.15 (a) and (b). Two regions have been highlighted to point out the interesting features of these images. The rectangular subsector contains cold (high) clouds and open ocean, while the circled area contains mostly warm (low) clouds and open ocean. Comparing the NIR and IR images to the visible image, it is clear that brightness temperature differences (ΔTB) are greater for optically thick clouds; i.e., those with higher visible albedo (whiter regions of the visible image) than for thinner clouds as indicated by the radiative transfer simulations presented in Chapter 5. Recall that ΔTB, during the day, is largely due to the added component of reflected NIR radiation which increases as the optical depth of the cloud increases. This contribution to the upwelling radiance is even larger for low, moderately thick water clouds (circled) so that these clouds actually appear to be warmer (i.e., blacker in Figure 6.15 (b)) than the adjacent sea surface.

Determination of Surface Temperature

The mean cloud temperature was inferred from the soundings as discussed above, but the surface temperature, also required to initialize the radiative transfer model, may not necessarily be the same as that extrapolated from these soundings because the temperature profiles were made over land and the sector analyzed was mainly over water. The advantage in selecting a case over the ocean was discussed in section 5.1.4 (see Figure 5.1); i.e., the spectral albedo of water for these window wavelengths is negligible assuring reliable results from a model in which surface reflection has been ignored. The 4/15/86 case was also a good one to study because there are distinct cloud-free areas and other areas that appear to be uniformly cloudy. The determination of surface temperature and radiative properties of homogeneous cloud surfaces can be objectively made under these

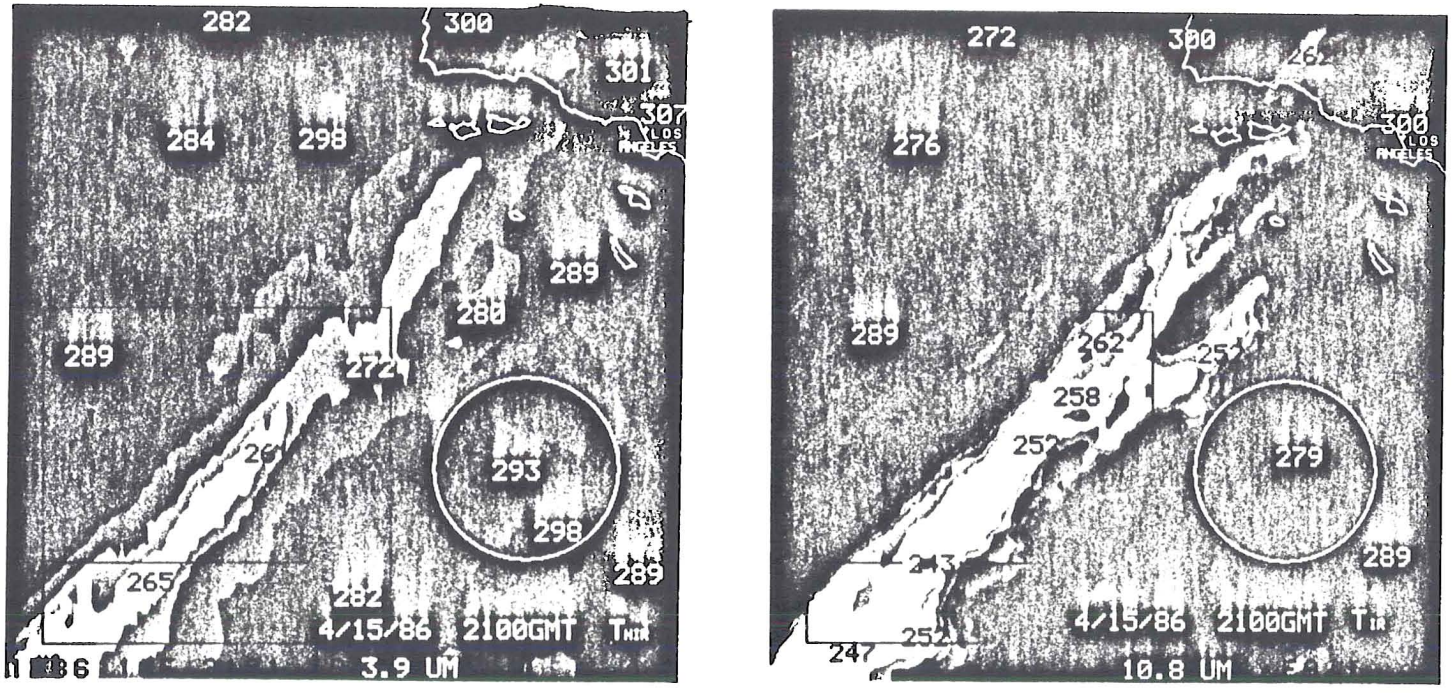

(a) (b)

Figure 6.15: (a) NIR and (b) IR images for the 4/15/86 21GMT case study. Numbers represent average brightness temperatures for the gray tone diefined by the enhancement curve shown in Fig. 6.16. Subsectors are described in the text.

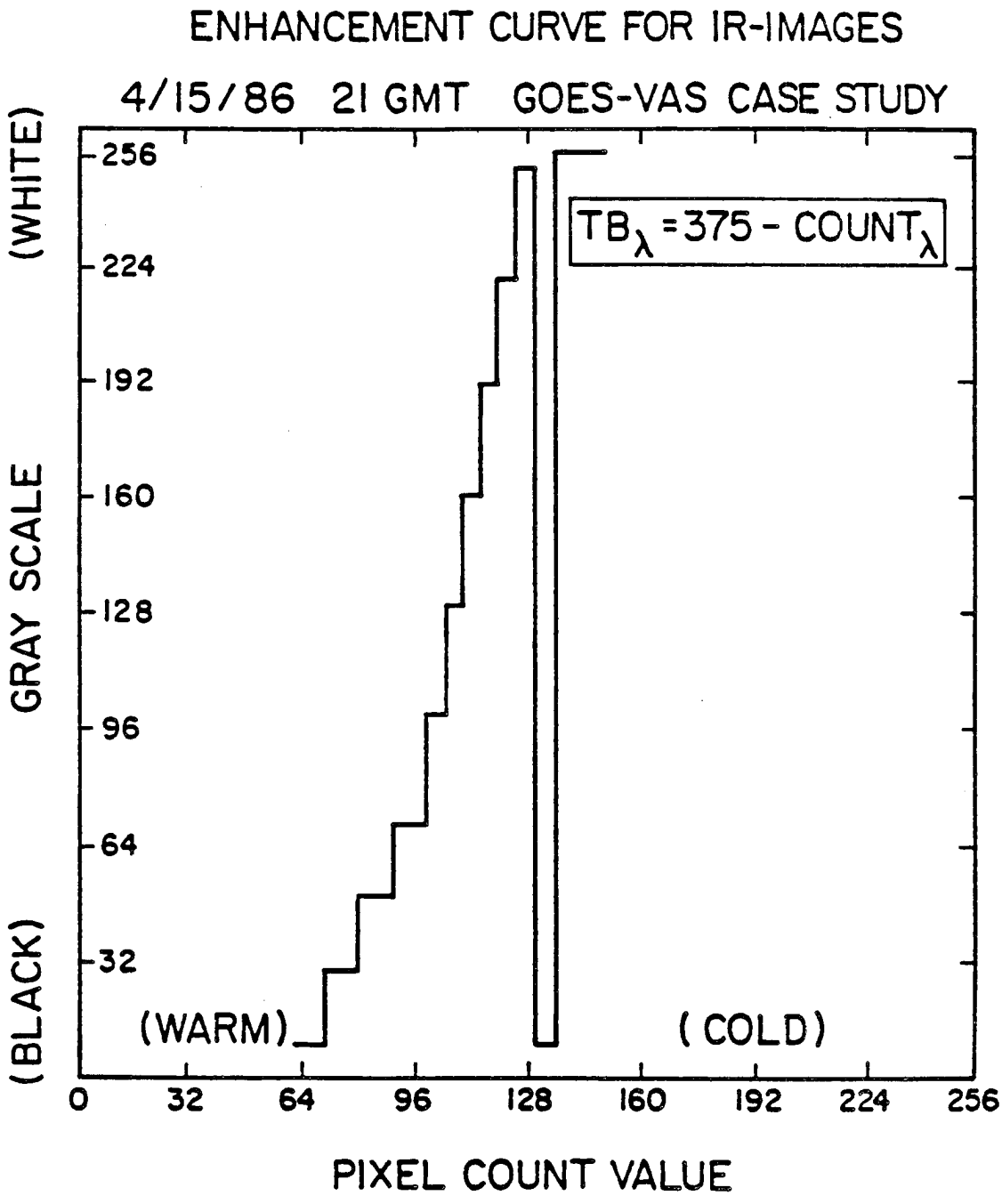

Figure 6.16: Enhancement curve applied to the NIR and IR images for the 4/15/86 21GMT case study presented in Figures 6.15 (a) and (b). See text for description.

conditions utilizing a technique referred to as the Neighbor-to-Neighbor Method (NTN). Cox, Ackerman and Vonder Harr (1986) describe this technique in the following manner.

Assuming that the variation of measured radiance is small for a given surface type compared to the measured radiances for other surface types, e.g., cloud vs. sea surface, a two dimensional histogram of adjacent pixel brightness temperatures can be constructed and analyzed employing an objective clustering technique to identify the most uniform features in a satellite image. That is, the value of the brightness temperature for the N^{th} pixel is plotted against the value of its neighbor, (N+1), and a cluster technique (e.g. Debois et al., 1982) is used to contour the normalized values of the total number of each (N, N+1) pair stored in an array. Uniform features are then easily identified along the diagonal of the histogram since points lying on this line represent identical neighboring pixel values and non-identical, but closely matched pairs cluster near the diagonal; the greater the number of similar pairs, the more defined the cluster. Cox et al. found that, by utilizing this method, surface temperature could be retrieved from the "cleaner" NIR image to within $1°C$ of aircraft-measured surface temperature. Therefore, the NTN method was employed here to estimate the sea surface temperature. Figures 6.17 (a) and (b) show the results of these NTN analyses for the respective images. Normalization of the count array was based on the maximum number of specific (N,N+1) pairs counted, and contours were drawn at 0.1 intervals (algorithm supplied by Ackerman, 1986). The results of the clustering analyses for 4 "peaks" are given for each figure. Peak 1 of the $3.9\mu m$ NTN analysis clearly relates to the sea surface temperature ($\approx$ 289 K) in that image. Note that the IR derived surface temperature was actually greater than the NIR temperature in this case which is contrary to what normally would be expected (see section 5.1.3). This discrepancy is possibly due to a temperature inversion, which may have existed above the sea surface at the time the images were collected (1 PM LT), giving rise to a greater contribution to the upward radiance due to continuum emission at $10.8\mu m$ compared to the $3.9\mu m$ continuum emission. The one dimensional histograms associated with the NTN plots in Figure 6.17 are presented in Figures 6.18 (a) and (b). From these histograms, the total range of count values for the images was determined for use in construting the enhancement curve shown in Figure 6.16.

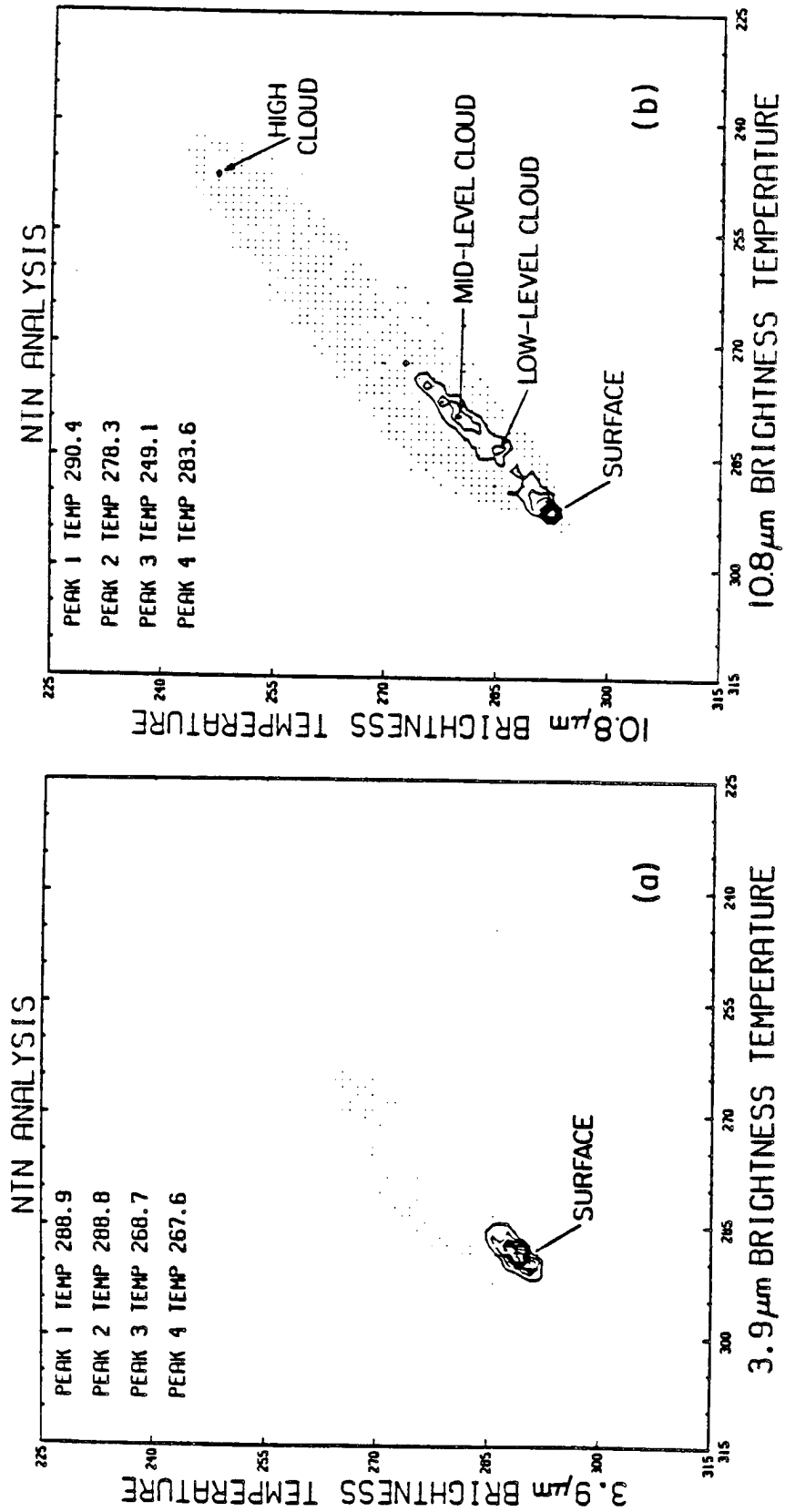

Figure 6.17: NTN cluster analysis for the (a) NIR and (b) IR images shown in Figure 6.15.

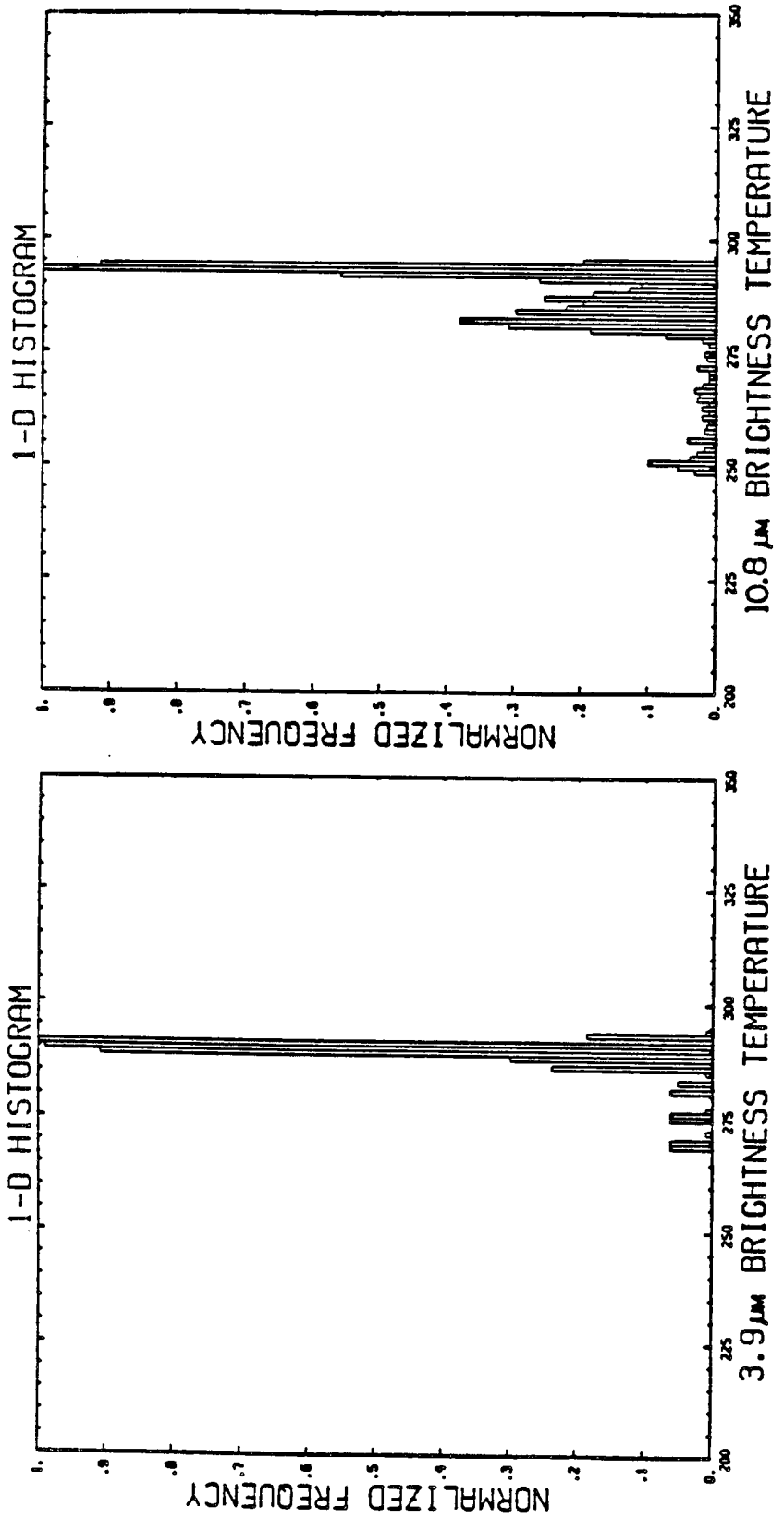

Figure 6.18: One dimensional histograms for the (a) NIR and (b) IR images shown in Figure 6.15.

In addition to determining surface temperature, the NTN clusters can be used to identify distinctly different cloud features. For instance, peaks 2, 3 and 4 in the $10.8\mu m$ NTN diagram suggest the presence of three distinct cloud types within the sector. Peaks 2 and 4 are associated with mid-level and low clouds respectively. Peak 3 identifies the cirrus deck. These features are not apparent in the $3.9\mu m$ NTN diagram because of the peculiar characteristics of radiative transfer in the NIR window region. Due to the enhanced reflection by thicker clouds, the range of NIR brightness temperatures is greatly reduced, diminishing the usefulness of the NTN method for identifying features other than the surface temperature for this spectral band.

Simulations and Selection of Microphysical Model

Once the surface and cloud temperatures were estimated, radiative transfer simulations were made for a quadrature angle that approximately matched the satellite viewing angle, and comparisons with the actual satellite derived brightness temperatures were then made. In this case, it was sufficient to run simulations for only three model clouds (MP-3, 4 and 5). The procedure follows that described in section 5.3. Plots of ΔTB *vs.* τ were generated for the specific boundary conditions and viewing geometry related to the 4/15/86 case. These results are presented as the family of curves shown in Figure 6.19. The cluster of points was produced analogously to the cluster shown in Figure 6.10 for the Aspendale study.

This analysis consisted of determining the IR brightness temperatures (TB_{IR}) and differences in brightness temperatures (ΔTB) along the line indicated within the rectangular subsector in Figure 6.15. This line of image elements was selected because a maximum range of ΔTB was observed to occur along this cross section insuring a broad spread of points making up the cluster. The results of this pixel-by-pixel analysis are presented in Figure 6.20. The solid curve in this figure relates to the left scale (TB_{IR}) and the dashed curve for ΔTB relates to the right scale.

The procedure used to deduce the MP-index of the cirrus layer was to plot points on the simulated family of curves corresponding to $(TB_{IR}, \Delta TB)$ pairs as was done for the time series in Section 6.1. A point was plotted for each pixel along the line assuming

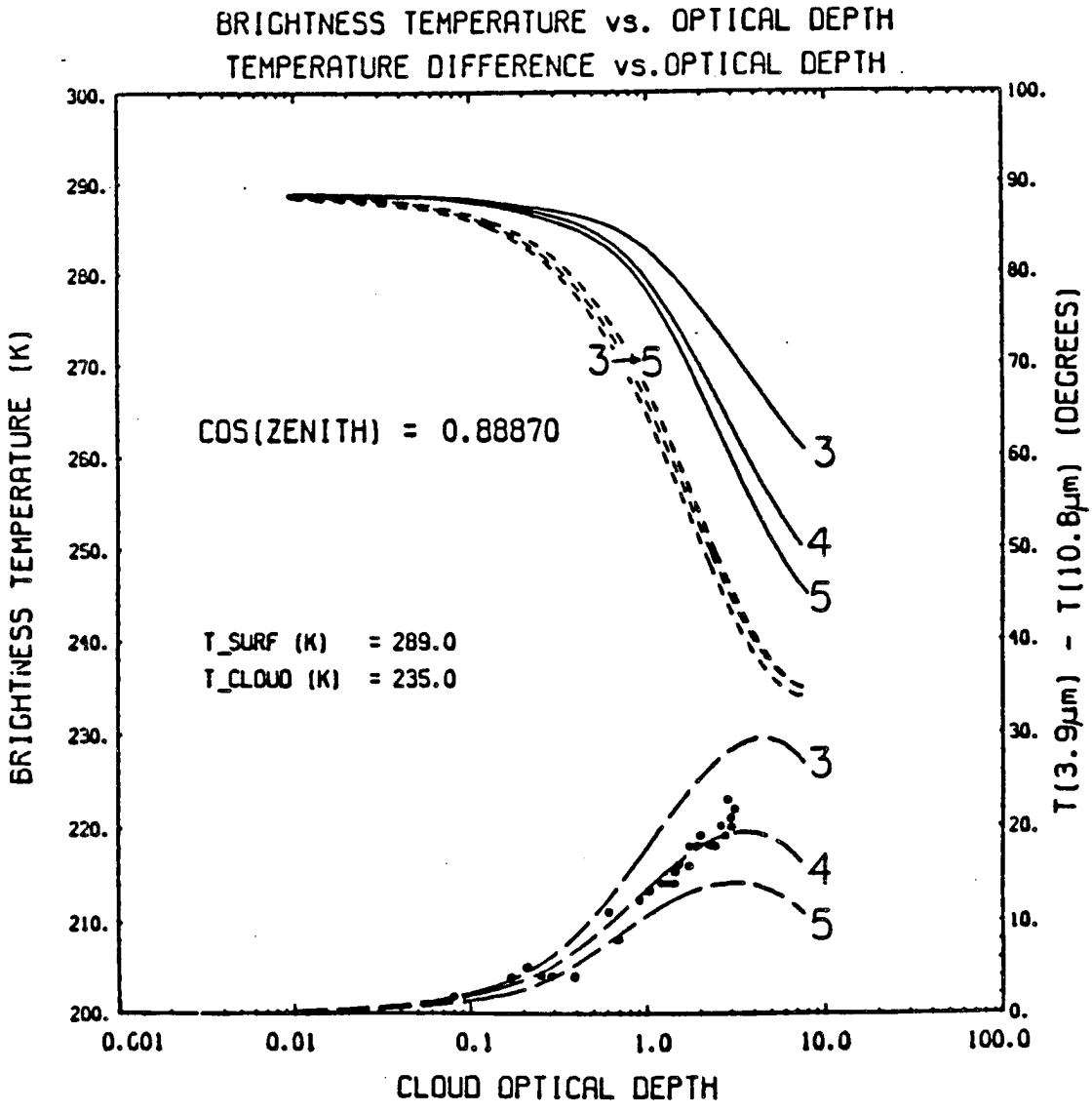

Figure 6.19: Family of curves relating ΔTB to τ for the microphysical model indices indicated. Solid and dashed curves are for $3.9\mu m$ and $10.8\mu m$ brightness temperatures respectively (left scale) and the long dashed curves are for ΔTB (right scale). (See Table 3.2 for radiative properties.)

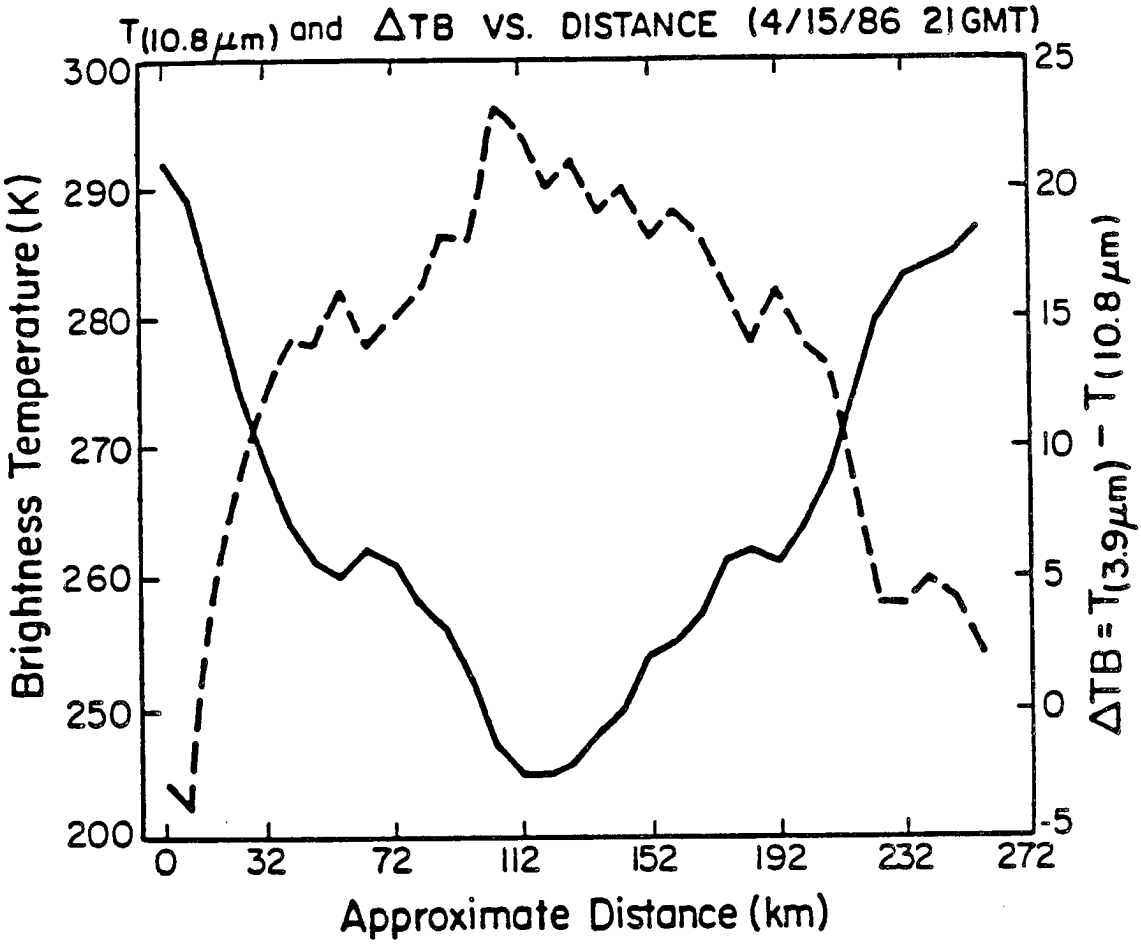

Figure 6.20: Cross-sectional analysis of TB_{IR} (solid curve, left scale) and ΔTB (dashed curve, right scale) for the line indicated in Figure 6.15.

varying MP-indices and the index of the ΔTB curve which best fit the resulting cluster of points was taken to represent the microphysical properties of the cloud. MP-4 was an obvious choice for this cloud.

Mapping Cirrus Cloud Optical Depth

As a final demonstration of the usefulness of the spectral differencing method, the NIR and IR image sectors were differenced and analyzed with respect to the simulated relationship between ΔTB and r for a model cloud characterized by MP-4. An enhancement curve was constructed for the purpose of highlighting different ranges of ΔTB relating to intervals of optical depth as the scale in Figure 6.21 below indicates.

The enhancement curve in Figure 6.21 was applied to the differenced image and the image labelled appropriately to show the variation of optical depth in correspondence to the enhancement table. A "map" of cloud optical depth for the cirrus layer was effectively produced following this procedure. Figure 6.22 is such a map for the subsector shown in Figure 6.15. The labelled values in this figure represent the average optical depth for the respective areas of gray shading.

It must be noted that the usefulness of such a map is limited in that the intervals of optical depth (labelled in the figure), apply only to ice clouds with microphysical properties defined by index MP-4. Applying the same enhancement curve to warm water clouds yields dubious results at best. The methodology developed above may certainly be modified for other cloud types by constructing the appropriate microphysical tables (e.g., Arking and Childs, 1984) and performing radiative transfer simulations initialized for realistic optical properties of these cloud types. The problem of producing a map of cloud optical depth for different cloud types within the same image sector may be possible by applying this technique successively to different cloud types and constructing composite overlays. There is obvious merit to the above approach, but many more cases must be analyzed and validated before any sort of objective scheme for its implementation can be devised. The data collected during the 1986 FIRE project designed to investigate cirrus clouds should provide an excellent data base for validating and improving upon this technique.

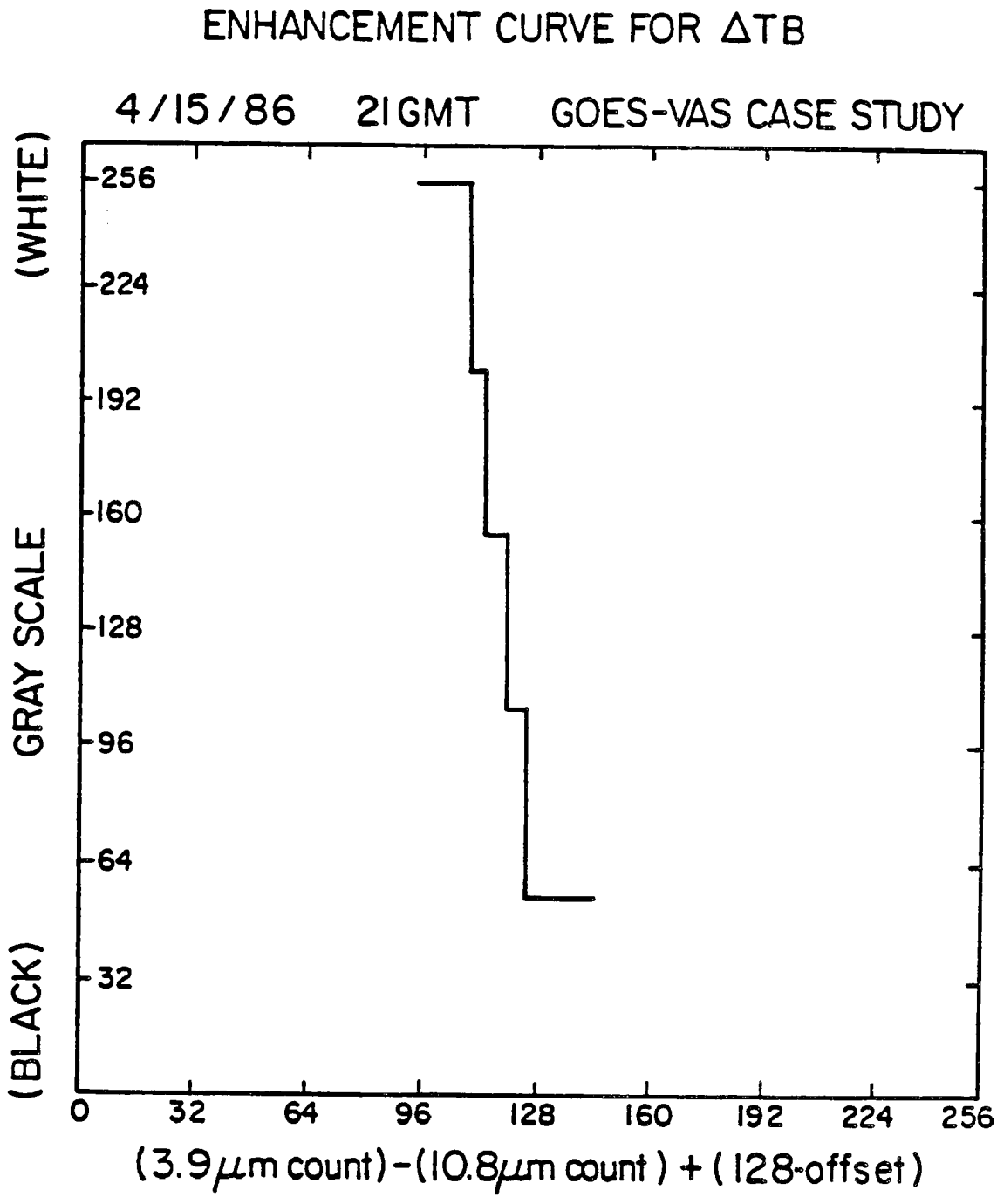

Figure 6.21: Enhancement curve used to highlight areas of varying optical depth based on the simulation for MP-4 in Figure 6.19. The conversion table defines the intervals selected.

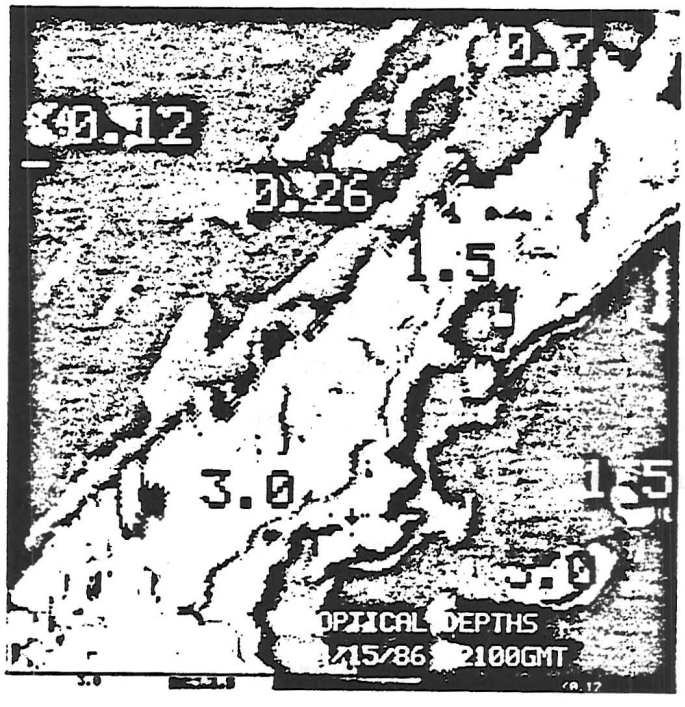

Figure 6.22: Map of cloud optical depth for the cirrus deck highlighted by the rectangular subsector in Figure 6.15. Values are representative average optical depths for intervals tabulated in Figure 6.21.

Chapter 7

SUMMARY, CONCLUSIONS, AND RECOMMENDATIONS

Cirrus clouds, by virtue of their global distribution, high altitude and distinctive microphysical and radiative properties, significantly influence the radiative energy balance of the earth-atmosphere system. *In situ* observations of cirrus show large variations in their general characteristics which complicates the parameterization of these clouds in numerical weather or climate models. The presence of cirrus in the atmosphere can cause heating by the greenhouse effect or cooling by the albedo effect depending on the optical depth, altitude and radiative properties of the cloud system. To better understand these processes, methods to determine cirrus radiative properties are needed. The International Satellite Cloud Climatology Project (ISCCP) was established to coordinate the collection and distribution of data necessary to study various cloud/radiative-dynamical feedback mechanisms and to monitor the earth's cloud climatology with a focus on large scale marine stratus and cirrus cloud systems.

The objectives of this study were to explore the microphysical and radiative properties of cirrus clouds, compare radiative transfer simulations of model clouds with observed cirrus and to develop a technique to approximate their optical properties. The relationship between differenced NIR and IR window radiances and cloud optical depth (the spectral differencing method) forms the theoretical basis of this approach.

7.1 The Radiative Transfer Equation and Model

An appropriate monochromatic radiative transfer equation for this study was introduced in Chapter 2. This equation describes the transfer of radiation through a plane-parallel horizontally homogeneous absorbing-emitting and scattering atmosphere, including sources of thermal emission within the layer. The integro-differential form of this

equation was reduced to an easily solved system of linear equations involving only the global transmission and reflection functions and boundary conditions of the layer. To make this simplification, the radiation field was discretized into a carefully selected set of incident and response angles and Guassian quadrature was employed to represent the the integral expressions appearing in the transfer equation. Azimuthal independence of the radiation field was assumed and the Henyey- Greenstein approximation to the phase function was used. The resulting matrix form of the transfer equation was solved using an efficient and accurate doubling routine beginning with an infinetesimally thin layer and building up the layer to the total optical depth of the cloud.

7.2 Cirrus Microphysical and Radiative Properties

Several parameters were required to initialize the radiative transfer model used in this study. To compare model results with satellite observations, surface and cloud temperatures, solar zenith and satellite viewing angles and the appropriate wavelengths to match the satellite radiometric data were required. In addition, specification of the cloud optical properties ($k_{ext}, \tilde{\omega}_o, g$ and τ) were required. No a priori knowledge of these radiative properties existed for the clouds studied. Therefore, model clouds were constructed to simulate naturally occuring cirrus in the atmosphere and comparative analysis was employed to deduce actual conditions.

The notion of microphysical indices (MP-indices) was introduced in Chapter 3. A complex interrelationship between crystal habit, volume density and ice water content in high level clouds, all dependent on temperature was noted. Though cirrus clouds are composed of a variety of nonspherical ice particles (possibly oriented in the horizontal plane), distributions of ice spheres were used here to simulate cirrus composition, enabling the use of a Mie algorithm to calculate values of the radiative properties for each MP-index. The results for five model clouds were listed in Tables 3.2 and 3.3. Plots of $g, \tilde{\omega}_o$ and k_{ext} (Figures 3.2, 3.3 and 3.4) clearly illustrated the codependence of these parameters on MP-index and wavelength.

The differences in observed spectral brightness temperatures (ΔTB), used to infer optical depth (τ), are primarily due to differences in radiative properties varying as functions

of the size parameter χ, defined by the ratio of particle size to wavelength. Differences in cloud optical properties and thus ΔTB tend to diminish as χ increases.

Problems associated with large particle anisotropy were also described in Chapter 3. The scattering phase function was shown to be very asymmetric, having a strong forward peak and a scattering pattern which becomes more complex as the size parameter increases. The NIR backscatter intensity is significant over a range of particle sizes giving rise to an additional component of reflected radiation from the cloud top which enhances the ΔTB during the day. At night, ΔTB is still positive due primarily to greater transmission of NIR radiation through the cloud from the surface compared to the sum of emitted and transmitted IR radiation.

7.3 Model Simulations of Satellite Viewed Cloud Fields

An overview of topics related to radiometry and image processing was given in Chapter 4. Discrepancies in the spatial and temporal resolution between measurements made from ground-based LIRAD (lidar and infrared radiometer) and satellite-borne instruments were shown to complicate the task of correlating these data. In particular, problems associated with mislocation of cloud tops and degradation of pixel resolution as the satellite nadir angle increases from subpoint were illustrated. The steps required to convert raw analog power received by the VAS and AVHRR scanning radiometers to displayable digital images were also described.

In Chapter 5, the details of the spectral differencing method were discussed for varying solar zenith angles and day vs. night. The potential of the spectral differencing method was summarized in Figure 5.7, which presented a family of curves showing the relationship between ΔTB and τ over the full range of MP-indices defined above. Further radiative arguments were presented to explain why these temperature differences occur and differ for varying microphysics. Differences exist largely due to the differing degree of asymmetry in the scattering phase function for the NIR and IR spectral regions. As forward scattering becomes more pronounced for large particles ($g \rightarrow 1$), the backscattering component in the NIR decreases; thus, ΔTB is reduced as the particle size (or MP-index) increases.

Also, in Chapter 5, the assumption of azimuthal independence was demonstrated to be reasonable for a wide range of emergent angles in the radiation field. In contrast, a much stronger dependence of calculated radiance on quadrature angle was demonstrated.

7.4 Observations and Results (Case Studies)

In Chapter 6, the spectral differencing method was used to analyze bispectral images from NOAA-9 and GOES-6. Lines of pixel elements were analyzed to test the validity of this method. Two case studies were presented. The first involved both ground-based and NOAA-9 satellite observations made of a cirrus deck drifting over a site equipped with a LIRAD system. Radiometric and lidar measurements were analyzed in a time frame of reference and collated with aerological data used to estimate the mean temperature and motion of the cloud layer. After making the appropriate transformation in time and space, satellite and LIRAD measurements were correlated relative to an equivalent brightness temperature-emissivity scale. Further comparison between satellite ΔTB values and theoretical curves of ΔTB vs. r for varying MP-indices provided a means of deducing the MP-index for the cloud. Knowing the radiative properties of the cloud (from the microphysical tables), a time series of observed and theoretically predicted cloud optical depths were produced.

In the second case, a methodology was presented for deducing the MP-index and radiative properties of cirrus utilizing only bispectral measurements from GOES-6 and nearby rawinsonde data. Again, the theoretical relationship between ΔTB and r was exploited through intercomparison of observed and predicted results. The results of this latter case were used to define theoretical values of optical depth as a function of observed ΔTB values for the derived MP-index. An enhancement curve was constructed on the basis of this ΔTB *vs.* r relationship and applied to the differenced satellite image. A "map" of cirrus cloud optical depth was ultimately produced following this procedure.

7.5 Recommendations

The results obtained for the case studies presented in this paper demonstrated the potential usefulness of the spectral differencing method for detecting thin cirrus clouds and,

to a first approximation, determining their monochromatic radiative properties. Of course, many more cases need to be analyzed and validated before the properties so derived can confidently be used to extrapolate the broadband radiative parameters needed to initialize general climate models incorporating the effects of cirrus. Hopefully, the data collected during FIRE will provide the means to carry out this validation process.

The methodology outlined above may be improved by use of more sophisticated models and more accurate initialization of those models based on *in situ* observations. In addition, more precise coordination of data collection with enhanced spatial and temporal resolution and the development of interactive efficient objective analysis techniques are needed.

7.5.1 Model Design and Initialization

In this study, a very simple model was used to simulate the transfer of radiation through idealized hypothetical cirrus clouds. Some loss in accuracy was compromised for efficient use of computer resources. Comparisons between these calculations and those from a more sophisticated radiative transfer models are needed to determine the relative errors which can be attributed to the various simplifying assumptions made in this study. Such a model should be designed for multiple layers enabling calculation of the effects due to IR absorption-emission due to water vapor, CO_2 and O_3 above and below the cloud layer. The component of diffuse surface reflection should be accounted for if surfaces underlying the cloud layer have significant spectral albedos. For thicker clouds, thermal emission must be calculated as a function of the actual temperature profile through the cloud rather than assuming isothermal conditions. Addition of multiple layers will require the implementation of the "adding method" in the radiative transfer model.

Model initialization may be improved by using more realistic cloud models as the microphysical data base broadens and better *in situ* measuements of cirrus characteristics become available. Modified Mie algorithms should be developed and implemented to better determine the optical properties of observed non-spherical ice crystals of varying size distributions. Anisotropy resulting from preferential orientation of these crystals should also be simulated.

7.5.2 Data Collection and Analysis

Development of an objective method to determine cirrus cloud optical properties will require many in depth studies similar to the Aspendale Cirrus Experiment described above. In addition to MSI data, LIRAD and rawinsonde data, *in situ* aircraft measurements of microphysical and radiative cloud properties are needed. All of these data must be closely correlated in time and space to insure reliable results. Intercomparison of these measurements with theoretical model results initialized for specific observed boundary conditions and actual cloud properties are necessary to further verify the accuracy of the method.

The use of the "rapid-scan" mode of the GOES satellites in conjunction with at least two synchronized LIRAD systems is recommended to reduce the errors associated with the discrepancies in the temporal and spatial resolution of these systems. Rapid-scan images would provide higher temporal resolution for satellite measurements, while an array of synchronized LIRAD systems would permit interpolation of the downwelling radiation field providing greater spatial coverage then is possible with only one system. Data obtained in this manner would be much more compatible for comparative analyses. Finally, extensive cirrus systems should be studied throughout their life-cycles in order to understand any diurnal changes which may occur with respect to their physical and/or microphysical and radiative characteristics.

To reiterate, the goal of these studies should be to develop an objective efficient technique to determine cirrus cloud optical properties (day or night) utilizing readily available satellite imagery. With sufficient refinement, it may be possible to provide reliable parameterizations of cirrus radiative effects for use in weather and climate models on an operational basis.

REFERENCES

Ambarzumian, V. A., 1943: Diffuse reflection of light by a foggy medium. *C.R. Acad. Sci. USSR*, **38**, 229-257.

Arking, A. and J. D. Childs, 1985: Retrieval of Cloud Cover Parameters from Multispectral Satellite Images. *J. Climate Appl. Meteor.*, **24**, 322-333.

Barton, I.J., 1983: Upper level cloud climatology from an orbiting satellite. *J. Atmos. Sci.*, **40**, 435-447.

Brumberger, H., et al., 1968: Light Scattering. *Sci. Technol.*, November, 34-60.

Chandrasekhar, S., 1960: *Radiative Transfer.* Dover, 393 pp.

Chesters, D., and W. D. Robinson, 1983: Performance appraisal of VAS radiometry for GOES-4, -5 and -6. *NASA Technical Memorandum*, 85125.

Clark, J. D., 1983: *GOES User's Guide*, U.S. Department of Commerce.

Coakley, J.A., Jr., and F.P. Bretherton, 1982: Cloud cover from high- resolution scanner data: detecting and allowing for partially filled fields of view. *J. Geophys. Res.*, **87**, 4917-4932.

Cox, S.K., S.A. Ackerman and T.H. Vonder Haar, 1986: *Neighbor-to- neighbor objective satellite analysis for the determination of surface and cloud mean radiative properties.* Second Conference on Satellite Meteorology/Remote Sensing and Applications.

Desbois, M., G. Seze and G. Szejwach, 1982: Automatic classification of clouds on METEOSAT imagery: Application to high-level clouds. *J. Appl. Meteor.*, **21**, 401-412.

FIRE (First International Satellite Cloud Climatology Project Regional Experiment), 1983: Research Plan, International Satellite Cloud Climatology Project.

Goody, R.M., 1964: *Atmospheric Radiation: I. Theoretical Basis*, Oxford University Press, 436 pp.

Grant, I.P., and G. Hunt, 1969: Discrete space theory of radiative transfer I. Fundamentals. *Proc. Roy. Soc. London*, **A313**, 183-197.

Hansen, J.E., 1971: Multiple Scattering of Polarized Light in Planetary Atmospheres. Part II. Sunlight Reflected by Terrestrial Water Clouds. *J. ATmos. Sci.*, **28**, 1400-1426.

Heymsfield, A.J., 1975: Cirrus unicus generating cells and the evolution of cirroform clouds. Part I. Aircraft observations of the growth of the ice phase. *J. Atmos. Sci.*, 32, 799-808.

——, and C.M.R. Platt, 1984: A parmaterization of the particle size spectrum of ice clouds in terms of the ambient temperature and the ice water content. *J. Atmos. Sci.*, **41**, 846-855.

——, 1977: Precipitation Development in Stratiform Ice Clouds: A Microphysical and Dynamical Study. *J. Atmos. Sci.*, **34**, 367-381.

Iqbal, M., 1983: ***Introduction to Solar Radiation***, Academic Press, Canada.

King, M.D., 1983: Number of terms required in the Fourier expansion of the reflection function for optically thick atmospheres. *J. Quant. Spectrosc. Radiat. Transfer*, **30** 2, 143-161.

Liou, Kuo-Nan, 1973: Transfer of solar irradiance through cirrus cloud layers. *J. Geophys. Res.*, **78**, 1409-1418.

——, 1974: On the radiative properties of cirrus in the window region and their influence on remote sensing of the atmosphere. *J. Atmos. Sci.*, **31**, 522-532.

——, 1976: On the absorption, reflection and transmission of solar radiation in cloudy atmospheres. *J. Atmos. Sci.*, **33**, 789-805.

——, 1977: Remote sensing of the thickness and composition of cirrus clouds from satellites. *J. Appl. Meteor.*, **16**, 91-99.

——. 1980: ***Introduction of Atmospheric Radiation***, Academic Press, 404 pp.

——, and K.L. Gebhart, 1982: Numerical experiments on the thermal equilibrium temperature in cirrus cloudy atmospheres. *J. Meteor. Soc. Japan*, 570-582.

——, 1986: Influence of cirrus clouds on weather and climate processes: a global perspective. *Mon. Wea. Rev.*, **114**, 1167-1199.

Manabe, S., and R.T. Wetherald, 1967: Thermal equilibrium of the atmosphere with a given distribution of relative humidity. *J. Atmos. Sci.*, **24**, 241-259.

McClatchey, R.A., R.W. Fenn, J.E. Selby, F.E. Volz and J.S. Garing, 1972: Optical properties of the atmosphere, 3rd ed. *AFCRF-72-0497*, 102 pp.

Magono, C., and C.V. Lee, 1966: Meteorological classification of natural snow crystals. *J. Fac. Sci.*, Hokkaido University, Ser. VII, 2, No. 4, 321- 362.

Paltridge, G.W. and C.M.R. Platt, 1976: ***Radiative Process in Meteorology and Climatology***, Elsevier, 318 pp.

——, and C.M.R. Platt, 1981: Aircraft measurements of solar and infrared radiation and the microphysics of cirrus cloud. *Quart. J. Roy. Meteor. Soc.*, **107**, 367-380.

Platt, C.M.R., 1978: Lidar backscatter from horizontal ice cyrstal plates. *J. Appl. Meteor.*, **17**, 482-488.

——, 1979: Remote sounding of high clouds: I. Calculation of Visible and Infrared Optical Properties from Lidar and Radiometer Measurements, *J. Appl. Meteorol.*, **18**, 1130-1143.

——, 1983: On the bispectral method for cloud parameter determination from satellite VISSR data: Separating Broken Cloud and semitransparent cloud. *J. Cli. & Appl. Meteor.*, **22**, 429-439.

——, and A.C. Dilley, 1979: Remote sounding of high clouds. II: Infrared emissivity of cirrostratus. *J. Appl. Meteor.*, **18**, 1144-1150.

——, and A. C. Dilley, 1981: Remote Sounding of high clouds. IV: Observed temperature variations in cirrus optical properties. *J. Atmos. Sci.*, **38**, 1069-1082.

Reynolds, D.W., and T.H. Vonder Haar, 1977: A bispectral method for cloud parameter determination. *Mon. Wea. Rev.*, **105** 447-457.

Satellite and Their Data: Part I, 1982: Workshop on Satellite Meteorology, CIRA, Fort Collins, CO.

Stamnes, K., 1986: Theory of multiple scattering of radiation in plane parallel atmospheres. *Rev. Geophys.*, **24**, 2, 299-310.

Stephens, G.L., 1980a: Radiative properties of cirrus clouds in the infrared region. *J. Atmos. Sci.*, **37**, 2095-2104.

——, 1980b: Radiative transfer on a linear lattice: Application to anisotropic ice crystal clouds. *J. Atmos. Sci.*, **37**, 2095-2104.

——, 1981: *Transfer of 3.7μm radiation through model cirrus clouds*, American Meteorological Society, Boston, Massachusetts.

——, 1984: The parameterization of radiation for numerical prediction and climate models. *Mon. Wea. Rev.*, **112**, 826-867.

——, 1987: Radiative transfer through randomly fluctuating optical metia: I General solution. Submitted to *J. Atmos. Sci.*.

——, and P.J. Webster, 1979: Sensitivity of radiative forcing to variable cloud and moisture. *J. Atmos. Sci.*, **36**, 1542-1556.

——, and P.J. Webster, 1981: Clouds and climate: Sensitivity of simple systems. *J. Atmos. Sci.*, **38**, 235-247.

Tsay, Si-Chee, 1986: Numerical study of atmospheric radiative transfer process with application to the arctic energy balance. Ph.D. Thesis, Dept. of Physics, College of Natural Sciences, Univ. of Alaska, Fairbanks, Alaska.

van de Hulst, H.C., 1957: *Light Scattering by Small Particles*. Wiley, 470 pp.

——, 1980: *Multiple Light Scattering. Tables, Formulas, and Applications*, Vols. 1 and 2. Academic Press.

Vonder Haar, T.H. and D.W. Hillger, 1984: WMO Compendium of Lecture Notes on Meteorological Satellites (for training Class I meteorological personnel), Prepared for the Education and Training Directorate, World Meteorological Organization, Geneva.

Weiss, C., 1978: Cloud-location corrections near the horizon of an SMS image *NOAA, NWS/NESS Satellite Applications Information Note*, 78/8, 8pp.

Wiscombe, W., 1976: On initialization, error and flux conservation in the doubling method. *J. Quant. Spectrosc. Radiat. Transfer*, **16**, 637- 658.

——, 1976: Extension of the doubling method to inhomogeneous sources. *J. Quant. Spectrosc. Radiat. Transfer*, **16**, 477-489.

——, 1977: The delta-M method: Rapid yet accurate radiative flux calculations for strongly asymmetric phase functions. *J. Atmos. Sci.*, **34**, 1408-1422.